Anderson localization in metamaterials and other complex media (Review Article)

Sergey A. Gredeskul[a)]

Ben Gurion University of the Negev, 84105 Beer-Sheva, Israel

Yuri S. Kivshar

Nonlinear Physics Centre, Research School of Physics and Engineering, The Australian National University, Canberra, ACT 0200, Australia

Ara A. Asatryan

Department of Mathematical Sciences, University of Technology, Sydney, NSW 2007, Australia

Konstantin Y. Bliokh

Advanced Science Institute, RIKEN, Wako-shi, Saitama 351-0198, Japan and A. Usikov Institute of Radiophysics and Electronics, 12 Ak. Proskury St., Kharkov 61085, Ukraine

Yuri P. Bliokh

Department of Physics, Technion—Israel Institute of Technology, 32100 Haifa, Israel

Valentin D. Freilikher

Department of Physics, Bar-Ilan University, Raman-Gan 52900, Israel

Ilya V. Shadrivov

Nonlinear Physics Centre, Research School of Physics and Engineering, The Australian National University, Canberra, ACT 0200, Australia

(Submitted March 14, 2012)
Fiz. Nizk. Temp. **38**, 728–765 (July 2012)

This is a review of some recent (mostly ours) results on Anderson localization of light and electron waves in complex disordered systems, including: (i) left-handed metamaterials, (ii) magnetoactive optical structures, (iii) graphene superlattices, and (iv) nonlinear dielectric media. First, we demonstrate that left-handed metamaterials can significantly suppress localization of light and lead to an anomalously enhanced transmission. This suppression is essential at the long-wavelength limit in the case of normal incidence, at specific angles of oblique incidence (Brewster anomaly), and in vicinity of zero-ε or zero-μ frequencies for dispersive metamaterials. Remarkably, in disordered samples comprised of alternating normal and left-handed metamaterials, the reciprocal Lyapunov exponent and reciprocal transmittance increment can differ from each other. Second, we study magnetoactive multilayered structures, which exhibit nonreciprocal localization of light depending on the direction of propagation and on polarization. At resonant frequencies or realizations such nonreciprocity results in effectively unidirectional transport of light. Third, we discuss the analogy between wave propagation through multilayered samples with metamaterials and charge transport in graphene, which provides a simple physical explanation of unusual conductive properties of disordered graphene superlatices. We predict disorder-induced resonance of the transmission coefficient at oblique incidence of Dirac quasiparticles. Finally, we demonstrate that an interplay of nonlinearity and disorder in dielectric media can lead to bistability of individual localized states excited inside the medium at resonant frequencies. This results in nonreciprocity of wave transmission and unidirectional transport of light.
[http://dx.doi.org/10.1063/1.4736617]

1. Introduction

Anderson localization is one of the most fundamental phenomena in physics of disordered systems. Predicted in the seminal paper[1] for spin excitations, it then extended to electrons and other one-particle excitations in solids[2,3] and classical waves,[4–7] and became a paradigm of modern physics.[8] The study of this phenomenon has remained a hot topic for more than 50 years. It is constantly stimulated by new experimental results, including the most recent observations in microwaves,[9–11] optics,[12–14] and Bose–Einstein condensates.[15]

Being a universal wave phenomenon, Anderson localization has natural implications in novel exotic wave systems, such as photonic crystals, meta- and magnetooptical materials, and graphene superlattices. Indeed, left-handed

metamaterials, nonlinear and magnetooptical materials, and graphene[16–22] are involved in the design and engineering of various multilayered structures operating in a broad spectral range, from optical to microwave frequencies. Random wave scattering and localization naturally appear in such systems due to either technological imperfections or intentionally designed random lattices. Importantly, exotic properties of constituent materials essentially require consideration of the interplay of Anderson localization with various additional effects: absorption and gain,[9,23–26] polarization and spin,[27–30] nonlinearity,[13,14,31–33] and magnetooptical phenomena.[34–36] In this review we describe novel remarkable features of Anderson localization of waves in multilayered structures composed of nonconventional materials with unique intrinsic properties.

We start our review in Sec. 2, where the basic concepts and general formalism describing wave propagation, scattering, and localization in random-layered media are introduced. Anderson localization originates from interference of multiply scattered waves, manifesting itself most profoundly in one-dimensional (1D) systems, where all states become localized.[37,38] Due to one-dimensional geometry such systems are well analyzed,[2,39,40] including the mathematical level of rigorousness of the results.[41,42] We describe the exact transfer matrix approach to wave propagation and scattering in layered media. The main spatial scale of localization, i.e., *localization length*, can be defined in two ways: (i) via the Lyapunov exponent of a random system and (ii) via the decrement of wave transmission dependent on the system. In the usual Anderson-localization problems these two localization lengths coincide with each other.

In Sec. 3 we consider transmission and localization properties of multilayered H-stacks comprised of normal materials with right-handed R-layers and mixed M-stacks, also including left-handed L-layers with a negative refractive index.[16] The opposite signs of the phase and group velocities in metamaterials lead to partial or complete cancellation of phase accumulation in multilayered M-stacks. We show that this cancellation suppresses interference of multiple scattering waves and the localization itself.[43–46] Using the weak scattering approximation (WSA)[43,44] we give a detailed analytical and numerical description of transmission and localization properties of both M- and H-stacks and reveal a number of intriguing results. Namely: (i) in the long-wave limit the localization lengths defined via the Lyapunov exponent and transmission decrement differ from each other in M-stacks, (ii) there are two ballistic regimes in the H-stacks, (iii) essential suppression of localization is observed at special angles in the case of oblique incidence (Brewster anomaly) and in vicinity of special frequencies (zero-ε or zero-μ frequencies). Finally, in Sec. 3.7 we discuss anomalous enhancement[43] of wave transmission in minimally disordered alternated M-stacks of metamaterials, where layer thicknesses are equal, and only dielectric permittivities (or only magnetic permeabilities) vary.

Section 4 is devoted to the study of novel localization features in novel materials. We begin with a discussion of localization of light propagating through magnetoactive multilayered structures, with either Faraday or Cotton–Mouton (Voigt) geometries (Sec. 4.1). We show that magnetooptical effects can significantly affect phase relations, resulting in nonreciprocal localization depending on the direction of wave propagation and polarization of light. At resonant frequencies corresponding to the excitation of localized states inside the sample, a nonreciprocal shift of resonance results in effectively unidirectional transmission of light.[34] In Sec. 4.2 conducting properties of a graphene layer subject to stratified electric field are considered. The close analogy between charge transport in such system and wave transmission through a multilayered stack[47] underpins remarkable conductive properties of disordered graphene.[48] We predict disorder-induced resonance of the transmission coefficient at oblique incidence of electron waves. Finally, in Sec. 4.3, we examine the interplay between nonlinearity and disorder in resonant transmission through a random-layered dielectric medium.[31] Owing to effective energy localization and pumping, even weak Kerr nonlinearity can play a crucial role leading to bistability of Anderson localized states inside the medium. Akin to magnetooptical structures, this brings about unidirectional transmission of light.

2. Random multilayered structures

2.1. Transmission length and the Lyapunov exponent

As mentioned above, 1D Anderson localization results is exponential decay of the transmission coefficient with length L of the sample. For multilayered systems, it is important to use the total number of layers N and mean layer thickness L/N. In what follows we use dimensionless variables measuring all lengths in mean layer thickness units, while time dependence is shown in the form $e^{-i\omega t}$. For simplicity, throughout this review we mainly consider the lossless stacks. Detailed results concerning the case of stacks with losses can be found in the original works.

Let us introduce the dimensionless transmission length l_N on realization that

$$\frac{1}{l_N} = \frac{\ln|T_N|}{N} = -\frac{\mathrm{Re}\ln T_N}{N}$$

and the "averaged" N-dependent dimensionless transmission length $l_T \equiv l_T(N)$ of a multilayered N-layered stack,

$$\frac{1}{l_T} = -\left\langle \frac{\ln|T_N|}{N} \right\rangle = -\left\langle \frac{\mathrm{Re}\ln T_N}{N} \right\rangle. \qquad (2.1)$$

Here, T_N is the stack amplitude transmission coefficient related to its transmittivity $\mathcal{T}_N$ by the equality $\mathcal{T}_N = |T_N|^2$. Due to self-averaging of $\ln|T_N|/N$ both the lengths l_T and l_N tend to the same limit

$$\lim_{N\to\infty} l_T = \lim_{N\to\infty} l_N = l, \qquad (2.2)$$

as the number N of layers tends to infinity. Following[49] we recall l as the localization length. This localization length is related directly to the transmission properties. Its reciprocal value is nothing but the decrement of the stack transmission coefficient.

The transmission coefficient in these equations is naturally expressed in terms of the total T-matrix of the stack written on the basis of a running wave. Consider transmission of a plane wave, which is normal on the left to the stack comprised of an even number N of layers and embedded into free space. In the simplest case, the wave is described in terms of two component vectors of, say, an electric field e. Within a uniform medium with dielectric permittivity ε and magnetic permeability μ, the field e has the form

$$e(z) = e^{+}\mathrm{e}^{ikz} + e^{-}\mathrm{e}^{-ikz}, \quad k = \frac{\omega}{c}\sqrt{\varepsilon\mu}, \tag{2.3}$$

with z axis directed to the right (here and below all the lengths in the problem are dimensionless and measured in the mean layer thickness).

If the components of vector $\mathbf{e}$ are normalized in such a way that the energy flux of the wave Eq. (2.3) is $|e^{+}|^2 - |e^{-}|^2$, then the amplitudes,

$$\mathbf{e}_{L,R} = \begin{pmatrix} e^{+}_{L,R} \\ e^{-}_{L,R} \end{pmatrix} \tag{2.4}$$

of the field from both sides out of the N-layer stack are related by its transfer matrix $\hat{T}(N)$,

$$\mathbf{e}|_L = \hat{T}(N)\mathbf{e}|_R, \tag{2.5}$$

which is expressed via transmission and reflection coefficients of the stack as

$$\hat{T}(N) = \begin{Vmatrix} \dfrac{1}{T_N} & \dfrac{R_N^*}{T_N^*} \\ \dfrac{R_N}{T_N} & \dfrac{1}{T_N^*} \end{Vmatrix}, \tag{2.6}$$

where the asterisk denotes complex conjugation.

Methods of calculating the transmission coefficient

$$T(N) = (\hat{T}_{11})^{-1} \tag{2.7}$$

are discussed in the next subsection.

In what follows we consider stacks composed of weak scattering layers with reflection coefficients of each layer much smaller than 1. In spite of this, for a sufficiently long stack the transmission coefficient is exponentially small $|T_N| \sim \exp(-\kappa N)$ with decrement coinciding with reciprocal localization length $\kappa = l_T^{-1}$ (localized regime). However, a short stack comprising a comparatively small number of layers is almost transparent $|R_N|^2 \ll 1$ (ballistic regime). Here, the transmission length takes the form

$$l_N \approx b = \frac{\langle |R_N|^2 \rangle}{2N}, \tag{2.8}$$

involving average reflectance.[50] This follows directly from Eq. (2.1) by virtue of the current conservation relationship, $|R_N|^2 + |T_N|^2 = 1$. The length b in this equation is termed the ballistic length.

Accordingly, in studies of the transport of classical waves in one-dimensional random systems, the following spatial scales arise in a natural way:

- l_T — *transmission length* of a finite sample Eq. (2.1),
- l — *localization length* Eq. (2.2) related to transmission properties, and
- b — *ballistic length* Eq. (2.8).

Exponential decrease of the transmission coefficient with the stack size is only a manifestation of Anderson localization. The phenomenon of localization itself is the localized character of eigenstates in an infinite disordered system with sufficiently fast decaying correlations. The quantitative characteristic of such a localization is the Lyapunov exponent, which is the increment of exponential growth of the currentless state with a given value at a certain point far from this point. The amplitude Eq. (2.4) of the currentless state in inhomogeneous medium in the basis of running waves can be parameterized as,

$$\mathbf{e} = \mathrm{e}^{\xi}\begin{pmatrix} \mathrm{e}^{i\theta} \\ \mathrm{e}^{-i\theta} \end{pmatrix} = R\begin{pmatrix} \mathrm{e}^{i\theta} \\ \mathrm{e}^{-i\theta} \end{pmatrix}, \tag{2.9}$$

where $R(z)$ and $\theta(z)$ are the modulus and the phase of the considered currentless solution, respectively.

It is known[2,41] that at given initial values $\xi(0)$, $(R(0))$, and $\theta(0)$ the function $\xi(z)$ at a sufficiently far point is approximately proportional to its distance from the initial point. In discrete terms, with probability of 1 the positive limit exists

$$\gamma = \lim_{N\to\infty}\frac{\xi(N)}{N} = \lim_{N\to\infty}\frac{1}{N}\ln\frac{R(N)}{R(0)}, \tag{2.10}$$

which is called the Lyapunov exponent. Its reciprocal value is also called *localization length*

$$l_\xi = \frac{1}{\gamma}. \tag{2.11}$$

However, the index ξ reminds us that this localization length is defined through the Lyapunov exponent.

To compare the two localization lengths l and l_ξ we first consider the continuous case where the corresponding dynamic variable $\xi(z)$ depends on the continuous coordinate z. In this case, transmittance of the system with length L is exactly expressed as,[2,42]

$$\mathcal{T}_L \equiv |T_L|^2 = \frac{4}{\mathrm{e}^{2\xi_c(L)} + \mathrm{e}^{2\xi_S(L)} + 2}, \tag{2.12}$$

where $\xi_c(z)$ and $\xi_s(z)$ are two independent solutions satisfying the so-called cosine and sine initial conditions $\theta_c(0) = 0$ and $\theta(0) = \pi/2$ and having the same limiting behavior

$$\gamma = \frac{1}{l_\xi} = \lim_{z\to\infty}\frac{\xi_c(z)}{z} = \lim_{z\to\infty}\frac{\xi_S(z)}{z}. \tag{2.13}$$

Equations (2.12) and (2.13) evidently show that in the continuous case l and l_ξ coincide exactly.

In the discrete case (multilayered stack) the corresponding expression for transmittance reads

$$\mathcal{T}_N \equiv |T_N|^2 = 4[e^{2\xi_c(N)} + e^{2\xi_S(N)} + 2e^{\xi_c(N)+\xi_S(N)}\sin(\theta_c(N) - \theta_S(N))]^{-1}. \quad (2.14)$$

Here, the last term in the denominator differs from that in Eq. (2.12). Moreover, it can change its sign and, generally speaking, can essentially reduce the denominator itself thus enlarging transmittance, and as a result enlarging the localization length l_ξ compared to l. Thus, Eqs. (2.10) and (2.14) enable us to state only that $l \geq l_\xi$ in contrast to the continuous case, where these two localization lengths always coincide. In spite of that, the study of localization in normal disordered multilayered stacks did not show any difference in the two lengths. We will see below that such a difference manifests itself truly in the alternating metamaterial stacks.

In this review we are mainly interested in the transmission length l_T. This quantity can be found directly by standard transmission experiments. At the same time, it is sensitive to the size of the system and, therefore, is best suited to the description of transmission properties in both the localized and the ballistic regimes. More precisely, transmission length coincides either with the localization length l or with the ballistic length b in the case of comparatively long stacks (localized regime) or comparatively short stacks (ballistic regime), respectively. That is,

$$l_T \approx \begin{cases} l, & N \gg l, \\ b, & N \ll b. \end{cases}$$

2.2. Transfer matrices and weak scattering approximation

In this subsection we describe some methods used for the calculation of transmission length and other transmission or/and localization characteristics in various regimes. All of them are based on various versions of transfer matrix approach.

Consider the M-stack comprised of an even number N of alternating uniform layers labeled by index $j = 1,\ldots, N$ from right to left, so that all odd layers $j = 2n-1$, are of type "α" and all even layers $j = 2n$ are of type "β," $n = 1,2,\ldots, N/2$ (see Fig. 1). In general the jth layer is characterized by its dimensionless thickness d_j, dielectric permittivity ε_j, and magnetic permeability μ_j.

The total transfer matrix Eq. (2.6) is factorized to the product

$$\hat{T}(N) = \hat{t}_N \hat{t}_{N-1} \ldots \hat{t}_2 \hat{t}_1 \quad (2.15)$$

of the layer transfer matrices $\hat{t}_j$.

Note that for the alternating stack under consideration it is natural to join each pair of subsequent layers with numbers $j = 2n-1$ and $j = 2n$ into one effective cell number n. Then the total transfer matrix factorizes to the product of $N/2$ transfer matrices of separate cells.[43,51–54]

Parametrizing the transfer matrix of the jth layer by its transmission t_j and reflection r_j coefficients of a corresponding layer we obtain the recurrence relations

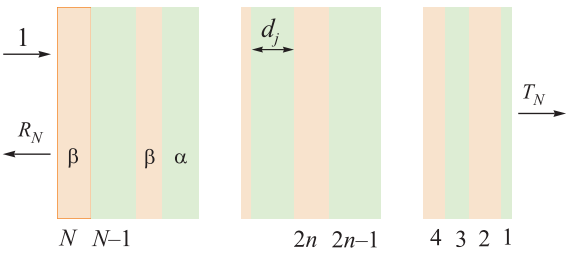

FIG. 1. (Ref. 43) Two-component multilayered alternative stack.

$$T_j = \frac{T_{j-1}t_j}{1 - R_{j-1}r_j}, \quad T_0 = 1, \quad (2.16)$$

$$R_j = r_j + \frac{R_{j-1}t_j^2}{1 - R_{j-1}r_j}, \quad R_0 = 0, \quad (2.17)$$

where T_j and R_j are transmission and reflection coefficients of the reduced stack comprised only of j first layers. These relations provide an *exact* description of the system and will be used later for direct numerical simulations of its transmission properties. Another possible, but less effective way is related to direct numerical calculation of the total transfer matrix Eq. (2.15).

Relations (2.16) and (2.17) serve as a starting point for the weak scattering approximation (WSA) elaborated on in Ref. 43 and based on the assumption that reflection from a single layer is small, i.e., $|r_j| \ll 1$. This demand is definitely satisfied in the case of weak disorder. Within WSA, instead of exact relations (2.16) and (2.17) we use for the transmission length the following first order approximations,

$$\ln T_j = \ln T_{1,j-1} + \ln t_j + R_{j-1}r_j, \quad (2.18)$$

$$R_j = r_j + R_{j-1}t_j^2, \quad j = 2,3,\ldots,N. \quad (2.19)$$

Note that in deriving Eq. (2.19) we omit the first-order term $R_{j-1}^2 t_j^2 r_j$. This is an uncontrolled action. The omitted term contributes only to the second order of $\ln T_j$ after the first iteration for a not very large number of layers j. For sufficiently large j the term should be taken into account. Nevertheless, as will be shown below, this approximation works very well in the entire wavelength region.

Neglecting the last term on the right-hand side of Eq. (2.18) results in the so-called single-scattering approximation (SSA), which implies that multi-pass reflections are neglected, so that the total transmission coefficient is approximated by the product of the single layer transmission coefficients, just as the total transmittance is approximated by the product of single layer transmittances, which results in

$$\ln|T_N| = \sum_{j=1}^{N} \ln|t_j|.$$

In the case of very long stacks (i.e., as the length $N \to \infty$) we can replace the arithmetic mean, $N^{-1}\sum_{j=1}^{N} \ln|t_j|$, by its

ensemble average $\langle \ln |t| \rangle$. On the other hand, in this limit the reciprocal of the transmission length coincides with the localization length. Using the energy conservation law, $|r_j|^2 + |t_j|^2 = 1$, which applies in the absence of absorption, the reciprocal localization length in single-scattering approximation may be written as,

$$\left(\frac{1}{l}\right)_{SSA} = \frac{1}{2}\langle |r|^2 \rangle$$

and is proportional to the mean reflectance of a single random layer.[2,55]

The version of transfer matrix approach described above is based on the consideration of a single layer embedded into vacuum. This version and related WSA were used in Refs. 43–46 for analytical and numerical study of metamaterial M-stacks (see Sec. 3).

Another version used in Ref. 34 (Sec. 4.1) is based on separation of wave propagation inside a layer and through the interface between layers (see, e.g., Ref. 56). Here, wave propagation inside the jth layer is described by a diagonal transfer matrix

$$\hat{S}_j = \mathrm{diag}\left(\mathrm{e}^{-i\varphi_j}, \mathrm{e}^{-i\varphi_j}\right), \tag{2.20}$$

where $\varphi_j = k_j d_j$ is the phase accumulated upon the wave propagating from left to right through the jth layer, and $k_j = (\omega/c)\sqrt{\varepsilon_j \mu_j}$. The interfaces are described by unimodular transfer matrices $\hat{F}^{0\alpha}, \hat{F}^{\alpha\beta}, \hat{F}^{\beta\alpha}, \hat{F}^{\beta 0}$ corresponding, respectively, to transitions (all from left to right) from vacuum to the medium "α," from the medium "α" to the medium "β," from the medium "β" to the medium "α," and from the medium "α" into vacuum. Thus, the total transfer matrix Eq. (2.6) of the structure in Fig. 1 is

$$\hat{T}(N) = \hat{F}^{0\alpha}\hat{F}_N\hat{S}_N\hat{F}_{N-1}\hat{S}_{N-1}\ldots\hat{F}_2\hat{S}_2\hat{F}_1\hat{S}_1\hat{F}^{\alpha 0},$$
$$\hat{F}_{2n-1} \equiv \hat{F}^{\beta\alpha}, \quad \hat{F}_{2n} \equiv \hat{F}^{\alpha\beta}, \quad n = 1, 2, \ldots, N/2. \tag{2.21}$$

Using the group property of the interface transfer matrices: $\hat{F}^{\beta\alpha} = \hat{F}^{\beta 0}\hat{F}^{0\alpha}$ and $\hat{F}^{\alpha\beta} = \hat{F}^{\alpha 0}\hat{F}^{0\beta}$ the total transfer matrix is factorized to the product Eq. (2.15), where the layer transfer matrices are

$$\hat{t}_{2n} = \hat{F}^{0\beta}\hat{S}_{2n}\hat{F}^{\beta 0}, \quad \hat{t}_{2n-1} = \hat{F}^{0\alpha}\hat{S}_{2n-1}\hat{F}^{\alpha 0}.$$

Such a representation is especially efficient in the short-wave limit, where the total transmission coefficient is reduced to the product of transmission coefficients of interfaces only (see Ref. 56 and Sec. 4.1).

We now come to the application of the transfer matrix approach to the calculation of the Lyapunov exponent γ. For each layer we define the currentless vector $\mathbf{e}_j$ by Eq. (2.9) with the corresponding values ξ_j and θ_j. In these terms the Lyapunov exponent is written as

$$\gamma = \lim_{j\to\infty}\frac{\xi_j}{j} = \lim_{j\to\infty}\left(\xi_j - \xi_{j-1}\right) \tag{2.22}$$

(using the Stolz theorem). The vectors $\mathbf{e}_j$ and $\mathbf{e}_{j-1}$ satisfy the equation,

$$\mathbf{e}_j = \hat{t}_{j-1}\mathbf{e}_{j-1}. \tag{2.23}$$

Therefore, the difference in the r.h.s. of Eq. (2.22) is some function of θ_{j-1} is

$$\xi_j - \xi_{j-1} = \Phi\left(\theta_{j-1}\right), \tag{2.24}$$

the explicit form of which is determined by Eq. (2.23). Using self averaging of the ratio ξ_j/j and the fact that the phase θ_j stabilizes,[2] we finally obtain the Lyapunov exponent,

$$\gamma = \langle \Phi(\theta) \rangle_{\mathrm{st}}, \tag{2.25}$$

where the average in the r.h.s. is taken over the stationary distribution of the phase θ.

A continuous version of this result was obtained in Ref. 2 (see Eq. (10.2)). Its discrete version in slightly different terms (see Sec. 3.7) was obtained in Ref. 57. Note that due to the existence of the closed formula (2.25) for the Lyapunov exponent the task of analytical calculation of the localization length $l_\xi = \gamma^{-1}$ is a simpler problem than that of the transmission length l_T.

The following steps are standard (see, e.g., Refs. 2 and 58): using Eq. (2.23) to get the dynamic equation for the phase θ, write down the corresponding Fokker–Planck equation for its distribution, solve it, and calculate the average Eq. (2.25). Moreover, in weakly disordered systems only the first and the second order terms should be accounted for in the dynamic equations.[2,59] For minimally disordered M-stacks defined in Sec. 1 this program was successfully realized in Refs. 51 and 52 (see Sec. 3.7 below).

3. Suppression of localization in metamaterials

Over the past decade the physical properties of metamaterials and their possible applications in modern optics and microelectronics have received considerable attention (e.g., see Refs. 7, 18, 60, and 61). The reasons for such interest are the unique physical properties of metamaterials, including their ability to overcome the diffraction limit,[16,17] potential role in cloaking,[62] suppression of spontaneous emission rate,[63] enhancement of quantum interference,[64] etc. One of the first studies of the effect of randomness[65] revealed that weak microscopic disorder may lead to a substantial suppression of wave propagation through magnetic metamaterials over a wide range of frequencies. Therefore, the next problem was to study localization properties of disordered metamaterial systems.

It is known that in normal multilayered systems comprising right-handed media the localization length is proportional to the square of the wavelength λ in the long-wavelength limit, that it tends to a constant in a short-wavelength regime, and oscillates irregularly in the intermediate region.[4,6,49,66,67] Naturally, the question arises: how inclusion of metamaterial layers influences the localization and transmission effects.

The study of localization in metamaterials was started in Ref. 68, where wave transmission through an alternating

sequence of air layers and metamaterial layers of random thicknesses was studied. Localized modes within the gap were observed, and delocalized modes were revealed despite one-dimensional nature of the model. Then, a comprehensive study of transmission properties of M-stacks was conducted.[43–46] Here, anomalous enhancement of transmission through minimally disordered (see Sec. 1) M-stacks was revealed,[43] non-coincidence of the two localization lengths l and l_ξ was established,[44] polarization[45] and dispersion[46] effects in transmission were studied.

Scaling laws of transmission through a similar mixed multilayered structure were investigated in Ref. 69. It was shown that spectrally averaged transmission in a frequency range around the fully transparent resonant mode decayed with the number of layers much more rapidly than in a random homogeneous slab. Localization in a disordered multilayered structure comprised of alternating random layers of two different left-handed materials was considered in Ref. 70. Within the propagation gap, the localization length was shorter than the decay length in the underlying periodic structure (opposite of that observed in the random structure of right-handed layers).

A detailed investigation of the Lyapunov exponent (and, therefore, localization length l_ξ) in various multilayered metamaterials is presented in Refs. 51–54. In the weak disorder limit, explicit expressions for the Lyapunov exponent valid in the entire region of wavelengths for various kinds of correlated disorders were obtained,[53,54] and an analytical explanation of anomalous suppression of localization was found.[51,52]

Dispersion effects in M-stacks comprised by metamaterial layers separated by air layers with only positional disorder were considered in Refs. 71–73. Here, essential suppression of localization in vicinity of the Brewster angle and at the very edge of the band gap was revealed,[71] influence of both quasi-periodicity and structural disorder was studied,[72] and effects of some types of disorder correlation on light propagation and Anderson localization were investigated.[73]

In this section we consider suppression of localization in sufficiently disordered M-stacks. In the first four subsections we consider the model with noncorrelated fluctuating thicknesses and dielectric permittivities. This model possesses the main features caused by the presence of metamaterials and at the same time remains comparatively simple. The results concerning disorder correlations can be found in papers mentioned in the previous paragraph and a recent detailed survey.[40] The presentation is mostly based on works.[43–46,52]

3.1. Model

We start with the model described at the beginning of Sec. 2.2 and displayed in Fig. 1. Electromagnetic properties of the jth layer with given dielectric permittivity ε_j and magnetic permeability μ_j are characterized by its impedance Z_j and refractive index ν_j,

$$Z_j = \sqrt{\mu_j/\varepsilon_j}, \quad \nu_j = \sqrt{\mu_j \varepsilon_j}. \tag{3.1}$$

Being embedded into vacuum, each layer can be described by its reflection and transmission coefficients with respect to a wave with dimensionless length λ incident from the left

$$r_j = \frac{\rho_j(1-\mathrm{e}^{2i\beta_j})}{1-\rho_j^2\mathrm{e}^{2i\beta_j}}, \quad t_j = \frac{(1-\rho_j^2)\mathrm{e}^{i\beta_j}}{1-\rho_j^2\mathrm{e}^{2i\beta_j}}. \tag{3.2}$$

Here, $\rho_j = (Z_j - 1)/(Z_j + 1)$ is the Fresnel coefficient, $\beta_j = kd_j\nu_j$, and $k = 2\pi/\lambda$ is dimensionless wavenumber.

Within our model, dielectric permittivity, magnetic permeability, and thickness of the jth layer have the form,

$$\varepsilon_j = (-1)^j(1+\delta_j^{(\nu)})^2, \quad \mu_j = (-1)^j, \quad d_j = 1+\delta_j^{(d)}, \tag{3.3}$$

so that the corresponding impedance and refractive index are

$$Z_j = \sqrt{\mu_j/\varepsilon_j} = (1+\delta_j^{(\nu)})^{-1}, \tag{3.4}$$

$$\nu_j = (-1)^j(1+\delta_j^{(\nu)}). \tag{3.5}$$

Thickness fluctuations $\delta_j^{(d)}$ are independent, identically distributed zero-mean random variables, as well as all refractive index fluctuations $\delta_j^{(\nu)}$. To justify the weak scattering approximation we assume that all these quantities $\delta_j^{(d,\nu)}$ are small.

The considered model possesses some symmetry: statistical properties of fluctuations and the absorption coefficient are the same for L and R layers. As a consequence of this symmetry, the scattering coefficients of R and L layers are complex conjugate $t_r = t_l^*$ and $r_r = r_l^*$, resulting in the relations,

$$\langle g(t_r)\rangle = \langle g(t_l)\rangle^*, \quad \langle g(r_r)\rangle = \langle g(r_l)\rangle^* \tag{3.6}$$

valid for any real value function g in either the lossless or the absorbing case. In more general models this symmetry can be broken.

The model with two parameters (here, thickness and refractive index) is in a sense the simplest sufficiently disordered model. Further simplification, where only one of these quantities is random, qualitatively changes the picture. Indeed, the case of an M-stack with only thickness disorder in the absence of absorption is rather trivial: such a stack is completely transparent (a consequence of $Z_j \equiv 1$). On the other hand, an M-stack with only refractive-index disorder, as it was revealed in Ref. 43, manifests dramatic suppression of Anderson localization: essential enlightenment in the long-wave region. This intriguing case is considered below in Sec. 3.7. Here we focus on the case where both types of disorder are present simultaneously.

Specific features of transmission and localization in M-stacks look more pronounced in comparison to those of homogeneous stacks (H-stacks), comprised of solely either right-handed or left-handed layers. Therefore, albeit localization in disordered H-stacks with right-handed layers has been studied by many authors,[6,26,49,66,74] we also consider this problem here in its most general formulation. This consideration enables us to compare localization properties of M- and H-stacks. To describe an H-stack composed of only R (L) layers, all the multipliers $(-1)^j$ in Eqs. (3.3) and (3.5) should be replaced with 1 (–1).

3.2. Mixed stack

Within the version Eqs. (2.18) and (2.19) of weak scattering approximation, contributions from even and odd layers are separated. As a result, transmission length of a finite length M-stack may be cast in the form[44]

$$\frac{1}{l_N} = \frac{1}{l} + \left(\frac{1}{b} - \frac{1}{l}\right) f(N/\bar{l}), \tag{3.7}$$

where

$$f(x) = \frac{1 - \mathrm{e}^{-x}}{x}. \tag{3.8}$$

Localization length l, ballistic length b, and *crossover length* $\bar{l}$ are completely described by the three averages $\langle \ln|t| \rangle$, $\langle r \rangle$, and $\langle t^2 \rangle$, composed of transmission t and reflection r coefficients of a single right-handed layer

$$\frac{1}{l} = -\langle \ln|t| \rangle - \frac{|\langle r \rangle|^2 + \mathrm{Re}(\langle r \rangle^2 \langle t^2 \rangle^*)}{1 - |\langle t^2 \rangle|^2}, \tag{3.9}$$

$$\frac{1}{b} = \frac{1}{l} - \frac{2/\bar{l}}{1 - \exp(-2/\bar{l})} \times \left(\frac{|\langle r \rangle|^2 + \mathrm{Re}(\langle r \rangle^2 \langle t^2 \rangle^*)}{1 - |\langle t^2 \rangle|^2} - \frac{|\langle r \rangle|^2}{2} \right),$$

$$\bar{l} = -\frac{1}{\ln|\langle t^2 \rangle|}. \tag{3.10}$$

Equations (3.7)–(3.10) are valid in the presence of absorption. However, below, to make our treatment more transparent, we consider the lossless case.

The characteristic lengths l, b, and $\bar{l}$ are functions of wavelength λ. The first two always satisfy the inequality $(\lambda) > b(\lambda)$, while in the long-wavelength region the crossover length is the shortest of the three, $b(\lambda) > \bar{l}(\lambda)$. In the case of a fixed wavelength λ, for comparatively short stacks with $N \ll \bar{l}(\lambda)$ the function $f(N, \bar{l}) \approx 1$, while for sufficiently long stacks $N \gg \bar{l}(\lambda)$ it tends to zero $f(N, \bar{l}) \approx 0$. Correspondingly, transmission length coincides with the ballistic length $l_T(\lambda) \approx b(\lambda)$ for short stacks $N \ll \bar{l}(\lambda)$ and with localization length $l_T(\lambda) \approx l(\lambda)$ for long stacks $N \gg \bar{l}(\lambda)$, with the transition between the two ranges of N being determined by the crossover length $\bar{l}(\lambda)$. Thus, ballistic regime occurs when the stack is much shorter than the crossover length $N \ll \bar{l}(\lambda)$. The localized regime is realized for the stacks longer than localization length $N \gg l(\lambda)$. For stacks of intermediate sizes $\bar{l}(\lambda) \lesssim N \lesssim l(\lambda)$ transmission length coincides with the localization length, however, they correspond to the transition region between the ballistic regime and the localized one.

Alternatively we can consider the stack with a given size N and use the wavelength as the parameter governing the localized and ballistic regimes. To do this, we introduce two characteristic wavelengths, $\lambda_1(N)$ and $\lambda_2(N)$, defined by the relations,

$$N = l(\lambda_1(N)), \quad N = \bar{l}(\lambda_2(N)). \tag{3.11}$$

In these terms, the localized regime occurs if $\lambda \ll \lambda_1(N)$, while in the long-wavelength region, $\lambda \gg \lambda_2(N)$, the propagation is ballistic. Intermediate range of wavelengths, $\lambda_1(N) < \lambda < \lambda_2(N)$, corresponds to the transition region between the two regimes.

Consider now the example of rectangular distribution, where the fluctuations $\delta_j^{(\nu)}$ and $\delta_j^{(d)}$ are uniformly distributed over the intervals $[-Q_\nu, Q_\nu]$ and $[-Q_d, Q_d]$, respectively, and have the same order of magnitude $Q_\nu \sim Q_d$, so that the dimensionless parameter

$$\zeta = 2\frac{Q_d^2}{Q_\nu^2}$$

is on the order of unity.

In the next step we calculate the averages $\langle \ln|t| \rangle$, $\langle |r| \rangle$, and $\langle |t^2| \rangle$ with the help of Eqs. (3.2)–(3.5), substitute them into Eqs. (3.9) and (3.10), and neglect the contribution of terms of order higher than Q_d^2. The resulting general expressions for localization, ballistic, and crossover lengths are rather cumbersome, so we present here only their asymptotical forms.

In the short-wavelength region, the main contribution to localization length is related to the first term in the r.h.s. of Eq. (3.9), corresponding to the single scattering approximation, and the localization length is

$$l(\lambda) = \frac{12}{Q_\nu^2}, \quad \lambda \ll 1. \tag{3.12}$$

This means that the size N of the short stack $NQ_\nu^2 \ll 1$ is always smaller than the localization length, and short-wave transmission through a short stack is always ballistic.

The opposite limiting case $NQ_\nu^2 \gg 1$ corresponds to long stacks. In this case both regimes are realized, and transition from localized propagation to the ballistic one occurs at the long wavelength $\lambda \sim Q_\nu\sqrt{N} \gg 1$. Indeed, asymptotical expressions for all three characteristic lengths read

$$l(\lambda) \approx \frac{3\lambda^2}{2\pi^2 Q_\nu^2} \frac{3+\zeta}{1+\zeta}, \tag{3.13}$$

$$\bar{l}(\lambda) \approx \frac{3\lambda^2}{2\pi^2 Q_\nu^2} \frac{1}{4(3+\zeta)}, \tag{3.14}$$

and

$$b(\lambda) \approx \frac{3\lambda^2}{2\pi^2 Q_\nu^2}. \tag{3.15}$$

Note that the single scattering approximation for localization length fails in the long-wave limit because both terms in the r.h.s. of Eq. (3.9) contribute to the asymptotic value Eq. (3.13).

Thus, in the symmetric weak scattering case, ballistic, localization, and crossover lengths in the long-wave region differ only by numerical multipliers, satisfy the inequality $\bar{l}(\lambda) < b(\lambda) < l(\lambda)$ mentioned above, and are proportional to λ^2. Two characteristic wavelengths Eq. (3.11) corresponding to localization length Eq. (3.13) and crossover length Eq. (3.14), are proportional to $Q_\nu\sqrt{N}$, differ only by a numerical multiplier, and satisfy the inequality $\lambda_1(N) < \lambda_2(N)$. For

sufficiently long stacks $NQ_\nu^2 \gg 1$, they are lying in the long-wave region $\lambda_{1,2} \gg 1$.

Localization properties of an infinite stack are described by the Lyapunov exponent Eq. (2.10) or by localization length Eq. (2.11). Within the considered model Eqs. (3.2)–(3.5), its long-wave asymptotic value calculated with the help of the well known transfer matrix approach reads

$$\gamma \approx \frac{\pi^2 \overline{\left(1+\delta^{(d)}\right)^2}}{2\lambda^2} \frac{\overline{\epsilon^2} - \overline{\epsilon}^2}{\overline{\epsilon}}, \quad \epsilon = (1+\delta^{(\nu)})^2. \tag{3.16}$$

In the case of rectangular distribution of fluctuations of the dielectric constants and thicknesses described above, the reciprocal of the Lyapunov exponent is reduced to

$$l_\xi(\lambda) = \gamma^{-1}(\lambda) \approx \frac{3\lambda^2}{2\pi^2 Q_\nu^2} \tag{3.17}$$

coinciding with the ballistic length $b(\lambda)$. Thus, the disordered M-stack in the long-wavelength region presents a unique example of a one-dimensional disordered system, in which the localization length, defined as transmission decrement of a sufficiently long stack, differs from the reciprocal of the Lyapunov exponent.

The qualitative picture of transmission and localization properties of the symmetric mixed stack described above remains correct in the much more general case, where statistical properties of the r and l layers are different, and the distributions of fluctuations and thicknesses are not rectangular. The only distinction we expect is that localization and crossover lengths will have different wavelength dependence, which will result in a more complicated structure of the ballistic region, like that considered below for an H-stack (see Sec. 3.3 below).

To check the WSA theoretical predictions formulated above we provided a series of numerical calculations. They were made for the lossless stack with uniform distributions of fluctuations $\delta(d)$ and $\delta(\nu)$, with widths $Q_\nu = 0.25$ and $Q_d = 0.2$, respectively, and included: (a) direct simulations based on the exact recurrence relations (2.16) and (2.17); (b) weak scattering analysis for the transmission length. In all cases, unless otherwise mentioned, ensemble averaging is taken over $N_r = 10^4$ realizations.

Throughout this subsection we considered only M-stacks. Nevertheless, to emphasize the main features of the transmission in metamaterials, we compare transmission spectra for an M-stack of $N = 10^5$ layers and an H-stack of length $N = 10^3$, plotted in the same Fig. 2. Both stacks are sufficiently long: for the shortest of them the parameter NQ_ν^2 is 62.5 $\gg$1. There are two major differences between the results for these two types of samples: first, in the localized regime ($N \gg l_T$) transmission length of the M-stack exceeds or coincides with that of the H-stack; second, in the long-wavelength region the plot of transmission length of the M-stack exhibits a pronounced bend or kink in the interval $\lambda \in [10^2, 10^3]$, while there is no such feature in the results for the H-stack.

Figure 2 demonstrates excellent agreement of analytical and numerical results: the curves obtained by direct numerical simulations and by calculations based on the weak scattering approximation are indistinguishable (solid line). The short- and long-wavelength behavior of the transmission length is also in excellent agreement with the calculated asymptotics in both regimes. The characteristic wavelengths of this mixed stack are $\lambda_1 \approx 148$ and $\lambda_2 \approx 839$. Therefore, the region $\lambda \lesssim 148$ corresponds to the localized regime, whereas longer wavelengths, $\lambda \gtrsim 839$, correspond to the ballistic regime. Thus, the kink observed within the region $\lambda_1 \lesssim \lambda \lesssim \lambda_2$ describes the crossover from the localized to the ballistic regime. The long-wave asymptotic value of the ballistic length, as we saw below, coincides with that of the reciprocal of the Lyapunov exponent. Therefore, the difference between the localization and the ballistic lengths of the M-stack simultaneously confirms the difference between the localization length and the reciprocal of the Lyapunov exponent in the localized regime.

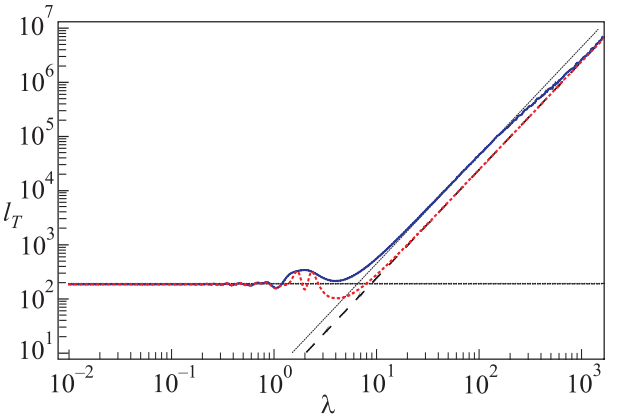

FIG. 2. (Ref. 44) Transmission length l_T vs. λ for an M-stack (thick solid line, direct simulation and calculations based on WSA recurrence relations) and an H-stack (thick dashed line, direct simulation). Asymptotic values of the localization length l: the short-wavelength asymptotic value (thin dotted line), and the long-wavelength asymptotic values (a thin solid line for the M-stack and a thin dashed line for the H-stack).

More detailed numerical calculations of the transmission length, average reflectance, and characteristic wavelengths of M-stacks of various sizes also demonstrate excellent agreement between direct simulations and WSA based calculations thus completely confirming the theory presented above.[44]

Until now, we have dealt only with transmission length $l_T(\lambda)$, which was defined through an average value. However, additional information can be obtained from the transmission length $l_N(\lambda)$ for a single realization,

$$\frac{1}{l_N} = -\frac{\ln|T_N|}{N}.$$

In the localized regime, i.e., for a sufficiently long M-stack with $N \gg l$, the transmission length for a single realization $l_N(\lambda)$ is practically nonrandom and coincides with $l_T(\lambda)$ and l, while in the ballistic region it fluctuates. The data displayed in Fig. 3 enables us to estimate the difference between the transmission length $l_T(\lambda)$ (solid line) and the transmission length $l_N(\lambda)$ for a single randomly chosen realization (dashed line), and the scale of the corresponding fluctuations. Both curves are smooth, coincide in the localized region, and differ noticeably in the ballistic regime. The separate discrete points in Fig. 3 present the values of

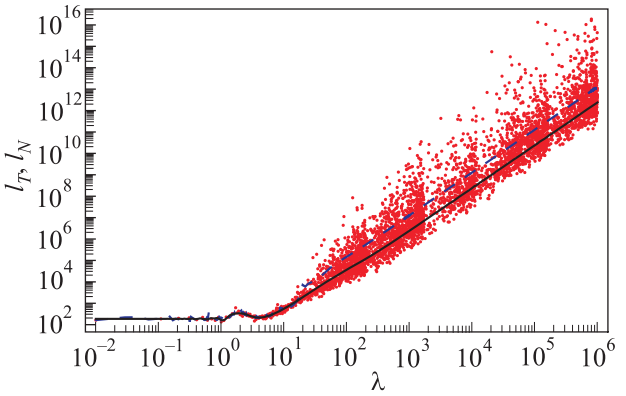

FIG. 3. (Ref. 44) Transmission lengths l_T (solid black line), and the transmission length for a single realization l_N (dashed blue line) vs. λ for an M-stack with $Q_\nu = 0.25$, $Q_d = 0.2$, and $N = 10^4$ layers. Each separate point corresponds to a particular wavelength with its own realization of a random stack.

transmission length $l_N(\lambda)$ calculated for different randomly chosen realizations. It is evident that fluctuations in the ballistic region become more pronounced with increasing wavelength.

3.3. Homogeneous stack

For an H-stack composed entirely of either normal material or metamaterial layers, the transmission length obtained within the WSA is

$$\frac{1}{l_T} = \frac{1}{l} + \frac{1}{N}\mathrm{Re}\left\{\frac{\langle r\rangle^2}{(1-\langle t^2\rangle)^2}\left[1-\exp\left(-\frac{N}{\bar{l}} - i\frac{N}{\bar{l}_b}\right)\right]\right\}, \tag{3.18}$$

where $\bar{l}$ is the crossover length Eq. (3.10), and $\bar{l}_b$ is the ballistic crossover length defined by the equation

$$\frac{1}{\bar{l}_b} = -\mathrm{Im}\ln\langle t^2\rangle.$$

The H-stack localization length l is

$$\frac{1}{l} = -\langle\ln|t|\rangle - \mathrm{Re}\frac{\langle r\rangle^2}{1-\langle t^2\rangle}, \tag{3.19}$$

where r, t are the transmission and reflection coefficients of an R layer (for L layers they should be replaced with r^* and t^*, however, this does not change the final result due to the real part operation Re).

Here, we consider the simplest lossless model ($\sigma = 0$) with only refractive index disorder (i.e., $Q_d = 0$). In contrast to the M-stack case (see Sec. 3.2), where a minimal model, manifesting all the common features of M-stack transmission properties, necessarily includes an additional random parameter (in the previous subsection it is the layer thickness), for the H-stack it is sufficient to include only one such parameter. As earlier, we assume uniform distribution of refractive index fluctuations with the width $2Q_\nu$. In this case, the short-wave asymptotic value of the localization length coincides with that of the M-stack Eq. (3.12), and, similarly to the M-stack, transmission through short H-stacks with $N \lesssim Q_\nu^{-2}$ is always ballistic. So, below we consider long stacks $NQ_\nu^2 \gg 1$.

In the long-wave region $\lambda \gg 1$, the three characteristic lengths entering Eq. (3.18) asymptotically are

$$l = \frac{3\lambda^2}{2\pi^2 Q_\nu^2}, \quad \bar{l} = \frac{\lambda^2}{8\pi^2 Q_\nu^2}, \quad \bar{l}_b = \frac{\lambda}{4\pi}. \tag{3.20}$$

The main contribution to the long-wave and short-wave asymptotic value of localization length is related to the first term in Eq. (3.19). Thus, localization length of the H-stack in these two limits is well described by the single scattering approximation. The long-wave asymptotic value of the H-stack localization length differs from that of the M-stack and coincides with the reciprocal of its Lyapunov exponent Eq. (3.17) and the ballistic length Eq. (3.15).

We also calculated the H-stack Lyapunov exponent. It is described by the same Eq. (3.16) as that for the M-stack, thus the reciprocals of the Lyapunov exponents for both types of stacks have the same asymptotic form Eq. (3.17). This coincidence was established analytically in a wider spectral region in Ref. 53.

Long H-stacks with $N \gg Q_\nu^{-2}$ in the long-wave region $\lambda \gg 1$ manifest both ballistic and localized behavior. Transition between these regimes is governed by two characteristic wavelengths defined by Eq. (3.11). Similarly to the M-stack case, they are proportional to $Q_\nu\sqrt{N}$, differ only by a numerical multiplier, and satisfy the inequality $\lambda_1(N) < \lambda_2(N)$.

At the starting part of the long-wave region $1 \ll \lambda \ll \lambda_1(N)$ the transmission length l_T coincides with the localization length l and has an asymptotic value described by Eq. (3.20). Then, after passing the transition region $\lambda_1(N) \ll \lambda \ll \lambda_2(N)$, ballistic regime $\lambda \gg \lambda_2(N)$ starts. In this regime transmission length coincides with the ballistic length $b(\lambda)$ described by equation

$$\frac{1}{b(\lambda)} = \frac{2\pi^2 Q_\nu^2}{3\lambda^2}\left[1 + \frac{NQ_\nu^2}{12}\left(\frac{\sin(\lambda_3(N)/2\lambda)}{\lambda_3(N)/2\lambda}\right)^2\right],$$
$$\lambda_3(N) = 4\pi N, \tag{3.21}$$

obtained through the expansion of exponent $\exp(-N/\bar{l})$ in Eq. (3.18).

Due to the appearance of an additional characteristic wavelength $\lambda_3(N)$ determined by equation $N = \bar{l}_b(\lambda_3(N))$, where $\bar{l}_b$ is the ballistic crossover length Eq. (3.20), the ballistic region is naturally divided onto two subregions. The first of them defined by inequalities $\lambda_2(N) \ll \lambda \ll \lambda_3(N)$ is near the ballistic region, where ballistic length coincides with the localization length,

$$b_n(\lambda) = \frac{3\lambda^2}{2\pi^2 Q_\nu^2}. \tag{3.22}$$

Thus, crossover from the localized regime to the ballistic one is not accompanied by any change of the transmission length. In the ballistic transition region $\lambda \sim \lambda_3(N)$ the second term in Eq. (3.21) becomes essential leading to oscillations of the ballistic length. Finally, in the far ballistic region $\lambda \gg \lambda_3(N)$ expansion of the sine in Eq. (3.21) shows that for long stacks the second term in this equation dominates, and the far ballistic length is

$$\frac{1}{b_f(\lambda)} = \frac{2\pi^2 Q_\nu^2}{3\lambda^2}\left(1 + \frac{NQ_\nu^2}{12}\right) \approx \frac{N\pi^2 Q_\nu^4}{18\lambda^2}. \qquad (3.23)$$

The region $\lambda \geq \lambda_3(N)$ possesses a simple physical interpretation. Indeed, in this subregion the wavelength essentially exceeds the stack size, and so we may consider the stack as a single weakly scattering uniform layer with an effective dielectric permittivity[44]

$$\varepsilon_{\text{eff}} = \left(1 + \frac{Q_\nu^2}{3}\right).$$

Substitution of this value into the text-book formula for reflectivity of a uniform sample leads immediately to the far long-wavelength ballistic length Eq. (3.23). We note that because of the effective uniformity of the H-stack in the far ballistic region, the transmission length on a single realization is a less fluctuating quantity than that in the near ballistic region, where it fluctuates strongly, as it does over the entire ballistic region for M-stacks.

Numerical calculations for an H-stack show excellent agreement between direct simulations and calculations based on the WSA: the corresponding curves can not be distinguished. Figure 2 explicitly demonstrates that transmission length conserves the same analytical form in the localized long-wave region and near the ballistic region. For the considered stacks with $N = 10^3$ transmission spectrum features corresponding to the transition between two ballistic subregions can not manifest. Indeed, the transition occurs at wavelength $\lambda \sim 10^4$ that is out of range in this figure.

To study the crossover from near to far ballistic behavior consider the transmission lengths of H-stacks with $N = 10^3$ and 10^4 over the wavelength range extended up to $\lambda \sim 10^6$ plotted in Fig. 4. Transition from the localized to the near ballistic regime occurs without any change in the analytical dependence of transmission length, however, the crossover from the near to the far ballistic regime is accompanied by a change in the analytical dependence that occurs at $\lambda = \lambda_2(N)$, which for these stacks is on the order of 10^4 and 10^5, respectively. The crossover is accompanied by prominent oscillations described by Eq. (3.21). Finally, we note that vertical displacement between the moderately long and extremely long-wavelength ballistic asymptotic values does not depend on the wavelength, but grows with the size of the stack according to the law

$$\ln\frac{b_n}{b_f} = \ln\frac{NQ_\nu^2}{12},$$

which stems from Eqs. (3.22) and (3.23).

A detailed study of the average reflectivity of H-stacks with various lengths in the entire long-wave region[44] also completely confirms theoretical predictions formulated above.

Consider now the statistical properties of the H-stack transmission length on a given realization $l_N(\lambda)$. For very long stacks $N \to \infty$ this length becomes practically nonrandom in both the localized region due to self-averaging of the Lyapunov exponent, and the far ballistic region due to self-averaging nature of effective dielectric permittivity. For less long stacks, transmission length l_T also fluctuates even in the far ballistic region. However, for sufficiently long stacks these fluctuations are essentially suppressed since they must vanish in the limit as $N \to \infty$. This is demonstrated in Fig. 5, where transmission length l_T (solid line) and the transmission length $l_N(\lambda)$ for a single randomly chosen realization (dashed line) are plotted. Like in the M-stack case, the H-stack single realization transmission length in the near ballistic region is a complicated and irregular function, similar to the well known "magneto fingerprints" of magnetoconductance of a disordered sample in the weak localization regime.[75] This statement is supported by the displayed in Fig. 5 set of separate discrete points, each of them presenting transmission length calculated for a different randomly chosen realization.

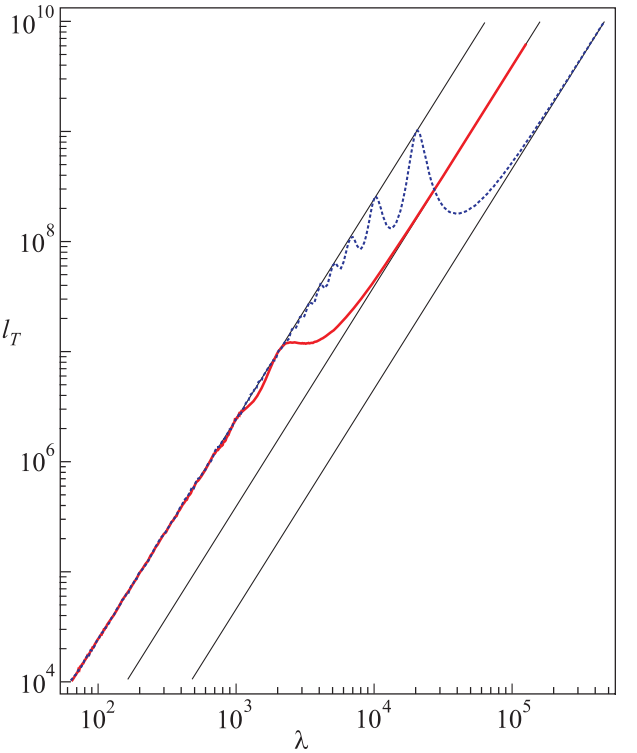

FIG. 4. (Ref. 44) Transmission length l_T vs. λ for H-stacks of $N = 10^3$ (solid line) and 10^4 (dotted line) layers (numerical simulation and WSA). Long-wave asymptotic values for the ballistic length in the near and far ballistic regions are plotted in thin solid lines.

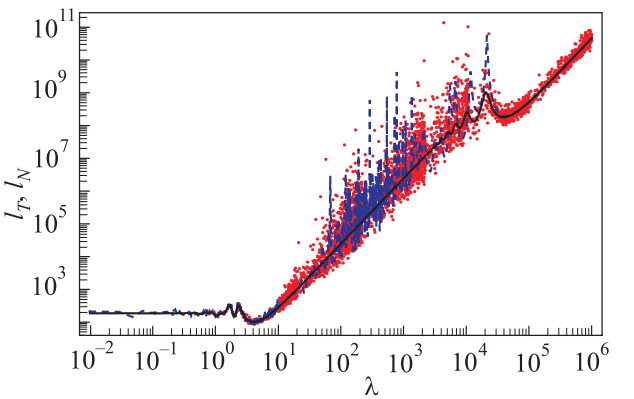

FIG. 5. (Ref. 44) Transmission lengths l_T (solid black line) and the transmission length for a single realization l_N (dashed blue line) vs. λ for an H-stack with $Q_\nu = 0.25$, $Q_d = 0.2$, and $N = 10^4$ layers. Each separate point corresponds to a particular wavelength with its own realization of a random stack.

3.4. Transmission resonances

An important signature of the localization regime is the presence of transmission resonances (see, for example, Refs. 76–78), which appear in sufficiently long, open systems, and which are a "fingerprint" of a given realization of disorder. These resonances manifest themselves as narrow peaks of transmittivity $|T_N|^2$ on a given realization as a function of wavelength λ. Figure 6 (Ref. 43) presents a single realization of transmittance $|T_N|^2$ as a function of λ for an M-stack (dashed line) and for the corresponding H-stack of $N=10^3$ layers (solid line). It is evident that resonance properties exhibited by homogeneous and mixed media serve as another (in addition to the behavior of the localization length) discriminating characteristic of these two media.

Indeed, there are no resonances for the M-stack for $\lambda \gtrsim 4$, while the disordered homogeneous stack exhibits well pronounced resonances over the entire spectrum.

Note that the dotted curve in Fig. 6 describes resonance properties of a periodic $Q_d=0$ comparatively short M-stack with only refractive index disorder (RID). An important feature of such a stack is the lack of phase accumulation over its total length: in the particular realization of Fig. 6, the accumulated phase of the wave in the mixed stack never exceeds $\pi/2$. Therefore, to subdue such a suppression of phase accumulation one essentially needs to enlarge the stack size or to switch on additional (thickness Q_d or magnetic permittivity μ) disorder.

The first possibility is demonstrated in Fig. 7, where transmittance spectra $|T|^2$ (λ) for a realization of two different M-stacks with two lengths $N=10^3$ and $N=10^5$ and only refractive index disorder is displayed. It is readily seen that while the resonances in the shorter stack (dashed line) at $\lambda \geq 5$ do not exist at all, they do appear in the same region for the longer sample (solid line).

The second way to generate transmission resonances is to introduce additional disorder. This is confirmed by the transmittance spectra for a realization, of two M-stacks of the same size $N=10^3$ with only refractive index disorder (dashed line), and both (thickness and refractive index) types of disorder (solid line), plotted in Fig. 8. It is clear that while the RID M-stack with this length, is too short to exhibit transmission resonances at $\lambda > 3$, resonances do emerge at longer wavelengths for the M-stack with thickness disorder.

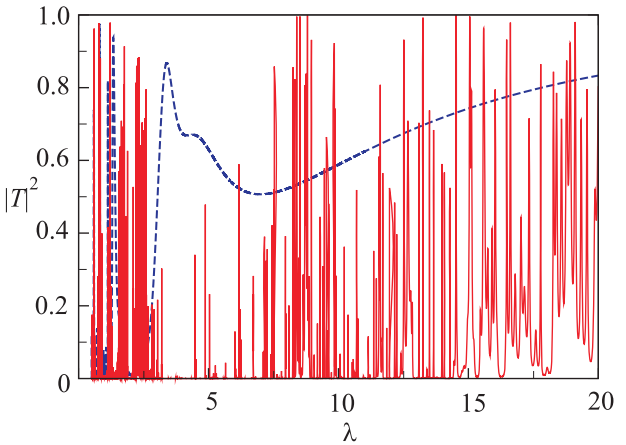

FIG. 6. (Ref. 43) Transmittance $|T|^2$ vs. λ for a single realization ($Q=0.25$, $N=10^3$). Solid: normal H-stack, dotted: M-stack.

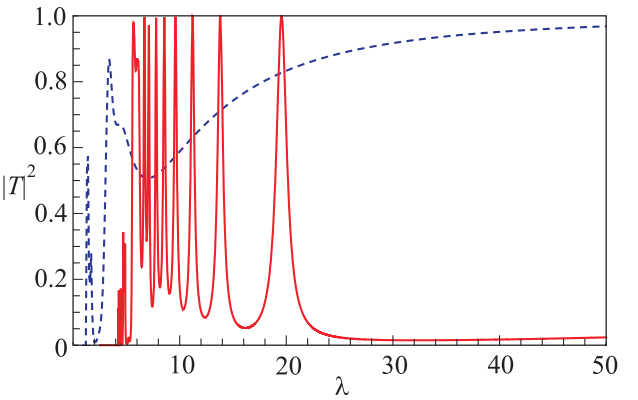

FIG. 7. (Ref. 44) Single realization transmittance $|T|^2$ vs. wavelength λ for RID M-stacks with $Q_\nu=0.25$ and $Q_d=0$ for $N=10^5$ layers (solid line) and $N=10^3$ layers (dotted line).

Transmission resonances are responsible for the difference between two quantities that characterize the transmission, namely transmittance logarithm $\langle \ln |T|^2 \rangle$ and logarithm of average transmittance $\ln\langle |T|^2 \rangle$. The former reflects the properties of a typical realization, while the latter value is often very sensitive to the existence of almost transparent realizations associated with the transmission resonances. Moreover, in some cases namely small number of such realizations contribute mainly to the average transmittance.

Thus, the ratio of the two quantities mentioned above

$$s = \frac{\langle \ln |T|^2 \rangle}{\ln \langle |T|^2 \rangle}$$

is a natural characteristic of the transmission resonances. In the absence of resonances this value is close to unity, while in the localization regime $s>1$. In particular, this ratio takes the value 4 in the high-energy part of the spectrum of a disordered system with Gaussian white-noise potential.[2]

Consider the ratio $s(\lambda)$ as a function of wavelength for RID M- and H-stacks and for the corresponding stacks with thickness disorder, plotted in Fig. 9. In all cases, the stack length is $N=10^3$. It is evident that for the RID M-stack $s(\lambda)\approx 1$, i.e., the length of this M-stack is too short for the localization regime to be realized. In the other three cases, however, $s(\lambda) \gtrsim 2$, which means that localization takes place even in such comparatively short stacks.

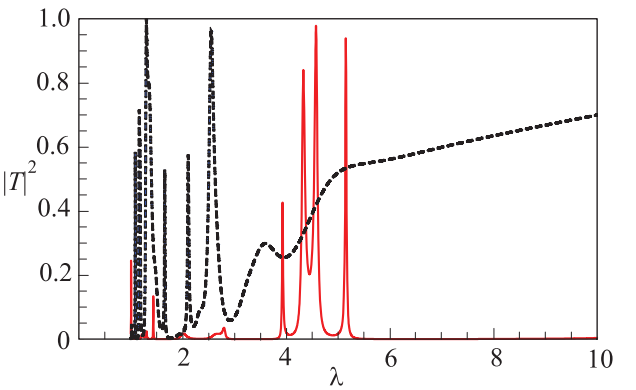

FIG. 8. (Ref. 44) Single realization transmittance $|T|^2$ vs. λ for an M-stack of $N=10^3$ layers with $Q_\nu=0.25$. Solid line corresponds to an M-stack with $Q_d=0.2$, and the dashed line – to an M-stack with no thickness disorder, i.e., $Q_d=0.0$.

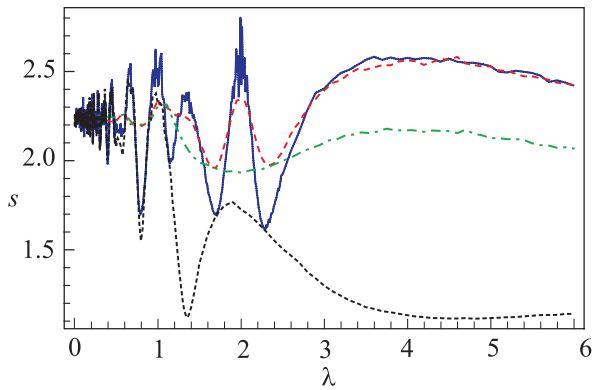

FIG. 9. (Ref. 44) Ratio s vs. wavelength λ for $Q_\nu = 0.25$ and stack length $N = 10^3$. Solid and dashed curves are for the RID H-stack and H-stack with $Q_d = 0.2$, respectively. The middle dashed-dotted curve is for an M-stack with $Q_d = 0.25$, and the bottom dotted line is for a RID M-stack.

3.5. Polarization effects

The results obtained above for normal incidence can be easily generalized to the case of oblique incidence. Here, all the characteristic lengths and wavelengths depend on the angle of incidence θ, and s- and p-polarizations should be considered separately. Qualitatively new features appear: essential enlightening in vicinity of the Brewster angle and appearance of supercritical regime induced by total internal reflection. We describe these new properties within the framework of the model defined in a previous section (Sec. 3.1).

General expressions for transmission length for both M-stacks (Eqs. (3.7)–(3.10) and H-stacks (Eqs. (3.18) and (3.19)) as well as general expressions Eq. (3.2) for transmission and reflection coefficients of a single layer remain the same as in the case of normal incidence. However, explicit expressions for the parameters entering these coefficients are changed. The Fresnel interface reflection coefficient is now given by

$$\rho = \frac{\mathcal{Z}\cos\theta_\nu - \cos\theta}{\mathcal{Z}\cos\theta_\nu + \cos\theta}, \qquad \mathcal{Z} = \begin{cases} Z^{-1}, & s\text{-polarization}, \\ Z, & p\text{-polarization}. \end{cases} \tag{3.24}$$

Here, the characteristic angle θ_ν and the layer impedance Z relative to the background (free space) according to Eq. (3.4) are

$$\cos\theta_\nu = \sqrt{1 - \frac{\sin^2\theta}{\nu^2}}, \quad Z = \sqrt{\frac{\mu}{\varepsilon}} = \frac{1}{1+\delta_\nu}.$$

Then the phase shift β is

$$\beta = kd\nu\cos\theta_\nu, \quad k = 2\pi/\lambda. \tag{3.25}$$

The characteristic angle conserves its direct geometrical meaning for the incidence angle $\theta \le \theta_c$ (subcritical incidence angle), where the critical angle is

$$\theta_c = \sin^{-1}(1 - Q_\nu).$$

For the supercritical incidence angle $\theta \ge \theta_c$ the values of θ_ν are complex.

Below we mention only the final asymptotical expressions for some characteristic lengths of the problem in the typical cases. We take into account both types of disorder, however, in all final results we keep only the leading terms and omit the higher order corrections with respect to refractive index and thickness fluctuations $Q_{\nu,d}$.

In the short-wave limit, localization length is the same for M- and H-stacks. In the subcritical region of incidence angles it is

$$\frac{1}{l} \approx \frac{Q_\nu^2}{12\cos^4\theta}\begin{pmatrix} 1, & s\text{-polarization}, \\ \cos^2 2\theta, & p\text{-polarization}. \end{pmatrix}$$

Note that for p-polarization this expression acquires an angle dependent multiplier that vanishes at the Brewster angle $\theta = \pi/4$. Accounting for the next term we obtain the localization length at the Brewster angle

$$l = 45/4Q_\nu^4,$$

which is Q_ν^{-2} times larger than that far from the Brewster angle and than that for s-polarization in the same shortwave limit.

At the incidence angle $\theta > \theta_c$ total internal reflection occurs and the WSA fails. If the supercriticality $\theta - \theta_c$ is not extremely small, then the exponent $2i\beta$ in Eq. (3.2) is real and negative, and thus the magnitude of the single layer transmission coefficient is exponentially small. This results in the attenuation length for both polarizations

$$\frac{1}{l_{\text{att}}} = \operatorname{Im}\langle\beta\rangle = k\operatorname{Im}\langle d\sqrt{\sin^2\theta - \nu^2}\rangle = \frac{k\sin^2\theta}{8Q_\nu}(\pi - 2\theta_0 - \sin 2\theta_0), \quad \sin\theta_0 = \frac{\sin\theta_c}{\sin\theta}.$$

Due to $\propto k$ dependence, in the short-wave limit $l_{\text{att}} \to \infty$, and transmission length in the supercritical region of the angles of incidence coincides with the attenuation length. However, for the same reason, at long-waves the attenuation contribution can be neglected, and the main contribution to transmission length is due to Anderson localization.

In the long-wave region, H- and M-stacks demonstrate different behavior, and we describe them separately.

a) Homogeneous stacks

For s-polarization, the long-wave asymptotic value of transmission length is similar to that for normal incidence Eq. (3.21)

$$\frac{1}{l_T} = \frac{2\pi^2 Q_\nu^2}{3\lambda^2\cos^2\theta}\left[1 + \frac{NQ_\nu^2}{12}\left(\frac{\sin(2\pi N\cos\theta/\lambda)}{(2\pi N\cos\theta)/\lambda}\right)^2\right].$$

This expression describes the localized regions, as well as both ballistic subregions.

In the case of a p-polarized wave, the localization length is given by

$$\frac{1}{l} = \frac{2\pi^2 Q_\nu^2\cos^2 2\theta}{3\lambda^2\cos^2\theta} + \frac{\pi^2 Q_\nu^4}{6\cos^4\theta} \times \left(1 - \frac{19}{6}\cos 2\theta + \frac{7}{15}\cos 4\theta + \frac{19}{30}\cos 6\theta\right).$$

At the Brewster angle $\theta = \pi/4$ the first term vanishes, and transmission length is

$$\frac{1}{l} = \frac{16\pi^2 Q_\nu^4}{45\lambda^2}. \tag{3.26}$$

b) Mixed stacks

Reciprocal transmission length for an *s*-polarized wave is

$$\frac{1}{l_T} = \frac{k^2 Q_\nu^2}{3\cos^2\theta}\left(\frac{1}{2} - \frac{1 - f(N\alpha_S)}{3 + \zeta\cos^4\theta}\right),$$
$$\alpha_S = \frac{k^2 Q_\nu^2}{3\cos^2\theta}(3 + \zeta\cos^4\theta), \tag{3.27}$$

where the function f and parameter ζ are defined in Sec. 3.2. Equation (3.27) describes the transition from localization to ballistic propagation at long wavelengths. In the limit $N \to \infty$ transmission length tends to localization length

$$l = \frac{3\lambda^2\cos^2\theta}{2\pi^2 Q_\nu^2}\frac{3 + \zeta\cos^4\theta}{1 + \zeta\cos^4\theta},$$

while the opposite extreme, i.e., as $N \to 0$, gives the ballistic length

$$b = \frac{3\lambda^2\cos^2\theta}{2\pi^2 Q_\nu^2},$$

which coincides with that for an H-stack in *s*-polarization.

For *p*-polarized waves incident at angles away from the Brewster angle, transmission length is given by

$$\frac{1}{l_T} = \frac{k^2 Q_\nu^2\cos^2 2\theta}{3\cos^2\theta}\left(\frac{1}{2} - \frac{1 - f(N\alpha_p)}{2 + \cos^2 2\theta + \zeta\cos^4\theta}\right),$$
$$\alpha_p = \frac{k^2 Q_\nu^2}{3\cos^2\theta}(2 + \cos^2 2\theta + \zeta\cos^4\theta). \tag{3.28}$$

Localization length is deduced from Eq. (3.28) by taking the limit as $N \to \infty$

$$l = \frac{3\lambda^2\cos^2\theta}{2\pi^2 Q_\nu^2\cos^2 2\theta}\frac{2 + \cos^2 2\theta + \zeta\cos^4\theta}{\cos^2 2\theta + \zeta\cos^4\theta}.$$

Correspondingly, ballistic length is obtained by calculating the limit as $N \to 0$

$$b = \frac{3\lambda^2\cos^2\theta}{2\pi^2 Q_\nu^2\cos^2 2\theta}.$$

At the Brewster angle $\theta = \pi/4$, accounting for the higher order corrections to r.h.s. of Eq. (3.28), we obtain the transmission length, and the result is the same as Eq. (3.26) that for an H-stack.

All analytical predictions are confirmed by numerical calculations. As in the case of normal incidence, theoretical curves based on WSA mostly can not be distinguished from those obtained by direct simulations. The results obtained are mostly similar to those of normal incidence. Therefore, here we mention only some of them. Specifically, those which differ from those presented above.

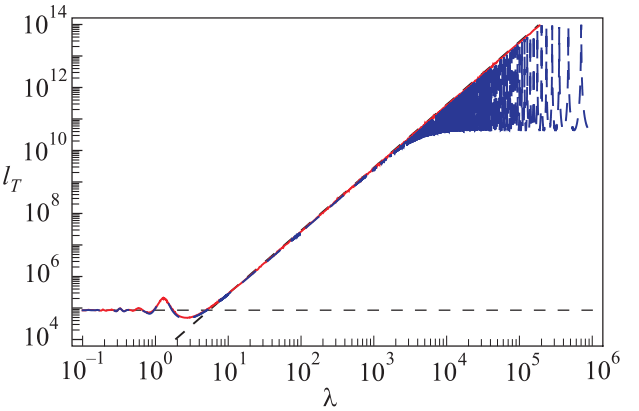

FIG. 10. (Ref. 45) Transmission length l_T vs. λ for an M-stack in *p*-polarized light with $Q_\nu = 0.1$, $Q_d = 0.2$, and $N = 10^6$, at the Brewster angle $\theta = 45°$ (red solid line). The blue dashed line shows results for *s*-polarization and an H-stack, replotted for comparison.

In Fig. 10 the transmission length spectrum for an M-stack of length $N = 10^6$ in *p*-polarized light with other parameters $Q_\nu = 0.1$, $Q_d = 0.2$, $N_r = 10^4$, and incidence angle $\theta = \pi/4$ is displayed. The chosen angle of incidence is less than the critical angle $\theta_c = \arcsin 0.9 = 64.16°$, and coincides with the Brewster angle for a single layer with mean refractive index $\nu = \pm 1$. The results of the numerical simulation and the WSA analytical forms coincide and are displayed with a single solid red line. Localization occurs for $\lambda \le \lambda_1 \approx 19$, while the transition from localization to ballistic propagation occurs at $\lambda \sim \lambda_1$. In contrast to the case of *s*-polarization, this transition is not accompanied by a change of scale and is given by the same wavelength dependence. Transition from near to far ballistic length is accompanied by oscillation of transmission lengths, which are much more pronounced in comparison to the case of normal incidence.

Now, consider a supercritical case, where the angle of incidence $\theta = 75°$ exceeds the critical angle. In Fig. 11 the transmission length spectrum for *s*-polarized light is presented. The results of both the exact numerical calculation (red solid line) and the analytic form (long dashed blue curve) are displayed. The short-wave (dashed dotted line) and the long-wave (black dashed line) asymptotic values of transmission length, respectively, coincide with numerical results for $\lambda \le 1$ and $200 \le \lambda$. In the intermediate region $1 \le \lambda \le 200$, however, the theoretical description

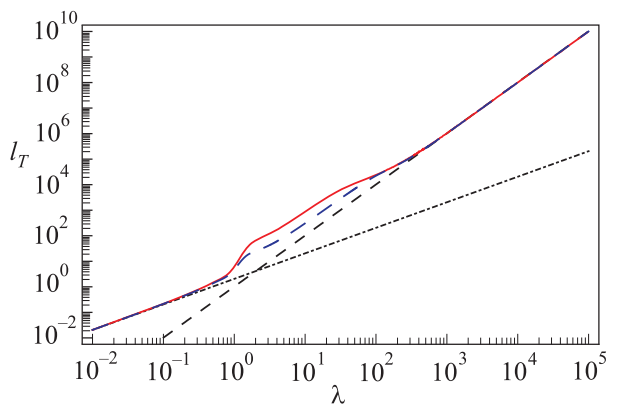

FIG. 11. (Ref. 45) Transmission length l_T vs. λ for an M-stack in *s*-polarized light with $Q_\nu = 0.1$, $Q_d = 0.2$, and $N = 10^4$, and for the supercritical incidence angle $\theta = 75°$. Red solid curve: numerical simulations; blue dash curve: analytical form.

underestimates the actual transmission length since the WSA is no longer valid for the chosen, supercritical angle of incidence. For p-polarization the results are qualitatively the same, but with an even more pronounced discrepancy at intermediate wavelengths.

We also consider the angular dependence of transmission length for mixed stacks. In Fig. 12 the transmission length l_T as a function of angle θ for a stack of length $N=10^6$ at two wavelengths $\lambda=0.1$ and $\lambda=1$ is displayed. In either case, the calculated transmission length does not exceed the stack length, and so, for subcritical angles our calculations display the true localization length. For the shorter wavelength $\lambda=0.1$ the form of transmission length for both polarizations is similar to that observed for homogeneous stacks.

Figure 12(b) displays the results for intermediate wavelength $\lambda=1$ with the lower solid red and blue dashed curves, respectively, displaying the results of numerical simulations and analytical predictions for s-polarization (bottom curves), while the upper solid green and brown dashed curves display simulations and analytical predictions for p-polarization. The agreement between simulations and the theoretical form is again excellent for angles of incidence less than the critical angle, $\theta<\theta_c$, while for angles greater than the critical angle the discrepancies that are evident are again explicable by the breaking down of the WSA at extreme angles of incidence.

3.6. Dispersive metamaterials

Real metamaterials are always dispersive materials. Here we consider the dispersive model of a stack composed

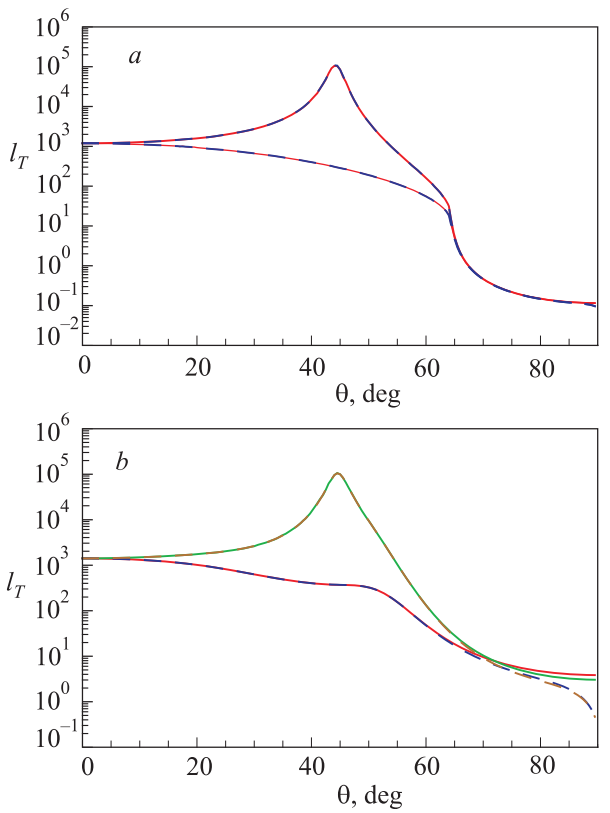

FIG. 12. (Ref. 45) Transmission length l_T vs. incidence angle θ for a mixed stack with $Q_\nu=0.1$, $Q_d=0.2$, for $\lambda=0.1$ (a), and $\lambda=1$ (b). The top and bottom curves are, respectively, for p- and s-polarizations.

of metalayers with the same thickness d and random dielectric permittivity and magnetic permeability described by the Lorentz oscillator model

$$\varepsilon(f)=1-\frac{f_{ep}^2-f_e^2}{f^2-f_e^2+i\gamma f}, \tag{3.29}$$

$$\mu(f)=1-\frac{f_{mp}^2-f_m^2}{f^2-f_m^2+i\gamma f}. \tag{3.30}$$

Here, f is circular frequency, f_m and f_e are the resonance frequencies, and γ is the phenomenological absorption parameter. In this model, disorder enters the problem through random resonance frequencies so that

$$f_e=\overline{f}_e(1+\delta_e),\quad f_m=\overline{f}_m(1+\delta_m),$$

where $\overline{f}_{e,m}=\langle f_{e,m}\rangle$ are the mean resonance frequencies (with the angle brackets denoting ensemble averaging), and $\delta_{e,m}$ are independent random values distributed uniformly in the range $[-Q_{e,m}, Q_{e,m}]$. The characteristic frequencies f_{mp} and f_{ep} are not random. Therefore, in lossless media ($\gamma=0$) both magnetic permeability and dielectric permittivity vanish with their mean values, $\overline{\varepsilon}(f)=\langle\varepsilon(f)\rangle$, and $\overline{\mu}(f)=\langle\mu(f)\rangle$ at frequencies $f=f_{ep}$ and $f=f_{mp}$, respectively, i.e.,

$$\mu(f_{mp})=\overline{\mu}(f_{mp})=0,\quad \varepsilon(f_{ep})=\overline{\varepsilon}(f_{ep})=0.$$

Following Refs. 79 and 80, in our numerical calculations we choose the layer thickness $d=0.003$ m and the values of characteristic frequencies $f_{mp}=10.95$ GHz, $f_{m0}=\overline{f}_m=10.05$ GHz, $f_{ep}=12.8$ GHz, $f_{e0}=\overline{f}_e=10.3$ GHz, and $\gamma=10$ MHz, which fit the experimental data given in Ref. 79. That is, we are using a model based on experimentally measured values for the metamaterial parameters. Then we choose the maximal widths of distributions of the random parameters $\delta_{e,m}$ as $Q_{e,m}=5\cdot10^{-3}$, corresponding to weak disorder.

We focus our study on the frequency region 10.40 GHz $<f<$ 11.00 GHz. In the absence of absorption and disorder, for these frequencies the dielectric permittivity and magnetic permeability of the metamaterial layers vary over the intervals $-26.9<\varepsilon<-2.9$ and $-1.64<\mu<0.055$. The refractive index is negative in the frequency range 10.40 GHz $<f<f_{mp}=10.95$ GHz, as shown in the inset of Fig. 13. However, at $f_{mp}=10.95$ GHz the magnetic permeability changes sign, and the metamaterial changes from being double negative (DNM) to single negative (SNM). As we show later, such changes have a profound effect on localization properties.

We study the transmission of a plane wave, either s- or p-polarized, and incident on a random stack from free space at an angle of incidence θ_0.

In the previous subsections we have described and used an effective WSA method developed and elaborated on in Refs. 43–45 for the study of transport and localization in random stacks composed of weakly reflecting layers.

In the dispersive case, reflection from a single layer located in free space is not necessarily weak, in which instance the method seems inapplicable. However, we can replace each layer with the same layer surrounded by infinitesimally thin layers of a background medium with permittivity and permeability given by the mean values of

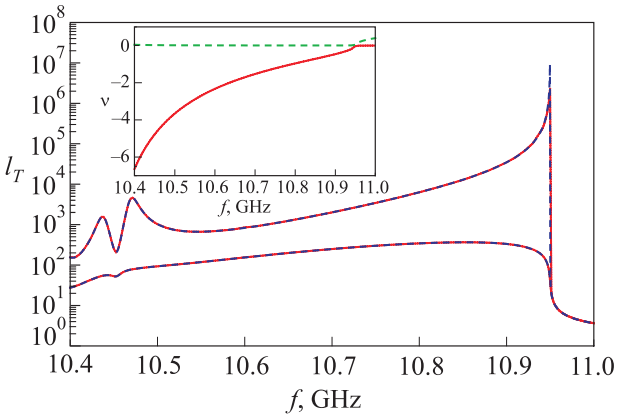

FIG. 13. (Color online) (Ref. 46) Transmission length l_T vs. frequency f at normal incidence ($\theta_0 = 0$) for a metamaterial stack without absorption (top curve) and in the presence of absorption (bottom curves). Red solid curves display numerical simulations, while blue dashed curves show analytical predictions. Inset: the real (red solid line) and imaginary (green dashed line) part of the metamaterial layer refractive index.

$\overline{\varepsilon}(f) \equiv \langle \varepsilon(f) \rangle$ and $\overline{\mu}(f) \equiv \langle \mu(f) \rangle$, respectively. In the considered case of weakly disordered stacks we can use the WSA for all the layers except the two "leads" connecting the stack with free space on the very left and the very right, where it ends. Localization characteristics, which are intrinsic properties of the stack, do not feel the leads. Their role is restricted to only change the coupling conditions for the random stack through the angle of incidence, transforming it from its given value θ_0 outside the lead to the frequency dependent refracted value θ_b inside the lead. These angles are related by the Snell law $\sin\theta_0 = \sin\theta_b \sqrt{\overline{\varepsilon}(f)\overline{\mu}(f)}$. It is important to note that while in the localized regime the input and output leads are of no significance, they do play a crucial role when localization breaks down (see below).

Single layer scattering is described by Eqs. (3.2), where, according to Eqs. (3.1) and (3.25),

$$\beta_n = kd\nu_n \cos\theta_n,\ \nu_n = \sqrt{\varepsilon_n \mu_n}, \tag{3.31}$$

and $k = 2\pi/\lambda = 2\pi f/c$ is the free space wavenumber. The interface Fresnel reflection coefficient ρ_n is given by

$$\rho_n = \frac{Z_b \cos\theta_b - Z_n \cos\theta_n}{Z_b \cos\theta_b + Z_n \cos\theta_n}. \tag{3.32}$$

Impedances Z_b and Z_n are

$$Z_b = \begin{cases} \sqrt{\overline{\mu}/\overline{\varepsilon}}, & p\text{-polarization}, \\ \sqrt{\overline{\varepsilon}/\overline{\mu}}, & s\text{-polarization}, \end{cases}$$

$$Z_n = \begin{cases} \sqrt{\mu_n/\varepsilon_n}, & p\text{-polarization}, \\ \sqrt{\varepsilon_n/\mu_n}, & s\text{-polarization}, \end{cases}$$

and angles θ_b and θ_n satisfy Snell's law

$$\nu_n \sin\theta_n = \overline{\nu}\sin\theta_b = \sin\theta_0, \quad \overline{\nu} = \sqrt{\overline{\varepsilon}\overline{\mu}}. \tag{3.33}$$

General WSA expressions (3.19) and (3.9) for the localization length of monotype and mixed stacks remain valid for stacks composed of dispersive stacks. To study localization properties of such stacks we should insert there the same single layer scattering coefficients Eq. (3.2) with dispersive phase shift Eq. (3.31) and Fresnel coefficient Eq. (3.32).

Dispersion essentially affects transport properties of the disordered medium. In particular, it can lead to suppression of localization either at some angle of incidence or at a selected frequency, or even in a finite frequency range. Below we consider the first two cases for an H-stack composed of L-layers. The third case will be considered further in Sec. 3.7.

In the presence of dispersion, the long-wave asymptotic value of localization length is

$$\frac{1}{l} = \frac{\pi^2 d^2}{2\lambda^2(f)} \left(\frac{\langle \mu^2 \rangle - \langle \mu \rangle^2}{\langle \mu \rangle^2} + \frac{\langle \varepsilon^2 \rangle - \langle \varepsilon \rangle^2}{\langle \varepsilon \rangle^2} \right), \tag{3.34}$$

where ε and μ are given by Eqs. (3.29) and (3.30), and frequency-dependent wavelength in the medium is

$$\lambda(f) = \frac{c}{f\sqrt{\varepsilon(f)\mu(f)}}$$

and can be large even when the wavelength of incident signal, $\lambda = c/f$, is small.

Accordingly, the inverse localization length

$$l^{-1} \propto f^2 \varepsilon(f)\mu(f)$$

becomes small not only at low frequencies $f \to 0$, but also in vicinity of μ- or ε-zero points. For example, as frequency approaches the μ-zero point from below (i.e., $f \to f_{mp}^-$) in an H-stack of metamaterial layers, $\mu(f)$ for any realization is proportional to the difference $(f_{mp} - f)$, and the expression for localization length diverges with $(f_{mp} - f)^{-1}$. Formally, this divergence can be treated as delocalization, however, the limiting value $1/l = 0$ means nothing but the absence of exponential localization. Moreover, when localization length becomes larger than the size of the stack, ballistic transport occurs, and the transmission coefficient is determined by transmission length, rather than by the localization length.

To calculate the transmission coefficient for this case we consider, for the sake of simplicity, a stack with only ε-disorder. Here, the transfer matrix of the nth layer at $f = f_{mp}$ has the form

$$\mathcal{T}_n \equiv \mathcal{T}(\epsilon_n) = \begin{Vmatrix} 1+\epsilon_n & \epsilon_n \\ -\epsilon_n & 1-\epsilon_n \end{Vmatrix},$$

where $\epsilon_n = ikd\varepsilon_n/2$.

As a consequence of the easily verified group property

$$\mathcal{T}(\epsilon_1)\mathcal{T}(\epsilon_2) = \mathcal{T}(\epsilon_1 + \epsilon_2),$$

it follows that the stack transfer matrix $\mathcal{T}$ is

$$c\mathcal{T} = \prod_{n=1}^{N} \mathcal{T}(\epsilon_n) = \begin{Vmatrix} 1+\mathcal{E} & \mathcal{E} \\ -\mathcal{E} & 1-\mathcal{E} \end{Vmatrix},$$

where

$$\mathcal{E} = \frac{ikL}{2}\frac{1}{N}\sum_{n=1}^{N} \varepsilon_n, \quad L = Nd.$$

In a sufficiently long stack, $\mathcal{E} \approx ikL\bar{\epsilon}/2$, and transmittance $T = |\mathcal{T}_{11}|^{-2}$ is given by

$$T = \frac{1}{1 + \left(kL\bar{\varepsilon}(f)/2\right)^2}.$$

Thus, at frequency f_{mp} transmittance of the sample is not an exponentially decreasing function of length L (as is typical for 1D Anderson localization). It decreases much more slowly, namely, according to the power law $T \propto L^{-2}$. The explanation of such a decrease is that at a μ-zero point ($f = f_{mp}$) the refractive index ν_n vanishes together with the phase shift $\beta_n = kd\nu_n \cos\theta_n$ across the layer, thereby destroying the interference, which is the main cause of localization. Another explanation is that the effective wavelength inside the stack tends to infinity when $\mu \to 0$ and exceeds the stack length. Obviously, such a wave is insensitive to disorder and therefore cannot be localized.

In the limit, as frequency approaches the μ-zero frequency from above (i.e., $f \to f_{mp}^{+}$), the medium is single negative, and $\varepsilon\mu < 0$. For frequencies f not too close to f_{mp} radiation decays exponentially inside the sample due to tunneling, and in the absence of dissipation the decay rate is

$$l_{\text{att}} = \frac{1}{kd\sqrt{-\langle\mu\rangle\langle\varepsilon\rangle}}. \tag{3.35}$$

Thus, as we approach μ-zero frequency from the right, the formally-calculated localization length diverges as $l \propto (f - f_{mp})^{-1/2}$, i.e., much more slowly than that for the left-hand limit, for which $l \propto (f_{mp} - f)^{-1}$. Transport properties in vicinity of ε-zero frequency f_{ep} can be considered in a similar manner. Waves are also delocalized in the more exotic case when both dielectric permittivity and magnetic permeability vanish simultaneously. The vanishing of both μ and ε simultaneously can happen at Dirac points in photonic crystals.[81]

The use of off-axis incidence from free space for frequencies for which μ or ε are zero is not an appropriate mechanism for probing the suppression of localization. Under such circumstances tunneling occurs, and localization properties of the stack are not "accessible"' from free space. Nevertheless, the suppression of localization can be revealed using an internal probe, e.g., by placing a plane wave source inside the stack, or by studying the corresponding Lyapunov exponent. Both approaches show total suppression of localization at the frequencies at which dielectric permittivity or magnetic permeability vanish.

Under such circumstances each layer that is embedded in a homogeneous medium with material constants given by average values of dielectric permittivity and magnetic permeability, is completely transparent, thus manifesting complete suppression of localization. However, the "delocalized" states at zero-μ or zero-ε frequencies are in a sense trivial, corresponding to fields that do not change along the direction normal to the layers.

Another example of suppression of localization is related to the Brewster anomaly. As we saw above, in a non-dispersive mixed stack with only thickness disorder the delocalization of p-polarized radiation occurs at the Brewster angle of incidence. At this angle the Fresnel coefficient ρ Eq. (3.24) and, therefore, the reflection coefficient Eq. (3.2) as well, vanish for any frequency, thus making each layer completely transparent.

In the presence of dispersion, the same condition $\rho = 0$ leads to more intriguing results. In this instance, frequency-dependent angles, at which a layer becomes transparent, exist not only for p-polarization, but also for an s-polarized wave. This means that the Brewster anomaly occurs for both polarizations, with the corresponding angles, θ_p and θ_s, being determined by the conditions

$$\tan^2\theta_p = \frac{\varepsilon(\varepsilon\overline{\mu} - \overline{\varepsilon}\mu)}{\overline{\varepsilon}(\varepsilon\mu - \overline{\varepsilon}\overline{\mu})}, \tag{3.36}$$

$$\tan^2\theta_s = \frac{\mu(\overline{\varepsilon}\mu - \varepsilon\overline{\mu})}{\overline{\mu}(\varepsilon\mu - \overline{\mu}\overline{\varepsilon})}. \tag{3.37}$$

The right-hand sides of these equations always have opposite signs. Therefore, from the Brewster conditions (3.36) and (3.37) one can find either the Brewster angle and the corresponding polarization for a given frequency, or the Brewster frequency and the corresponding polarization for a given angle of incidence.

While for a stack with only thickness disorder the condition $\rho = 0$ can be satisfied for all layers simultaneously, when ε and/or μ fluctuate the conditions (3.36) or (3.37) define the frequency-dependent Brewster angles, which are slightly different for different layers. These angles occupy an interval, within which the stack is not completely transparent, but has anomalously large transmission lengths.[27,45]

When only the dielectric permittivity is disordered and $\mu = \overline{\mu}$, the Brewster conditions (3.36) and (3.37) simplify to

$$\tan^2\theta_s = -1, \tag{3.38}$$

$$\tan^2\theta_p = \frac{\varepsilon}{\overline{\varepsilon}} \approx 1. \tag{3.39}$$

In this case, the Brewster condition is satisfied only for p-polarization. For weak disorder, the Brewster angle of incidence from the effective medium is $\theta_p \approx \pi/4$. For a given frequency f the angle of incidence from free space θ_0 should be found from Snell's law Eq. (3.33), and for a given θ_0 the Brewster frequency f_p follows from

$$\sqrt{\overline{\varepsilon}(f_p)\overline{\mu}(f_p)} = \frac{\sin\theta_0}{\sin\theta_p} = \sqrt{2}\sin\theta_0. \tag{3.40}$$

Note that this equation may be satisfied at multiple frequencies depending on the form of dispersion.

The case of only magnetic permeability disorder, $\varepsilon = \overline{\varepsilon}$, is described by similar equations, which are obtained by switching s and p in Eqs. (3.38)–(3.40).

For disorder in both permeability and permittivity the existence of a Brewster anomaly angle depends, in accordance with Eqs. (3.36) and (3.37), on the sign of the quantity $\xi = (\overline{\varepsilon}\mu - \varepsilon\overline{\mu})/(\varepsilon\mu - \overline{\varepsilon}\overline{\mu})$. If $\xi > 0$, the Brewster angle exists for s-polarization, while if $\xi < 0$, it exists for p-polarization. When $\xi = 0$ the layer and the medium in which it is embedded are impedance matched, and thus the layer is completely transparent.

The features of transmission length mentioned above are completely confirmed by numerical calculations. Consider

first the case of normal incidence on a stack of $N = 10^7$ layers, in which we randomize only the dielectric permittivity ($Q_m = 0$) with $Q_e = 0.5 \cdot 10^{-2}$. In Fig. 13 the transmission length l_T as a function of frequency f is displayed. The upper curves present the lossless case, while the lower curves show the effects of absorption (see Ref. 46 for details).

The red solid curves and the blue dashed curves display results from numerical simulations and the WSA theoretical prediction, respectively. The top curves represent genuine localization length for all frequencies except those in vicinity of $f \approx f_{mp} = 10.95$ GHz, where transmission length increases dramatically.

In the absence of absorption, for frequencies $f > 10.95$ GHz the metamaterial transforms from double negative to single negative (see inset in Fig. 13). The refractive index of the metamaterial layer changes from being real to being pure imaginary, the random stack becomes opaque, and transmission length decreases substantially. Such a drastic change in transmission length (by a factor of 10^5) may be exploitable in a frequency controlled optical switch. Across the frequency interval $10.4\ \text{GHz} < f < 11.0\ \text{GHz}$ theoretical results are in excellent agreement with those of direct simulation. Moreover, for all frequencies except those in the region $10.4\ \text{GHz} < f < 10.5\ \text{GHz}$ the single scattering approximation describes the l_T behavior very well. Quite surprisingly, the asymptotic value equations (3.34) and (3.35) are in excellent agreement with numerical results even over the frequency range $10.9\ \text{GHz} < f < 11.0\ \text{GHz}$, including the near vicinity of frequency $f_{mp} = 10.95$ GHz, at which μ vanishes.

Absorption substantially influences the transmission length (the lower curve in Fig. 13)[46] and smoothes the nonmonotonic behavior of transmission length for $f < 10.5$ GHz. The small dip at $f \approx 10.45$ GHz correlates with the corresponding dip in transmission length in the absence of absorption. The most prominent effect of absorption occurs for frequencies just below the μ-zero frequency $f_{mp} = 10.95$ GHz. While in the absence of absorption, the stack is nearly transparent in this region. Turning on absorption reduces the transmission length by a factor of 10^2–10^3 for $f > 10.7$ GHz. In contrast, for frequencies $f > 10.95$ GHz transmission lengths in the presence and absence of absorption are nearly identical, because here the stack is already opaque, and its transmittance is not much affected by a small amount of additional absorption.

The case where both disorders of dielectric permittivity and magnetic permeability are present is qualitatively similar to that of the single disorder case considered above.

In the case of oblique incidence the polarization effects become important. In Fig. 14 the transmission length frequency spectrum is displayed for the same metamaterial H-stack with only dielectric permittivity disorder for the angle of incidence $\theta_0 = 30°$. Here, for frequencies $f < 10.55$ GHz the transmission length is largely independent of polarization. Moreover, it does not differ from that for normal incidence (compare with the top curve in Fig. 13). This is due to high values of refractive indices at these frequencies ($|\nu_n| > 4$), resulting in almost zero refraction angles Eq. (3.33) for angles of incidence that are not too large.

The transmission length manifests a sharp maximum at an angle close to the Brewster angle, as commented upon in Refs. 27 and 45. This is indeed apparent in Fig. 14 for

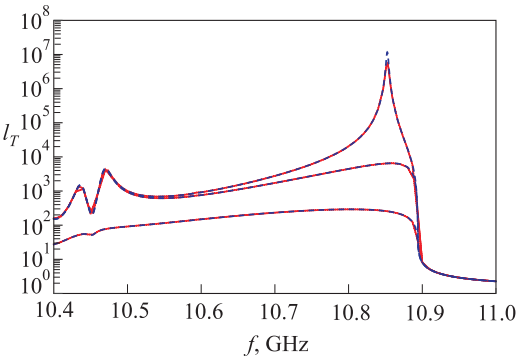

FIG. 14. (Ref. 46) Transmission length l_T vs. frequency f for $\theta_0 = 30°$ for a metamaterial stack: without absorption, p-polarization (top curves), s-polarization (middle curves); in the presence of absorption (bottom curves).

frequency $f \approx 10.85$ GHz. Because only ε fluctuates, the Brewster condition is satisfied only for p-polarization Eq. (3.38) at a single frequency $f_p \approx 10.852$ GHz. The introduction of additional permeability disorder (not shown) reduces the maximum value of localization length by two orders of magnitude.

Comparison of Figs. 13 and 14 shows that the frequency of the maximal suppression of localization decreases as the angle of incidence increases. At normal incidence it coincides with the μ-zero frequency f_{mp}, while for oblique incidence at $\theta_0 = 30°$ it coincides with the Brewster frequency f_p for p-polarization.

Absorption strongly diminishes the transmission providing the main contribution to the transmission length, while permittivity disorder has little influence on the transmission length. Therefore, in this case the results for both polarizations are practically indistinguishable.

The transmission properties of a stack with only magnetic permeability disorder at oblique incidence are similar to those for the case of only dielectric permittivity disorder. The key difference is that there is a Brewster anomaly for s-polarization, while for p-polarization it is absent.

We also consider the dependence of transmission length on the angle of incidence at a fixed frequency. The results for both polarizations are displayed in Fig. 15. Here we have plotted the transmission length of the stack with only dielectric permittivity disorder with $Q_e = 0.5 \cdot 10^{-2}$ at frequency

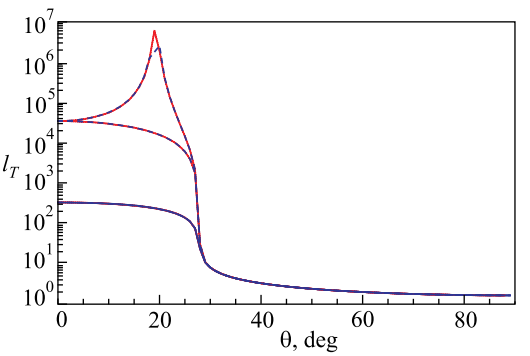

FIG. 15. (Ref. 46) Transmission length l_T vs. angle of incidence for a homogenous metamaterial stack at $f = 10.7$ GHz with permittivity disorder: in the absence of absorption (upper curve) and for p-polarization; middle curve is for s-polarization; and in the presence of absorption and for both polarizations (lower curves).

$f = 10.90$ GHz. The upper and middle curves in this figure correspond to the results for p- and s-polarized waves, respectively, in the lossless case. For s-polarized light, the transmission length decreases monotonically with increasing angle of incidence, while for a p-polarized wave it increases with increasing angle of incidence. Such behavior reflects the existence of a Brewster angle for p-polarization at the Brewster angle $\theta_0 = 20°$. The red solid curve shows the results of simulations, while the blue dashed line is the analytical prediction.

As in the previous cases, in the presence of absorption, the results for both polarizations are almost identical (the lower curves in Fig. 15). For angles $\theta_0 < 30°$, the transmission length is dominated by absorption, while for angles $\theta_0 > 30°$ tunneling is the dominant mechanism. The results for permeability disorder are very similar to those for permittivity disorder.

Transmission length manifests exactly the same behavior for normal H-stacks as it does for H-stacks comprised of metamaterial layers.

3.7. Anomalous suppression of localization

In this section we consider the stacks with only refractive index disorder (RID), i.e., the stacks with $\delta_d = \delta_\mu = 0$. In this limit, there is nothing special for H-stacks. Their transmission length demonstrates qualitatively and quantitatively the same behavior as was observed in the presence of both refractive index and thickness disorder. Corresponding formulae for the transmission, localization, and ballistic lengths can be obtained from the general case by taking the limit as $Q_d \to 0$.

In the case of M-stacks, however, the situation changes markedly. Here, suppression of localization in the long-wave region becomes anomalously large enhancing transmission length on some orders of magnitude and even changing its functional dependence on the wavelength.[43] Instead of the universal $\propto \lambda^2$ dependence, the long-wave asymptotic value of both the localization length l and the reciprocal of the Lyapunov exponent l_ξ follows a power law $\propto \lambda^m$ with a much larger exponent m.

Let us start with some numerical results demonstrating such anomalous growth of the long-wave localization lengths l, l_ξ of the minimally disordered M-stack with only RID. In Fig. 16 the localization length l_ξ for an M-stack with $Q = 0.25$ is plotted. The solid line in Fig. 16 corresponds to l_ξ for propagation in an M-stack and a single realization of $N = 10^9$ layers, while the dashed line is for the corresponding H-stack with the same parameters. Within the localization region $l_\xi(\lambda) < 10^8$, the M-stack reciprocal of the Lyapunov exponent grows in the long-wave region essentially faster than that of an H-stack. While the H-stack is described by the standard exponent $m = 2$, its value for an M-stack was estimated as $m = 6$, and the phenomenon itself was named as λ^6 anomaly. The observed anomalous suppression of localization was attributed to a lack of phase accumulation over the sample, due to the cancelation of the phase that occurs in alternating L- and R-layers.[43]

Anomalous enlightening is also manifested in the case of oblique incidence. The next Fig. 17 displays transmission length spectra for an M-stack with only refractive index

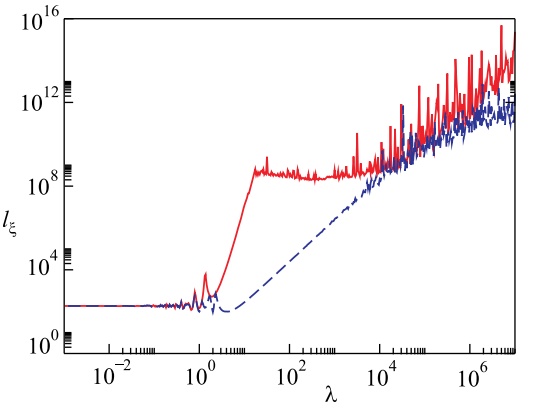

FIG. 16. (Ref. 43) Characteristic length l_ξ vs. wavelength λ for $Q = 0.25$ and $N = 10^9$ layers; the solid line is for the M-stack, while the dashed line is for the corresponding (normal) H-stack.

disorder for an angle of incidence $\theta = 30°$. There is a striking difference between the two polarizations: in the case of p-polarized light, there is strong localization at long wavelengths ($\lambda \le 10^2$), with the localization length showing $\propto \lambda^2$ dependence. In contrast, the localization length for s-polarized light is much larger and is estimated to be $\approx \lambda^6$, as the dependence occurring for normal incidence. Note that for s-polarization, anomalous enlightening manifests itself only in localization regions in Fig. 17, which are bounded from above by the wavelength limits $\lambda \le 5$, 9, and 12 for stacks of length $N = 10^5$, 10^7, and $8 \cdot 10^8$, respectively.

This asymmetry between the polarizations suggests that the suppression of localization is due not only to the suppression of the phase accumulation, but also to the vector nature of the electromagnetic wave. Because of the symmetry of Maxwell's equations between the electric and magnetic fields, it is to be expected that for a model in which there is disorder in magnetic permeability (with $\varepsilon = \pm 1$) the situation will be inverted with anomalous enlightening for p-polarized waves and with s-polarization showing strong localization.

The results of calculations[44] provided for much longer stacks (up to $N = 10^{12}$) qualitatively completely coincided with the previous ones. However, more detailed studies gave results slightly different quantitatively. The generation of a least squares fitting $l_T = A\lambda^m$ to the transmission length data led to surprising conclusions. The best fit was obtained using $m \approx 6.25$ for $N = 10^7$, $m \approx 7.38$ for $N = 10^9$, and even

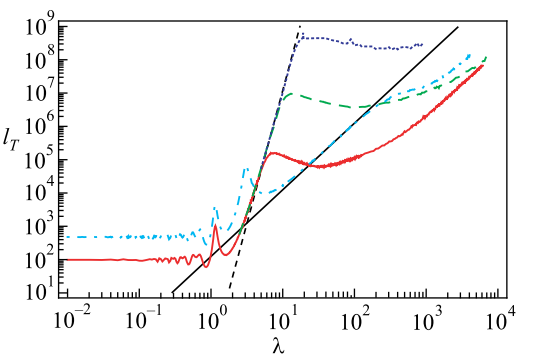

FIG. 17. (Ref. 45) Transmission length l_T vs. λ for an M-stack with $Q_\nu = 0.25$, $Q_d = 0$, and $\theta = 30°$ for p-polarized light (cyan dashed dotted curve, $N = 10^6$) and s-polarized light (red solid curve, $N = 10^5$; green dashed curve, $N = 10^7$; blue dotted curve, $N = 8 \cdot 10^8$).

$m \approx 8.78$, for $N = 10^{12}$. This shows that the question about a genuine value of exponent m still remains open.

Consider now the long-wave behavior of the localization length in the presence of dispersion. In Fig. 18(a) the transmission length spectrum is plotted in the case of normal incidence for a small permittivity disorder $Q_e = 0.5 \cdot 10^{-2}$. One can immediately observe significant (up to four orders of magnitude) suppression of localization in the frequency region $10.50\ \text{GHz} < f < 10.68\ \text{GHz}$. However, this suppression seems to have nothing in common with the observed above anomalous enlightening. Indeed, in this case localization length grows with increasing frequency, while in the previous studies[43–45] similar growth was observed with increasing incident wavelength. This is demonstrated in Fig. 8(b), where the same transmission length spectrum is plotted as a function of free space wavelength. Thus, the localization length decreases by four orders of magnitude, manifesting as an enhancement, rather than suppression, of localization with increasing wavelength.

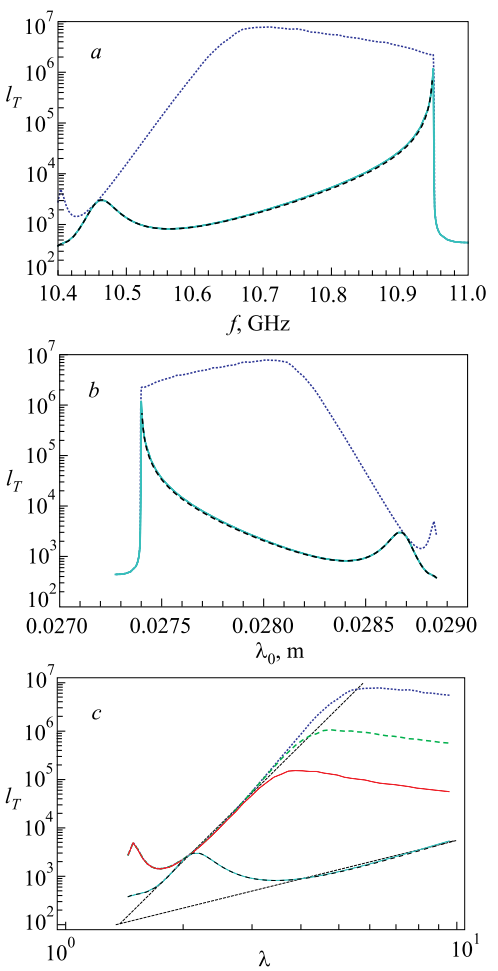

FIG. 18. (Ref. 46) (a) Transmission length l_T vs. frequency f for a mixed stack with $N = 10^7$ layers (top dotted blue curve), and only dielectric permittivity disorder. The bottom curves on all the panels (a, b, c) are for a stack with $N = 10^7$ layers with both permittivity and permeability disorder (the cyan, solid curve displays simulation results, while the dashed, black curve is for the analytical prediction); (b) is the same as (a), but plotted as a function of free space wavelength λ_0, while on panel (c) we plot transmission length as a function of the averaged wavelength inside the stack normalized to the thickness of the layer, for $N = 10^7$ layers (blue dotted top curve), $N = 10^6$ layers (dashed green curve) and for $N = 10^5$ layers (red solid curve), respectively.

Although at first look these findings are in sharp contrast with the previous ones, they are correct and physically meaningful. In the model studied earlier[43–45] the wavelength of incident radiation largely coincided with the wavelength inside each layer. In dispersive medium considered here these two wavelengths differ substantially. Accordingly, in Fig. 18(c) we plot transmission length as a function of wavelength within the stack and obtain results that are very similar to those in Refs. 43–45. To emphasize this similarity we have plotted the transmission length spectrum for three different stack lengths: $N = 10^5$, 10^6, 10^7. It is easily seen that the suppression of localization in the dispersive media is qualitatively and quantitatively similar to that predicted in Ref. 43. The corresponding exponent m of anomalous enlightening estimated with the help of these results is $m \approx 8.2$.

Enhanced suppression of localization exists in the strictly periodic alternative M-stacks with a constant layer thickness and only refractive index disorder. In other words, in mixed stacks having constant layer thickness the dielectric permittivity disorder alone is not sufficiently strong to localize low-frequency radiation in a standard way. There are many ways to violate these conditions. It is possible to add thickness fluctuations[43,44] or magnetic permeability fluctuations,[46] or to introduce a small difference between two constant thicknesses of R- and L-layers, or not to change any parameter but rearrange randomly the same numbers $N/2$ of R- and L-layers.[44] Each such violation immediately destroys anomalous suppression of localization and restores the standard long-wave asymptotic value $l \propto \lambda^2$.

Analytical results obtained above in Sec. 3 survive in the $\delta_d \to 0$ limit and predict $l \propto \lambda^2$ as the asymptotic value. However, a more detailed investigation shows that WA in its form (Eqs. (2.18) and (2.19)) fails in this limit.[44]

As was mentioned above, localization length l_ξ exhibits qualitatively the same behavior as transmission length l_T. At the same time, its calculation is simpler than that of l_T. The Lyapunov exponent in minimally disordered M-stacks was calculated in Ref. 52 using some version of the method described in Refs. 2, 41, 42, and 58 and at the end of Sec. 2.2. The remaining part of this Subsection contains slightly modified details and results of this calculation.[52]

Consider an electromagnetic wave of frequency $\omega = ck$ in an infinite array comprised of two types of lossless alternative α and β layers of equal dimensionless thickness $\Delta_j = 1$ with random dielectric permittivities. Enumerate the layers so that the jth layer occupies the interval $j - 1 \le z < j$ and choose all odd layers of α type and all even of β type. For an alternative array, it is natural to choose an elementary cell composed of two adjacent layers as the main basic element of the array.[43,52] The nth cell occupies interval $2n - 2 \le z < 2n$ and consists of $(2n - 1)$-th and $2n$ layers of type α and β, correspondingly. Each layer is characterized by its type $\alpha(\beta)$, magnetic permeability $\mu_\alpha = 1$ ($\mu_\beta = \pm 1$), refractive index $\nu_\alpha(n)$ ($\nu_\beta(n)$), impedance $Z_\alpha(n) = 1/\nu_\alpha(n)$ ($Z_\beta(n) = \pm 1/\nu_\beta(n)$), and wave number $k_{\alpha,\beta} = k\nu_{\alpha,\beta}$ of the wave.

Within such a model, two systems are considered: the H-array, when both α and β layers are made of righthanded materials, and the M-array, where α layers are of righthanded material, while β layers are of left-handed material. We emphasize that on the contrary to the H-stack notion,

where all the layers have the same statistical properties, an H-array is composed of two different materials with different statistical properties for odd and even layers. Disorder is incorporated into the model via dielectric permittivities $\varepsilon_{\alpha,\beta}$ only, so that refractive index ν is a sole fluctuation parameter, and the upper index in its fluctuations $\delta^{(\nu)}_{\alpha,\beta}(n)$ can be omitted

$$\nu_\alpha(n) = 1 + \delta_\alpha(n), \quad \nu_\beta(n) = \pm[1 + \delta_\beta(n)]. \tag{3.41}$$

Refractive index fluctuations $\delta_{\alpha,\beta}(n)$ are assumed to be delta-correlated with zero mean value $\langle\delta_{\alpha,\beta}(n)\rangle = 0$ and variance σ^2,

$$\langle\delta_\alpha(n)\delta_\beta(n')\rangle = \sigma^2\delta_{\alpha\beta}\delta_{nn'}, \tag{3.42}$$

where angular brackets denote the ensemble average.

To calculate the Lyapunov exponent of an electromagnetic wave of the frequency ω, consider a two-component vector

$$\mathbf{S}_n = \begin{pmatrix} Q_n \\ P_n \end{pmatrix}$$

with components

$$Q_n = E(2n-2), \quad P_n = \frac{c}{\omega}E'(2n-2) \tag{3.43}$$

proportional to the field and its derivative at the left edge of the nth cell. These components are real. Therefore they automatically correspond to the currentless field and can be parametrized as

$$\mathbf{S}_n = \mathrm{e}^{\xi_n}\begin{pmatrix} \cos\theta_n \\ \sin\theta_n \end{pmatrix} \tag{3.44}$$

(compare with Eq. (2.9)). Note that this is the currentless state on the basis of standing waves, while in Sec. 2.2 the basis of running waves was used.

Using Maxwell equations and appropriate boundary conditions at the interfaces of the layers, one obtains the dynamic equation

$$\mathbf{S}_{n+1} = \hat{T}\mathbf{S}_n. \tag{3.45}$$

Here, $\hat{T}_n$ is the unimodular matrix with elements

$$\begin{aligned} T_{11} &= \cos\varphi_\alpha\cos\varphi_\beta - Z_\alpha^{-1}Z_\beta\sin\varphi_\alpha\sin\varphi_\beta, \\ T_{12} &= Z_\alpha\sin\varphi_\alpha\cos\varphi_\beta + Z_\beta\cos\varphi_\alpha\sin\varphi_\beta, \\ T_{21} &= -Z_\alpha^{-1}\sin\varphi_\alpha\cos\varphi_\beta - Z_\beta^{-1}\cos\varphi_\alpha\sin\varphi_\beta, \\ T_{22} &= \cos\varphi_\alpha\cos\varphi_\beta - Z_\alpha Z_\beta^{-1}\sin\varphi_\alpha\sin\varphi_\beta. \end{aligned} \tag{3.46}$$

They depend on the cell number n, due to randomized refractive indices Eq. (3.41) entering both the impedances $Z_{\alpha,\beta}(n)$ and phase shifts $\varphi_{\alpha,\beta}(n)$,

$$\begin{aligned} \varphi_\alpha(n) &= \frac{1}{2}k_\alpha(n) = \varphi[1 + \delta^\nu_\alpha(n)], \\ \varphi_\beta(n) &= \frac{1}{2}k_\beta(n) = \pm\varphi[1 + \delta^\nu_\beta(n)], \end{aligned} \tag{3.47}$$

with $\varphi = k/2$.

In ξ_n, θ_n terms, dynamic equations read

$$\xi_{n+1} - \xi_n = \Phi(\theta_n), \tag{3.48}$$

$$\tan\theta_{n+1} = \left[\frac{T_{21} + T_{22}\tan\theta_n}{T_{11} + T_{12}\tan\theta_n}\right], \tag{3.49}$$

where now

$$\Phi(\theta) = \frac{1}{2}\ln\frac{(T_{11} + T_{12}\tan\theta)^2 + (T_{21} + T_{22}\tan\theta)^2}{1 + \tan^2\theta}. \tag{3.50}$$

Going to the limit $n \to \infty$ and using Eqs. (2.24) and (2.25) for localization length $l_\xi = \gamma^{-1}$ we obtain

$$\frac{1}{l_\xi} = -\langle\Phi(\theta)\rangle_{\mathrm{st}}, \tag{3.51}$$

where averaging in the r.h.s. is taken over the stationary distribution of phase θ.

In the case of weak disorder,

$$\sigma^2 \ll 1 \quad \text{and} \quad (\sigma\varphi)^2 \ll 1,$$

this distribution $\rho(\theta)$ can be explicitly found within the framework of a proper perturbation theory. Expanding the exact θ-map Eq. (3.48) up to the second order in perturbation[59] and taking into account the uncorrelated nature of the disorder (see Eq. (3.42)), one obtains

$$\begin{aligned} \theta_{n+1} - \theta_n = &-\phi - \delta_\alpha(n)U(\theta_n) \\ &\mp \delta_\beta(n)U(\theta_n - \phi/2) - \sigma^2 W(\theta_n), \end{aligned} \tag{3.52}$$

where

$$\begin{aligned} U(\theta) &= \varphi + \sin\varphi\cos(2\theta - \varphi) \\ W(\theta) &= \varphi[\cos(2\theta - 2\varphi) \pm \cos(2\theta - 2\phi)] + \sin\varphi \\ &\quad \times [\sin\theta\sin(\theta - \varphi) \pm \sin(\theta - \phi/2)\sin(\theta - \varphi - \phi/2)] \\ &\quad + \sin^2\varphi\sin(4\theta - 2\varphi - \phi)\cos\phi, \end{aligned} \tag{3.53}$$

"plus" stands for the H-array, and "minus" refers to the M-array, and

$$\phi = \begin{cases} k, & \text{H-array} \\ 0, & \text{M-array} \end{cases} \tag{3.54}$$

is the unperturbed Bloch phase shift ϕ over a unit (α,β) cell.

Now, one should write down the Fokker–Plank equation related to the dynamic equations (3.52)

$$\begin{aligned} &\frac{d^2}{d\theta^2}[U^2(\theta) + U^2(\theta - \phi/2)]\rho(\theta) \\ &\quad + 2\frac{d}{d\theta}\left[\frac{\phi}{\sigma^2} + W(\theta)\right]\rho(\theta) = 0, \end{aligned} \tag{3.55}$$

find it normalized in the π-periodic solution, and calculate the average in the r.h.s. of Eq. (3.51).

For an H-array, this program can be easily realized. Indeed, in such a structure the Bloch phase Eq. (3.54) is

nonzero, and for weak disorder the term in Eq. (3.55) containing ϕ/σ^2 prevails over the others. Therefore, phase distribution within the main order of perturbation theory is uniform

$$\rho(\theta) = 1/\pi. \tag{3.56}$$

Substituting this probability density into the definition (3.51) and using Eqs. (3.52) and (3.53) one gets

$$1/l_\xi \equiv \gamma = \sigma^2 \sin^2\varphi.$$

In the long-wave limit, where the phase shift φ is small, this result yields asymptotic values

$$l_\xi \approx \frac{\lambda^2}{\pi^2\sigma^2}, \quad \lambda \gg 1.$$

This result gives rise to standard λ-dependence, $l_\xi \propto \lambda^2$ when $\lambda \to \infty$. In the case of uniform distribution of δ over the interval $[-Q_\nu, Q_\nu]$ considered in Sec. 3, it exactly coincides with the long-wave asymptotic value Eq. (3.20) of localization length l.

A principally different situation emerges for the M-array. In this case the Bloch phase Eq. (3.54) is exactly zero. As a result, $W(\theta) = -U(\theta)U'(\theta)$ in Eq. (3.53), and Eq. (3.55) leads to a highly nonuniform phase distribution

$$\rho(\theta) = \frac{1}{\pi}\sqrt{\varphi^2 - \sin^2\varphi}/U(\theta). \tag{3.57}$$

Figure 19 displays perfect agreement between analytical expressions (3.56) and (3.57) and data obtained by the iteration of the exact map Eq. (3.45).

To calculate the Lyapunov exponent via Eq. (3.51) one needs to perform an averaging with the distribution $\rho(\theta)$ given by Eq. (3.57). Surprisingly, the use of Eqs. (3.51), (3.52), and (3.57) results in zero Lyapunov exponent[51] in the main (second order) approximation $\sim\sigma^2$. Therefore, the Lyapunov exponent is determined by the next orders of perturbation theory.

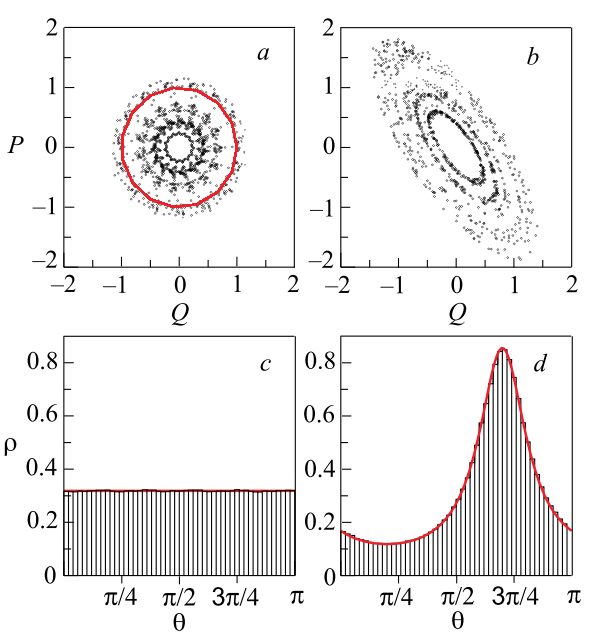

FIG. 19. (Ref. 52) (a) The phase space trajectory generated using Eq. ((3.45)) for an H-array with $N = 10^4$, $\varphi = \pi/15$, for zero disorder (solid circle), and for $\sigma^2 = 0.003$ (scattered points). (b) One trajectory for an M-array with $N = 10^6$, $\varphi = 2\pi/5$, $\sigma^2 = 0.003$. (c) $\rho(\theta)$ from Eq. ((3.45)) for an H-array (histogram), and Eq. ((3.56)) (horizontal line); (d) $\rho(\theta)$ from Eq. ((3.45)) for an M-array (histogram), and Eq. ((3.57)) (solid curve).

Unfortunately, direct evaluation of high order terms in $\rho(\theta)$ is rather cumbersome because of huge technical complexity.[51] The crucial step which enables authors of Ref. 52 to resolve the problem is the following. It is known that essential calculation difficulties are often related to non-proper selection of dynamic variables. To understand how these variables should be chosen, let us analyze the numerical data displayed in Fig. 19. The *b*-panel in this figure demonstrates that the trajectory (i.e., the sequence of points (Q_n, P_n)) has the form of a fluctuating ellipse specified by an angle with respect to the axes, and by fixed aspect ratio. This results in strongly nonuniform phase distribution (*d*-panel in Fig. 19). Therefore, one should introduce new variables $\tilde{Q}_n$, $\tilde{P}_n$ by rotating and rescaling the axes Q, P so that the trajectory transforms into a fluctuating circle. Then, one can expect that the distribution of a new phase Θ_n in the considered approximation will be uniform.

To follow this recipe, let us rotate the vector $\mathbf{S} \to \tilde{\mathbf{S}} = \hat{R}\mathbf{S}$ with the help of unimodular matrix

$$\hat{R} = \begin{Vmatrix} \sqrt{\eta}\cos\tau & \sqrt{\eta}\sin\tau \\ -\dfrac{\sin\tau}{\sqrt{\eta}} & \dfrac{\cos\tau}{\sqrt{\eta}} \end{Vmatrix},$$

where the angle τ describes rotation of the axes in **S**-space, with further rescaling of the axes due to free parameter η. In new coordinates the expressions (3.45) and (3.51) conserve their forms, however, with the rotated transfer matrix

$$\tilde{\hat{T}} = \hat{R}\hat{T}\hat{R}^{-1}, \quad \tilde{\mathbf{S}}_n = \mathrm{e}^{\Xi_n}\begin{pmatrix}\cos\Theta_n \\ \sin\Theta_n\end{pmatrix}. \tag{3.58}$$

Now the distribution $\rho(\Theta)$ for the new phase Θ can be found starting from the quadratic expansion of Eq. (3.48) with new coefficients Eq. (3.58) and $\phi = 0$,

$$\Theta_{n+1} - \Theta_n = [\eta_\alpha(n) - \eta_\beta(n)]V(\Theta_n) + \sigma^2 V(\Theta_n)V'(\Theta_n). \tag{3.59}$$

Here, the function $V(\Theta)$ is

$$\begin{aligned} V(\Theta) = {} & \sin\varphi\sin(2\tau-\varphi)\sin 2\Theta \\ & + \frac{\eta}{2}[\varphi - \sin\varphi\cos(2\tau-\varphi)][\cos 2\Theta - 1] \\ & - \frac{1}{2\eta}[\varphi + \sin\varphi\cos(2\tau-\varphi)][\cos 2\Theta + 1]. \end{aligned} \tag{3.60}$$

The stationary Fokker–Plank equation corresponding to the Θ-map Eq. (3.59) reads

$$\frac{d}{d\Theta}\left[V^2(\Theta)\frac{d}{d\Theta}\rho(\Theta) + V(\Theta)V'(\Theta)\rho(\Theta)\right] = 0.$$

From this equation one gets that the phase distribution is uniform, $\rho(\Theta) = 1/\pi$, and the trajectory is, indeed, a fluctuating circle, provided that

$$\frac{d}{d\Theta}V(\Theta)V'(\Theta)=0. \tag{3.61}$$

With the use of Eqs. (3.60) and (3.61) we can now obtain the desired expressions for the angle τ, parameter η, and function $V(\Theta)$ (which is actually no longer Θ-dependent),

$$\tau=\frac{\varphi}{2},\quad \eta^2=\frac{\varphi+\sin\varphi}{\varphi-\sin\varphi},$$
$$V(\Theta)=\sqrt{\varphi^2-\sin^2\varphi}. \tag{3.62}$$

The results presented in Fig. 20 confirm success of the chosen approach: in new variables the trajectory is a fluctuating circle, and phase distribution is uniform.

The Lyapunov exponent γ can now be obtained via Eq. (3.51) with the change $\theta_n \to \Theta_n$. Taking into account that γ vanishes within the quadratic approximation in disorder, we expand the Θ-map of the form Eq. (3.48) with the coefficients Eq. (3.58) up to the fourth order in perturbation. By substituting the resulting expression into Eq. (3.51) and expanding the logarithm within the same approximation, after averaging over Θ_n with uniform distribution, we arrive at the final expression

$$\frac{1}{l_\xi}=\frac{\zeta\sigma^4}{4}\frac{[(2\varphi^2-\sin^2\varphi)\cos\varphi-\varphi\sin\varphi]^2}{\varphi^2-\sin^2\varphi}. \tag{3.63}$$

Here, the constant

$$\zeta=\frac{\langle\delta(n)^4\rangle-\langle\delta(n)^2\rangle^2}{\langle\delta^2\rangle^2}$$

is specified by the form of distribution of $\delta_{\alpha,\beta}(n)$. For Gaussian and flat distributions we have $\zeta=0$, $-6/5$, respectively.

Equation (3.63) determines the asymptotic values for large $\lambda \gg \max(\sigma,1)$,

$$\frac{1}{l_\xi}\equiv\gamma\approx\frac{2^4}{3^35^2}(\zeta+2)\sigma^4k^8,$$

which results in quite a surprising wavelength dependence of localization length, $l_\xi \propto \lambda^8$. Thus, the dependence $l_\xi \propto \lambda^6$, numerically found for large λ in Refs. 43 and 44 and confirmed later on should be regarded as the intermediate one, apparently emerging due to not sufficiently large lengths N, over which the averaging of γ is performed.

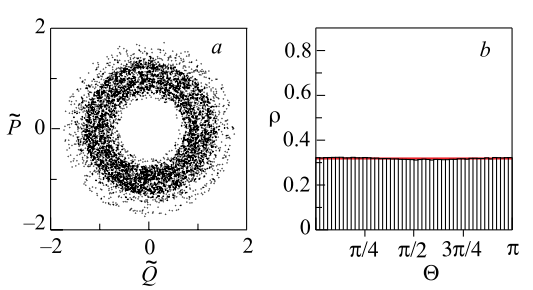

FIG. 20. (Ref. 52) (a) Phase space trajectory in new variables $(\tilde{Q},\tilde{P})$; (b) distribution $\rho(\Theta)$ generated by the transformed map with Eqs. ((3.58) and (3.62)), for $\gamma=0$, $\varphi=2\pi/5$, $\sigma^2=0.02$, and $N=10^7$.

4. Localization in complex media

4.1. Nonreciprocal transmission in magnetoactive optical structures

In this subsection we present the results of an analytical and numerical study of Anderson localization of light propagating through random magnetoactive layered structures. We demonstrate that an interplay between strong localization and magnetooptical effects produces a number of nonreciprocity features in the transmission characteristics.

Magnetooptical effects and nonreciprocity are widely exploited in modern optics and applied physics.[22,82] In particular, magnetoactive periodic structures are currently attracting growing attention.[83,84] The main phenomena of interest are the enhanced Faraday effect on resonances[85] and one-way propagation (nonreciprocal transmission)[86–89] employed for the concept of optical insulators. The resonant Faraday Effect has also been shown in connection with the localization of light in random layered structures.[35]

Here, we examine the transmission properties of one-dimensional random layered structures with magneto-optical materials. We employ short-wavelength approximation, where the localization is strong, and consider both Faraday and Voigt geometries. In the Faraday geometry, magnetooptical correction to the localization length l results in a significant broadband nonreciprocity and polarization selectivity in the typical, exponentially small transmission. In the

Voigt geometry, averaging over random phases suppresses the magnetooptical effect, in contrast to the case of periodic structures, where it can be quite pronounced.[86,88] At the same time, in both geometries we reveal nonreciprocal frequency shifts of narrow transmission resonances, corresponding to the excited localized states inside the structure.[9,78,90,91] This offers efficient unidirectional propagation at the given resonant frequency.

Consider light transmission through a long stack composed of magnetooptical materials in the short wavelength approximation. In the localized regime, we can neglect in Eq. (2.21) the external interface transfer matrices $\hat{F}^{0\alpha}$, $\hat{F}^{\beta 0}$ just replacing the exact matrix $\hat{T}$ by the truncated matrix $\hat{T}'$

$$\hat{T}'=\hat{F}_N\hat{S}_N\hat{F}_{N-1}\hat{S}_{N-1}\hat{F}_{N-2}\ldots\hat{F}_2\hat{S}_2\hat{F}_1\hat{S}_1. \tag{4.1}$$

Then, if the wavelength within the kth layer is much shorter than the variance of the layer thickness,[56] then the phases φ_k modulo 2π in the propagation matrices $\hat{S}_j$ Eq. (2.20) are independent and nearly uniformly distributed in the range $(0, 2\pi)$. In this approximation, transmittance corresponding to the transfer matrix Eq. (4.1) after averaging over all the phases φ_k is reduced to the product of transmittances of separate layers[49] and, furthermore, to the product of transmittances of the interfaces only[56]

$$\ln(\mathcal{T})\approx\sum_{j=1}^{2N}\ln\tau_j,\quad \tau_j=1/|(\hat{F}_j)_{11}|^2. \tag{4.2}$$

Substitution of Eq. (4.2) into Eq. (2.1) in the limit $N\to\infty$ yields a simple expression for the localization length

$$\frac{1}{l}=\frac{1}{2}\ln|(\hat{F}^{\alpha\beta})_{11}(\hat{F}^{\beta\alpha})_{11}| \tag{4.3}$$

in the short-wavelength approximation.

This result can be easily extended to any number of alternating layers. For instance, considering a random structure consisting of three types of alternating layers, "α," "β," and "γ," one has

$$\frac{1}{l}=\frac{1}{3}\ln|(\hat{F}^{\alpha\beta})_{11}(\hat{F}^{\beta\gamma})_{11}(\hat{F}^{\gamma\alpha})_{11}|.$$

Transmission through a one-dimensional lossless linear medium is always reciprocal if there is only one (but propagating in two directions) mode in the system. Indeed, while the forward transmission of the wave incident from the left of the medium is described by the 2×2 transfer matrix $\hat{T}$ with transmission coefficient T and transmittance $\mathcal{T}$, the backward transmission of the reciprocal wave incident from the right is characterized by the inverse transfer matrix $\hat{T}^{-1}$ with the same transmission coefficient and transmittance.[49,56]

If the system possesses two or more uncoupled modes labeled by index ς, the waves are marked by propagation direction υ and mode indices: $h^{\upsilon,\varsigma}$. Still, the forward and backward propagation of each mode ς through the system with incident waves of types $(+,\varsigma)$ and $(-,\varsigma)$ are described by the 2×2 transfer matrices $\hat{T}^{\varsigma}$ and $(\hat{T}^{\varsigma})^{-1}$ characterized by the same transmittance $\mathcal{T}^{\varsigma}$. However, the wave reciprocal to $(+,\varsigma)$ is determined by the time-reversal operation, which changes $\upsilon\rightarrow-\upsilon$ (because of the $\mathbf{k}\rightarrow-\mathbf{k}$ transformation), but can also affect ς.[82] In particular, if the time reversal operation changes the sign of the mode index ($\varsigma\rightarrow-\varsigma$), then the reciprocal wave will be $(-,-\varsigma)$ rather than the backward wave of the same mode $(-,\varsigma)$. Accordingly, transmittance of the mutually reciprocal waves through the system, $\mathcal{T}^{\varsigma}$ and $\mathcal{T}^{-\varsigma}$, can be different. This signals nonreciprocity in the system.

Nonreciprocity in the system under consideration originates from the difference between the modes ς and $-\varsigma$, and does not depend explicitly on the direction of incidence υ. Therefore, in practice, it is sufficient to compare only forward transmissions of the modes $\pm\varsigma$, described by the transfer matrices $\hat{T}^{\pm\varsigma}$ and transmittances $\mathcal{T}^{\pm\varsigma}$.

There are two main geometries typical for magnetooptical problems:[22] the Faraday geometry, where magnetization is collinear with the direction of propagation of the wave, and the Voigt (or Cotton–Mouton) geometry, where magnetization is orthogonal to the direction of propagation of the wave (see Fig. 21). Below we study the averaged transmission decrement and individual transmission resonances in both geometries and show that propagation of light in disordered magnetoactive layered media offers nonreciprocal transmission.

In the Faraday geometry both magnetization and the wave vector are directed across the layers, i.e., along the z axis (see Fig. 21). We assume that magnetic tensor is equal to one, and magnetooptical effects are described exclusively by the dielectric tensor, which in the Faraday geometry has the form[22]

$$\hat{\varepsilon}=\begin{Vmatrix}\varepsilon & -iQ & 0\\ iQ & \varepsilon & 0\\ 0 & 0 & \varepsilon\end{Vmatrix}.$$

The eigenmodes of the problem are circularly polarized waves of magnetic $\mathbf{H}$

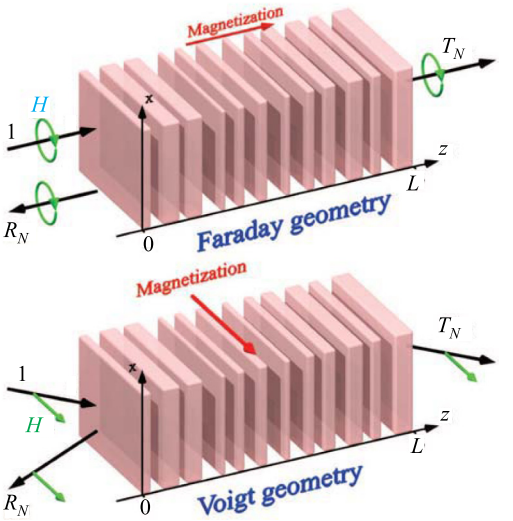

FIG. 21. (Ref. 34) A schematic picture of wave transmission and reflection from a random-layered structure consisting of two types of alternating layers "α" (here—a magnetoactive material) and "β" (here—air) with random widths. Magnetization of the medium, wave polarizations, and directions of propagation are shown for the Faraday and Voigt geometries.

$$\mathbf{H}^{\upsilon,\varsigma}=\frac{H^{\upsilon,\varsigma}}{\sqrt{2}}\begin{pmatrix}1\\ i\varsigma\\ 0\end{pmatrix}e^{i(\upsilon kz-\omega t)},\quad \upsilon,\varsigma=\pm 1, \tag{4.4}$$

and electric $\mathbf{E}$

$$\mathbf{E}^{\upsilon,\varsigma}=i\upsilon\varsigma\frac{k_0}{k}\mathbf{H}^{\upsilon,\varsigma} \tag{4.5}$$

fields. Here, $H^{\upsilon,\varsigma}$ ($E^{\upsilon,\varsigma}$) are the wave amplitudes, whereas k is the propagation constant affected by the magnetization parameter q, and, depending on ς:

$$k=nk_0\sqrt{1+\varsigma q},\quad n=\sqrt{\varepsilon},\quad k_0=\frac{\omega}{c},\quad q=\frac{Q}{\varepsilon}. \tag{4.6}$$

In the linear approximation in q, $k\simeq nk_0(1+\varsigma q/2)$.

Parameter ς is the mode index, which determines the direction of rotation of the wave field. In this manner, the product $\upsilon\sigma$ represents helicity

$$\chi=\upsilon\varsigma,$$

which distinguishes the right-handed ($\chi=+1$) and left handed ($\chi=-1$) circular polarizations defined with respect to the direction of propagation of the wave. Note that time reversal operation keeps helicity unchanged, whereas ς changes its sign.[82] Thus, the reciprocal wave is given by $\mathbf{H}^{-\upsilon,-\varsigma}$, precisely as described above.

The total field in a layer is the sum $\mathbf{H}^{+,\varsigma}+\mathbf{H}^{-,\varsigma}$ of eigenvectors Eq. (4.4) with amplitudes $H^{\pm,\varsigma}$. Consider wave transformation at the interface between the media "a" and "b." The helicity of the wave flips upon reflection and remains unchanged upon transmission. As a result, parameter ς remains unchanged, so that there is no coupling between the modes with $\varsigma=+1$ and $\varsigma=-1$ (see Fig. 21), and these modes can be studied independently. From now on, for the sake of simplicity, we omit $_{\varsigma}$ in superscripts and write explicitly only the values of direction parameter $\upsilon=\pm 1$.

Using the standard boundary conditions for the wave in electric and magnetic fields at the "α"–"β" interface, for normalized fields we have

$$\mathbf{h} = \frac{k_0}{k}\begin{pmatrix} H^+ \\ H^- \end{pmatrix}, \quad \mathbf{h}_\alpha = \hat{F}^{\alpha\beta}\,\mathbf{h}_\beta$$

with the normalized interface transfer matrix

$$\hat{F}^{\alpha\beta} = \frac{1}{2\sqrt{k_\alpha k_\beta}}\begin{Vmatrix} k_\beta + k_\alpha & k_\beta - k_\alpha \\ k_\beta - k_\alpha & k_\beta + k_\alpha \end{Vmatrix}, \tag{4.7}$$

where $k_{\alpha,\beta}$ are the wave numbers Eq. (4.6) in the corresponding media.

Calculating the localization decrement from Eq. (4.3) with Eqs. (4.6) and (4.7), in the linear approximation in q we obtain

$$\kappa = 2\ln\frac{k_\alpha + k_\beta}{2\sqrt{k_\alpha k_\beta}} \simeq \kappa^{(0)} + \kappa^{(1)}, \quad \kappa^{(0)} = \ln\frac{(n_\alpha + n_\beta)^2}{4n_\alpha n_\beta},$$
$$\kappa^{(1)} = \frac{\sigma}{2}(q_\alpha - q_\beta)\frac{n_\alpha - n_\beta}{n_\alpha + n_\beta}. \tag{4.8}$$

Thus, the localization decrement acquires the first-order magnetooptical correction $\kappa^{(1)}$ caused by the Faraday effect. This correction depends on ς, i.e., on the polarization helicity χ and the propagation direction υ through $\varsigma = \chi\upsilon$. For reciprocal waves with the same χ and opposite υ, $\kappa^{(1)}$ has opposite signs. This signals nonreciprocal localization in a Faraday random medium. In practice, the nonreciprocal difference in transmission decrements Eq. (4.8) can be observed by changing the sign of either propagation direction υ (with helicity being fixed), or polarization χ, or magnetization q.

Despite the fact that magnetooptical correction to the localization decrement is small in magnitude, $\kappa^{(1)} \ll \kappa^{(0)}$, it still might result in a significant difference in the typical transmission spectrum. This difference is described by an additional factor $\propto \exp[-2N\kappa^{(1)}]$ in transmittance, which is exponential with respect to the length of the structure. Hence, small correction Eq. (4.8) brings about significant broadband nonreciprocity or polarization selectivity in a typical small transmission when $N|\kappa^{(1)}| \geq 1$.

Figure 22 shows the dependence of localization decrement on the magnetization parameter $Q = \varepsilon q$ calculated numerically and compared to the analytical result Eq. (4.8). Numerical simulations were performed for the structure containing $\mathcal{N} = 2N = 90$ alternating layers of air ($\varepsilon = 1$, $Q = 0$) and bismuth iron garnet (BIG) with dielectric constant $\varepsilon = 6.25$ and magnetooptic parameter reaching $Q = 0.06$. The thicknesses of layers were randomly distributed in the range from 50 to 150 μm (i.e., $\overline{w} = 100\,\mu$m, $d = 50\,\mu$m), whereas the excitation wavelength was 632 nm. The averaging was performed over 10^5 realizations of the random sample. One can see excellent agreement between numerical simulations and analytical results showing linear splitting of the $\varsigma = 1$ and $\varsigma = -1$ localization decrements as a function of the magnetooptic parameter.

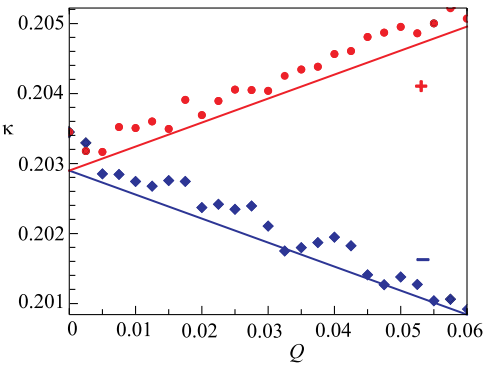

FIG. 22. (Ref. 34) Localization decrement κ vs. magnetooptical parameter Q for opposite modes propagating through a two-component random structure in the Faraday geometry (see details in the text). The modes with $\varsigma = \pm 1$ correspond to either opposite circular polarizations or propagation directions. Numerical simulations of exact equations (symbols) and the theoretical formula (4.8) (lines).

In the Voigt geometry, the dielectric tensor is[22]

$$\hat{\varepsilon} = \varepsilon\begin{Vmatrix} 1 & 0 & iq \\ 0 & 1 & 0 \\ -iq & 0 & 1 \end{Vmatrix}.$$

The first-order interaction of the wave with the magnetization occurs only upon oblique propagation of the wave in the xz plane, i.e., when $k_x = \text{const} \neq 0$ (see Fig. 21).

The eigenmodes of the problem are the TE mode, which is uncoupled from magnetization, and the TM mode with tangential components

$$H_y^{\upsilon,\varsigma} = H^{\upsilon,\varsigma} e^{i(\varsigma x k_\perp + \upsilon z k_{||} - \omega t)}, \quad E_x^{\upsilon,\varsigma} = A^{\upsilon,\varsigma} H_y^{\upsilon,\varsigma}.$$

Here, parameters $\upsilon = \pm 1$ and $\varsigma = \pm 1$ indicate propagation in the positive and negative z and x directions, respectively, $k_{||} = \sqrt{k^2 - k_x^2}$, $k_\perp = |k_x|$, whereas

$$A^{\upsilon,\varsigma} = -(A^{-\upsilon,\varsigma})^* = \frac{i\varsigma q k_\perp + \upsilon k_{||}}{\varepsilon(1-q^2)k_0}, \quad k = nk_0\sqrt{1-q^2}. \tag{4.9}$$

In the linear approximation in q, $A^{\upsilon,\varsigma} \simeq (\upsilon k_{||} + i\varsigma q k_\perp)/(\varepsilon k_0)$, and $k \simeq nk_0$, so that magnetization affects imaginary parts (i.e., phases) of the amplitudes $A^{\upsilon,\varsigma}$, and does not affect the propagation constant, cf. Eqs. (4.5) and (4.6).

In the Voigt geometry, direction of the transverse wave vector component, ς, serves as the mode index. The mutually reciprocal waves are $H^{\upsilon,\varsigma}$ and $H^{-\upsilon,-\varsigma}$, because the time reversal transformation reverts the whole wave vector, $\mathbf{k} \mapsto -\mathbf{k}$.

The parameter ς is not changed upon reflection and transmission through the layers, i.e., modes with $\varsigma = \pm 1$ are uncoupled from each other. Therefore, for the sake of simplicity we omit the mode index in superscripts and write explicitly only the values of the direction parameter $\upsilon = \pm 1$.

Using standard boundary conditions for the electric and magnetic fields of the wave at the "α"–"β" interface, for the normalized interface transfer matrix $\hat{F}^{\alpha\beta}$ we obtain[88]

$$\hat{F}^{\alpha\beta} = \frac{1}{\sqrt{4\mathrm{Re}\,A_\alpha^+\,\mathrm{Re}A_\beta^+}}\begin{Vmatrix} A_\beta^+ + A_\alpha^{+*} & A_\alpha^{+*} - A_\beta^{+*} \\ A_\alpha^+ - A_\beta^+ & A_\alpha^+ + A_\beta^{+*} \end{Vmatrix}.$$

In contrast to the Faraday geometry, in Voigt geometry the linear magnetooptical correction changes only the phases of transmission and reflection coefficients, whereas corrections to the interface transmittance start with the terms $\propto q^2$. In the short-wave limit, only these transmittances determine the total transmittance, Eq. (4.2). Therefore, a short-wavelength transmission through a random multilayered stack is reciprocal and is not affected by magnetization in the first-order approximation. In the short-wave limit, this statement remains true for any number of types of alternating layers. It was verified numerically for the three-layer system.[34] At the same time, a periodic structure with a cell consisting of three different layers (which breaks the mirror reflection symmetry) can demonstrate significant nonreciprocity,[88,89] but beyond the short-wave approximation.

Averaged localization decrement is associated with exponential decay of the incident wave deep into the infinite sample.[5,39,49,56] For a finite sample, this is so only for typical realizations. However, there exist some resonant realizations of the sample at a given frequency (or, equivalently, resonant frequencies for a given realization), where transmission is anomalously high and is accompanied by the accumulation of energy inside the sample.[76,90,91] Such resonant transmission corresponds to excitation of the Anderson localized states (quasi-modes) inside the sample.

Akin to the resonant localized states in photonic crystal cavities, transmission resonances in random structures are extremely sensitive to small perturbations: realization,[76] absorption,[91] nonlinearity,[31] and, as we show here, magnetoactivity.

Figure 23 shows transmission spectra for two modes $\varsigma = \pm 1$ (i.e., either with opposite helicities or propagation directions) in one realization of a magnetooptical sample in the Faraday geometry. Parameters of the sample are the same as in Sec. 3.1 with $Q = 0.06$. One can see strong splitting of the $\varsigma = \pm 1$ transmission resonances, which have exponentially narrow widths[91] $\propto \kappa \exp(-\kappa N)/2\overline{w}$. This offers strongly nonreciprocal, practically unidirectional propagation or polarization selectivity in vicinity of resonant frequencies.

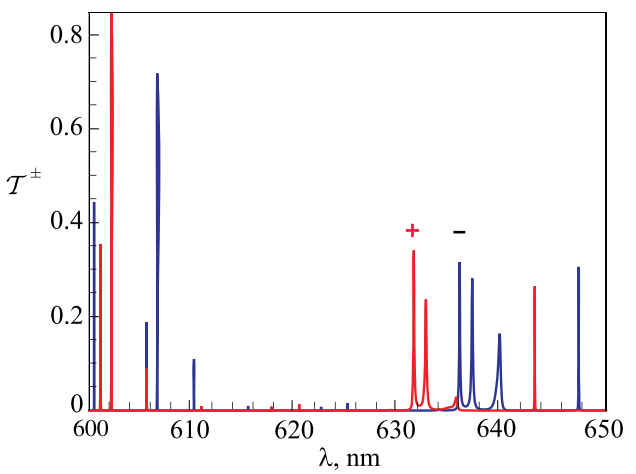

FIG. 23. (Ref. 34) Transmission spectra of a random magnetooptical sample in the Faraday geometry (see details in the text) for waves with $\varsigma = \pm 1$. While the averaged localization decrements are only slightly different (Fig. 22), all individual resonances are shifted significantly as compared with their widths, Eq. (4.10).

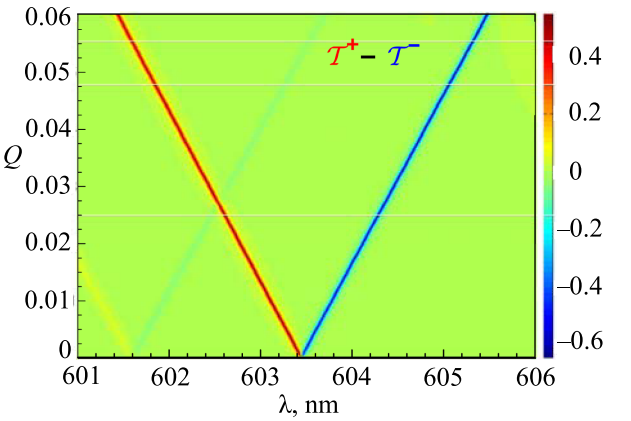

FIG. 24. (Ref. 34) Differential transmittance, $\mathcal{T}^+ - \mathcal{T}^-$, for two resonances from Fig. 22 as dependent on the value of magnetooptical parameter Q, cf. Eq. (4.10).

To estimate the splitting of resonances we note that wavenumbers in magnetooptical materials are shifted due to the Faraday Effect (Eq. (4.6)). Hence, the shifts of resonant wavenumbers of a random Faraday medium can be estimated by averaging of this shift over different materials in the structure:

$$\Delta k_{\mathrm{res}} \simeq \varsigma \frac{\overline{qnk_0}}{2}, \tag{4.10}$$

where $\overline{(\ldots)}$ stands for some average of $(\ldots)$. Using $\overline{qn} \sim (q_a n_a + q_b n_b)/2$ for the estimation in a two-component structure, we obtain $\Delta\lambda_{\mathrm{res}} \sim -\varsigma\, 3.6\,\mathrm{nm}$, which agrees with the ς-dependent splitting observed in Fig. 23.

Figure 24 displays the differential transmission for the waves with $\varsigma = +1$ and ς lying in a narrow frequency range in Fig. 23. In agreement with estimation Eq. (4.10), one observes the linear dependence of the resonance splitting on magnetization.

In the Voigt geometry, the resonances also allow nonreciprocal transmission and demonstrate splitting of the resonant frequencies. In Fig. 25, differential transmission is shown for reciprocal waves with $\varsigma = \pm 1$ in vicinity of one resonance for the three-component structure considered in Sec. 3.2. The splitting is very small in this case, and $\varsigma = +1$ and $\varsigma = -1$ resonances overlap significantly. Because of this,

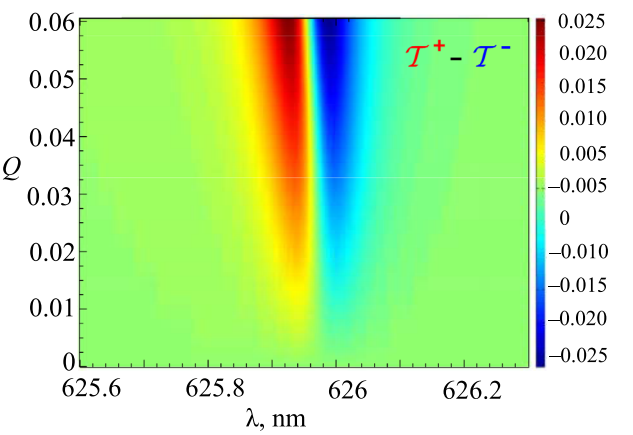

FIG. 25. (Ref. 34) Differential transmittance, $\mathcal{T}^+ - \mathcal{T}^-$, in the vicinity of a single resonance in the Voigt geometry (see Sec. 3.2 for details) as dependent on the magnetooptical parameter Q.

the differential transmittance in Fig. 25 is tiny, its amplitude linearly grows with Q, whereas the frequency positions of its maximum and minimum correspond to the width of the original resonance and are practically unchanged.

Unlike the wave-number shift in the Faraday geometry, the noreciprocal shift of resonant frequencies in the Voight geometry arises from the phases of the amplitudes A, Eq. (4.9). These phases are responsible for the phases estimated as $\phi \sim q(\varsigma k_\perp)/(\upsilon k_{||}) \equiv q \tan\theta$, where θ is the angle of propagation with respect to the z axis. Phases accumulated at a layer effectively shift the wavenumbers as $\upsilon \Delta k_{||} = \Delta k \cos\theta \sim \phi/w$, where w is the thickness of the layer. Averaging over different materials in the random layered structure, we estimate the nonreciprocal shift of the resonant wavenumber:

$$\Delta k_{\rm res} \sim \frac{\overline{q \sin\theta}}{w \cos^2\theta} = \varsigma \frac{\overline{q|\sin\theta|}}{w \cos^2\theta}.$$

This shift is ς-dependent, i.e., nonreciprocal, and much smaller than the Faraday-geometry shift Eq. (4.10) as $k\overline{w} > kd \gg 2\pi$ in the short-wavelength limit. For the parameters in use, with $Q = 0.06$, we have $\Delta\lambda_{\rm res} \sim -\varsigma 3 \cdot 10^{-4}$ nm, which agrees with the data plotted in Fig. 25.

4.2. Charge transport in disordered graphene

Shortly after the discovery of highly unusual physical properties of graphene it was realized that the electron transport in this material had many common features with the propagation of light in dielectrics. Historically, the analogy between Maxwell equations and those used in the relativistic electron theory has been discussed in different contexts and for various purposes (see, for example,[47,92–94]) since 1907, when Maxwell equations were reduced[95] to an alternative, more concise form by introducing a complex field $\mathbf{F} = \mathbf{E} + i\mathbf{H}$:

$$c\hat{\boldsymbol{\rho}} \cdot \nabla\Psi = -n\partial\Psi/\partial t, \tag{4.11}$$

where Ψ is the 4-vector with components $-F_x + iF_y$, F_z, F_z, $F_x + iF_y$, n is the refraction index, and the components of the 3-vector $\hat{\boldsymbol{\rho}}$ are the Dirac matrices $\hat{\rho}_i$, $i = 1,2,3$ (Pauli matrices in which the units are replaced by the unit 2×2 matrices).

In the last few years this activity has perked up due to recent developments in the physics of graphene. Nowadays it is well understood that under some (rather general) conditions, Dirac equations describing charge transport in a graphene superlattice created by applying inhomogeneous external electric potential could be reduced to Maxwell equations for the propagation of light in a dielectric medium. To better understand the physics of charge transport in graphene subject to a coordinate-dependent potential, in what follows we compare the results for graphene with those for the propagation of light in layered dielectric media (for more analogies between quantum and optical systems see Refs. 96 and 97). Additional analogies, not discussed here, also exist with the transport and localization of phonons in different kinds of periodic and random one-dimensional structures.[98–100]

As it was shown above, the light transport of electromagnetic waves in multilayered media is described in terms of the transfer matrices of two types. The first type is formed by diagonal matrices $\hat{S}_j$ corresponding to the propagation of wave through the jth layer. These matrices are the same as in Eq. (2.20) (up to the signs of the exponent). The second type is formed by the interface transfer matrices $\hat{F}_{j,(j+1)}$ describing transformation of the amplitudes of electromagnetic waves at the interface between jth and $(j+1)$-th layers and having the form

$$\hat{F}_{j,j+1} = \frac{1}{2\cos\theta_{j+1}} \begin{Vmatrix} G^{(+)}_{j,j+1} & G^{(-)}_{j,j+1} \\ G^{(-)}_{j,j+1} & G^{(+)}_{j,j+1} \end{Vmatrix}, \tag{4.12}$$

where

$$G^{(\pm)}_{j,j+1} = \cos\theta_{j+1} \pm \cos\theta_j \cdot {\rm sgn}(\nu_j\nu_{j+1}) \frac{Z_{j+1}}{Z_j} \tag{4.13}$$

for s-polarized waves, and

$$G^{(\pm)}_{j,j+1} = \frac{Z_{j+1}}{Z_j} \cos\theta_{j+1} \pm \cos\theta_j \cdot {\rm sgn}(\nu_j\nu_{j+1}) \tag{4.14}$$

for p-polarized waves. Here, θ_j is the angle of propagation within the jth layer, Z_j and ν_j are the impedance and the refractive index of the jth layer, respectively, defined by Eq. (3.1). Signs $\pm$ correspond, respectively, to R- and L-dielectric layers with positive and negative refractive indices.

In the case of charge transport in a graphene superlattice created by a piecewise-constant, electrostatic potential depending on one coordinate x in the plane (x, y) of the graphene layer, the analogues transfer matrix, which describes the transition through the interface between adjacent regions with different values of the potential, has the form[47]

$$\hat{\mathcal{F}}_{j,j+1} = \frac{1}{2\cos\theta_{j+1}} \begin{Vmatrix} \mathcal{G}^{(+)}_{j,j+1} & \mathcal{G}^{(-)}_{j,j+1} \\ (\mathcal{G}^{(-)}_{j,j+1})^* & (\mathcal{G}^{(+)}_{j,j+1})^* \end{Vmatrix}, \tag{4.15}$$

where

$$\mathcal{G}^{(\pm)}_{j,j+1} = {\rm e}^{-i\theta_{j+1}} \pm {\rm e}^{\pm i\theta_j} \cdot {\rm sgn}[(\varepsilon - u_j)(\varepsilon - u_{j+1})]. \tag{4.16}$$

Here, the θ_j is given by equation $\tan\theta_j = \beta/\sqrt{(\varepsilon - u_j)^2 - \beta^2}$, where β is the projection of the dimensionless momentum on y axis, ε and u_j are the dimensionless energy of the charge carrier and the scalar potential of the jth layer. If θ_j is real, it coincides with the angle of propagation of electron within the jth layer.

Comparison of Eqs. (4.12) and (4.15) shows that the role of refractive index ν in graphene is played by the difference $\varepsilon - u$. In particular, a layer, in which the potential exceeds the energy of the particle, $u > \varepsilon$, is similar to an L-slab with negative refractive index (metamaterial), while a layer where $u < \varepsilon$ is similar to normal material. It is due to this similarity that a junction of two regions having opposite signs of $u - \varepsilon$ (the so-called p–n junction) focuses Dirac electrons in graphene,[48] in the same way as an interface between left- and right-handed dielectrics focuses electromagnetic waves.[16]

This analogy is not complete: although the equations are akin, the boundary conditions are, generally speaking, different. As a result Eq. (4.16) (for graphene) does not contain

the factor Z_{j+1}/Z_j, which is present in Eqs. (4.13) and (4.14), and determines the reflection coefficients at the boundary between two dielectrics.[101] Another important distinction between transfer matrices $\hat{\mathcal{F}}$ (graphene) and $\hat{F}$ (electromagnetic waves) is that $\hat{\mathcal{F}}$ is a complex-valued matrix, while $\hat{F}$ is always real. This is a manifestation of the fundamental difference between graphene wave functions and electromagnetic fields in dielectrics. Graphene wave functions are complex-valued spinors that describe two different physical objects: particles (electrons) and antiparticles (holes). Electromagnetic fields are real, which reflects the fact that photons do not have antiparticles (an antiphoton is identical to a photon). These distinctions bring about rather peculiar dissimilarities between the conductivity of graphene and the transparency of dielectrics.

However in the particular case of normal incidence $\theta_j = \theta_{j+1} = 0$ and equal impedances $Z_j = Z_{j+1}$, transmission of Dirac electrons through a junction is similar to the transmission of light via an interface between two media with different refractive indices (but equal impedances). Such an interface is absolutely transparent to light, and, therefore both p–n and p–p junctions are absolutely transparent to the Dirac electrons in graphene.[48,102] This is related to the absence of backscattering and antilocalization of massless Dirac fermions caused by their spin properties.[29,30] This also explains the Klein paradox[103] (perfect transmission through a high potential barrier) in graphene systems, and leads (together with symmetry and spectral flow arguments) to the surprising conclusion that Dirac electrons are delocalized in disordered 1D graphene structure, providing a minimal nonzero overall transmission, which cannot be destroyed by fluctuations, no matter how strong they are.[104] However, this statement (being correct in some sense) should be perceived with a certain caution. Indeed, many features of Anderson localization can be found in random graphene systems. It has been shown in Ref. 94 that although wave functions of normally incident ($\theta = 0$) particles are extended and belong to the continuous part of the spectrum, away from some vicinity of $\theta = 0$, 1D random graphene systems manifest all the features of disorder-induced strong localization. In particular, for a long enough, disordered graphene superlattice the transmission coefficient T as a function of the angle of incidence, θ (or of the energy E, if $\theta \neq 0$ is fixed) has the typical for Anderson localization shape (see Fig. 26).

Along with continuous directions of typical angles (or energies), for which transmission is exponentially small, there exists a quasi-discrete random set of directions, where the sample is well transparent, i.e., the transmission coefficient is close to one. At these angles the wave functions are exponentially localized (Fig. 27), with the Lyapunov exponent (inverse localization length l_ξ) being proportional to the strength of disorder.

Charge transport in a graphene sheet subjected to a disordered electrostatic potential is determined by the ratio between its values $u(\xi)$ and the energy ε of the particle. In particular, in a randomly-layered potential $u_j = u_0(j) + \Delta u_j$ (j is the number of the layer, $u_0(j)$ is a nonrandom function, Δu_j are independent random variables homogeneously distributed in the interval $[-\delta u, \delta u]$) it manifests essentially different features in the following three different systems:[94]

(i) $u_j < \varepsilon$, $u_0(j)$ is a periodic function. In this case, a relatively weak disorder drastically changes the transmission spectrum. All features of the spectrum of the underlying periodic structure are washed out, and a rather dense (quasi-)discrete angular spectrum appears, with the corresponding wave functions being localized at random points inside the sample (disorder-induced resonances). However, there is one fundamental difference from the usual Anderson localization: in vicinity of normal incidence the transmission spectrum of graphene is continuous with extended wave functions, and the transmission coefficient is finite ($T = 1$ at $\theta = 0$). It is this range of angles that provides the finite minimal conductivity, which is proportional to the integral of $T(\theta)$ over all angles θ.

(ii) $\varepsilon \leq u_0\ (j) = \text{const}$. Under these conditions, the transmission of an unperturbed system is exponentially small (tunnelling) and, rather unusually, gets enhanced by the fluctuation of the potential.

(iii) $\varepsilon = 0$, $u_0(j)$ is a periodic set of numbers with alternating signs. The behavior of charge carriers in potential of this type is most unusual. It is characteristic of two-dimensional Fermions and has no analogies in electron and light transport. The disorder obliterates the transmission peaks of the underlying periodic system, makes the transparency zone around normal angle of incidence much wider, and gives rise to a new narrow peak in the transmission coefficient,

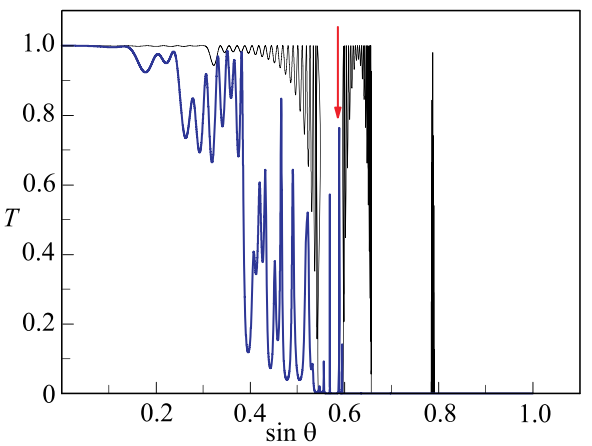

FIG. 26. (Ref. 47) Transmission coefficient $T(\theta)$ for periodic (thin black line) and disordered (bold blue line) graphene.

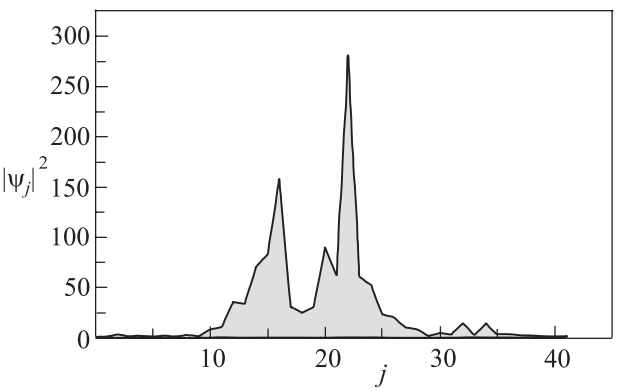

FIG. 27. (Ref. 47) Spatial distribution of wave function localized inside the sample for θ, marked by red arrow in Fig. 26.

associated with wave localization in the random potential. Unlike peaks in the periodic structure, the wave function of this disorder-induced resonance is exponentially localized. In distinction to case (i), the transmission in (iii) is extremely sensitive to fluctuations of the applied potential: relative fluctuations $\Delta u/u_0 = 0.05$ reduce the angular width of the transmission spectrum more than four times.

Propagation of light in analogous L–R and R–R disordered dielectric structures demonstrates completely different behavior. As the degree of disorder (variations of the refractive index) grows, the averaged angular spectra quickly reach their asymptotic "rectangular" shape: a constant transmission in the region where all interfaces between layers are transparent followed by an abrupt decrease in transmission in the region of angles where the total internal reflection appears.

4.3. Bistability of Anderson localized states in nonlinear media

The recently renewed interest in Anderson localization is driven by a series of experimental demonstrations in optics[12–14] and Bose–Einstein condensates.[15,105] One of the important issues that has risen in these studies is that disordered systems can be inherently nonlinear, so that an intriguing interplay of nonlinearity and disorder could be studied experimentally.

Nonlinear interaction between propagating waves and disorder can significantly change the interference effects, thus fundamentally affecting localization.[32,33,67,77] However, most of the studies of localization in random nonlinear media deal with the ensemble-averaged characteristics of the field, such as the mean field and intensity, correlation functions, etc. These quantities describe the averaged, typical behavior of the field, but they do not contain information about individual localized modes (resonances), which exist in the localized regime in each realization of a random sample.[9,67,77,91,106] These modes are randomly located in both real space and frequency domain and are associated with the exponential concentration of energy and resonant tunnelling. In contrast to regular resonant cavities, the Anderson modes occur in a statistically-homogeneous media because of the interference of the multiply scattered random fields. Although disorder-induced resonances in linear random samples have been the subject of studies for decades, resonance properties of nonlinear disordered media have not been explored so far.

In this section we present the study of the effect of nonlinearity on the Anderson localized states in a one-dimensional random medium.[31] As a result of interplay of nonlinearity and disorder, bistability and nonreciprocity appear upon resonant wave tunnelling and excitation of disorder-induced localized modes in a manner similar to that for regular cavity modes. At the same time, weak nonlinearity has practically no effect on the averaged localization background.

First, let us consider a stationary problem of the transmission of a monochromatic wave through a one-dimensional random medium with Kerr nonlinearity. The problem is described by the equation,

$$\frac{d^2\Psi}{dx^2} + k^2[n^2 - \chi|\psi|^2]\psi = 0, \tag{4.17}$$

where ψ is the wave field, x is the coordinate, k is the wave number in the vacuum, $n = n(x)$ is the refractive index of the medium, and χ is the Kerr coefficient.

In the linear regime, $\chi|\psi|^2 = 0$, multiple scattering of the wave on a random inhomogeneity $n^2(x)$ brings about Anderson localization. The main signature of the localization is exponential decay of wave intensity $I = |\psi|^2$ deep into the sample and, thus, an exponentially small transmission:[1,2,5,56] $I_{\text{out}}^{(\text{typ})} \sim I_{\text{in}} \exp(-2L/l) \ll 1$. Here, L is the length of the sample, and l is the localization length, which is the only spatial scale of Anderson localization. Along with the typical wave transmission, there is an anomalous, resonant transmission, which accompanies excitation of the Anderson localized states inside the sample and occurs at random resonant wave numbers $k = k_{\text{res}0}$.[9,67,77,91,106] In this case, the distribution of intensity in the sample is characterized by an exponentially localized high-intensity peak inside the sample, $I_{\text{peak}} \gg I_{\text{in}}$, and a transmittance much higher than the typical one: $I_{\text{out}}^{(\text{res})} \gg I_{\text{out}}^{(\text{typ})}$.

Excitation of each localized mode inside the random sample can be associated with an effective resonator cavity located in the area of field localization and bounded by two potential barriers with exponentially small transparencies.[78] According to this model, the transmittance spectrum $T(k, I_{\text{out}})$ in vicinity of a resonant wavelength for the case of weak nonlinearity ($\chi\,|\psi|^2 \ll 1$) is given in the form,[10,31,91]

$$T(k, I_{\text{out}}) \equiv \frac{I_{\text{out}}}{I_{\text{in}}} = \frac{T_{\text{res}}}{1 + [A\chi I_{\text{out}} + \delta]^2}, \tag{4.18}$$

where T_{res} is the transmission coefficient at resonance, and dimensionless parameters A and δ characterize, respectively, the strength of the nonlinear feedback and the detuning from the resonant wave number,

$$A = \frac{2Q}{\chi}\frac{d\ln k_{\text{res}}}{dI_{\text{out}}}\bigg|_{I_{\text{out}}=0}, \quad \delta = 2Q\left(1 - \frac{k}{k_{\text{res}0}}\right). \tag{4.19}$$

Equation (4.18) establishes a relation between the input and output wave intensities, which is given by a cubic equation with respect to I_{out}. It has a universal form typical for nonlinear resonators possessing optical bistability.[107] From Eq. (4.19) it follows that in the region of parameters

$$A\delta < 0, \quad \delta^2 > 3, \quad |\chi| I_{\text{in}} > \frac{8}{3\sqrt{3}}\frac{1}{|A|T_{\text{res}}},$$

the dependence $I_{\text{out}}(I_{\text{in}})$ is of the S-type, and the stationary transmission spectrum $T(k)$ is a three-valued function. In most cases, one of the solutions is unstable, whereas the other two form a hysteresis loop in the $I_{\text{out}}(I_{\text{in}})$ dependence (see Figs. 28 and 29).

It is important to emphasize two features of the Eqs. (4.18) and (4.19), describing nonlinear resonant transmission through a localized state. First, they have been derived without any approximations apart from the natural smallness of the nonlinearity and Lorentzian shape of the spectral line. Second, although resonant transmission and the effect of nonlinearity and bistability owe their origin to the excitation

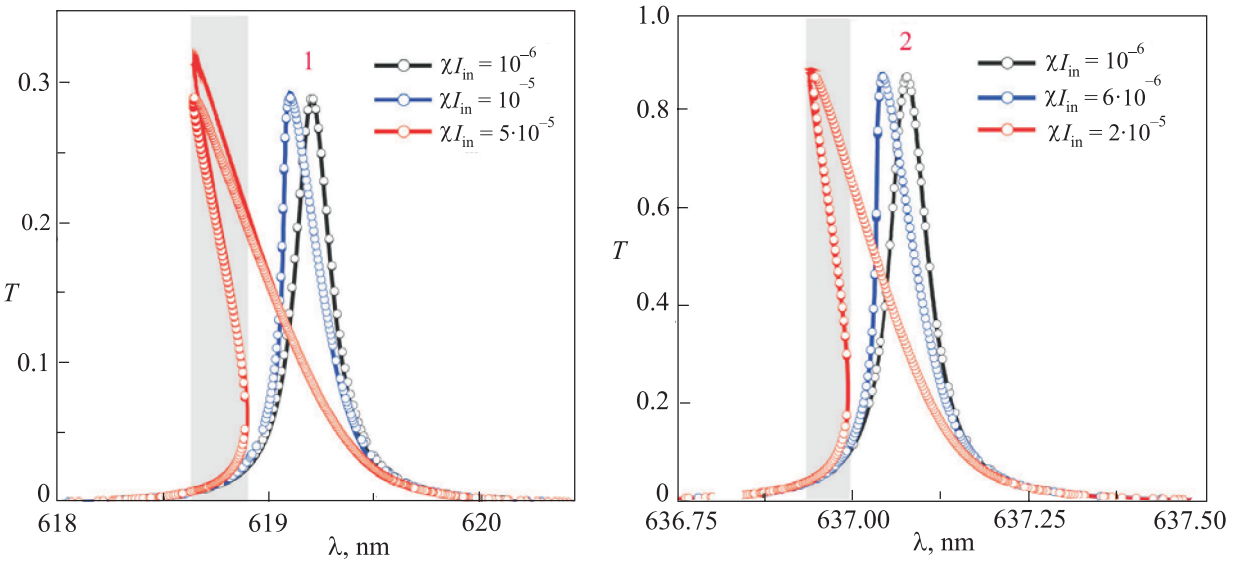

FIG. 28. (Ref. 31) Nonlinear deformations of transmission spectra of two random resonances at different intensities of the incident wave. Numerical simulations of the Eq. (4.17) (curves) and theoretical Eq. (4.18) (symbols) are shown for the case of defocusing nonlinearity, $\chi > 0$. Light-grey stripes indicate three-valued regions for the high-intensity curves, where only two of them (corresponding to the lower and upper branches) are stable.

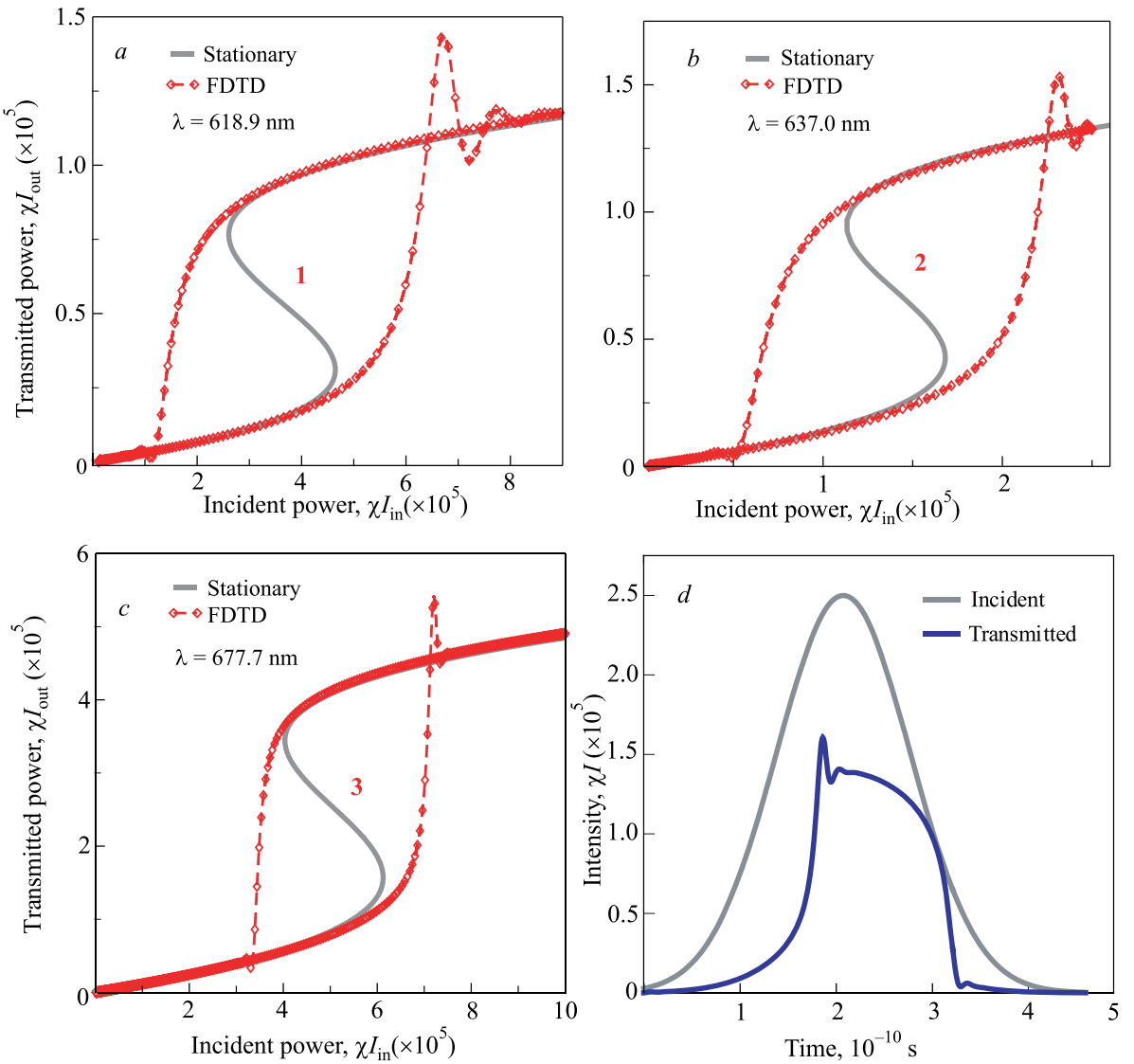

FIG. 29. (Ref. 31) Stationary and FDTD simulations showing hysteresis loops in the output vs input power dependence for three different resonances. Panel (d) shows deformation of the transmitted Gaussian pulse corresponding to the hysteresis switching on resonance 2.

of the Anderson localized mode inside a sample, Eqs. (4.18) and (4.19) contain only quantities which can be found via outside measurements.[31]

Figure 28 shows nonlinear deformations of the resonant transmission spectra $T(k)$ for different values of I_{in}, which exhibit transitions to bistability. The analytical dependence $T(k)$ given by Eqs. (4.18) and (4.19) with parameters T_{res}, Q, and A found from numerical experiments, are in excellent agreement with the direct numerical solutions of Eq. (4.17).[108] In numerical simulations of stationary regime we used the standard 4th order Runge–Kutta method. We note that the incident field amplitude is a single-valued function of the transmitted field. Thus, we solve second-order ordinary differential equation Eq. (4.17) using transmitted field value as the boundary condition for the equation.

The dimensionless parameters T_{res} and Q from Eqs. (4.18) and (4.19), can also be estimated from a simple resonator model of the Anderson localized states,[9,78,91]

$$T_{res} = \frac{4T_1T_2}{(T_1+T_2)^2}, \quad Q^{-1} \sim \frac{T_1+T_2}{4k_{res0}l}, \tag{4.20}$$

where

$$T_1 \sim \exp[-2x_{res}/l], \quad T_2 \sim \exp[-2(L-x_{res})/l]$$

are the transmission coefficients of the two barriers that form the effective resonator, x_{res} is the coordinate of the center of the area of field localization; l is the localization length, and L is the length of the sample.

Introducing a weak Kerr nonlinearity into the resonator model, one can also estimate the nonlinear feedback parameter A,

$$A \sim Q/\overline{n^2}T_2, \tag{4.21}$$

where $\overline{n^2}$ is the mean value of $n^2(x)$.

It is important to note that each disorder-induced resonance is associated with its own effective cavity, so that the disordered sample can be considered as a chain of randomly located coupled resonators.[11]

Equations (4.20) and (4.21) enable one to estimate the values of parameters describing the nonlinear resonant wave tunnelling in Eqs. (4.20) and (4.21) by knowing only the basic parameters of the localization—the localization coordinate and the localization length. In particular, substituting Eqs. (4.20) and (4.21) into Eq. (4.19) and taking into account that the most pronounced transmission peaks correspond to localized states with $x \simeq L/2$ and $T_1 \sim T_2$, we estimate the incident power needed for bistability of localized states to be

$$|\chi|I_{in} \gtrsim \frac{\exp(-2L/l)}{k_{res0}l}. \tag{4.22}$$

For the parameters used in our simulations this gives quite a reasonable value $|\chi|I_{in} \gtrsim 10^{-5}$. If we increase the length of the sample, the Q-factors of the resonances grow, and the incident power needed to observe the bistability becomes smaller.

To demonstrate temporal dynamics upon bistable resonant tunnelling, an explicit iterative nonlinear finite-difference time-domain (FDTD) scheme was implemented. For precise modelling of the spectra of narrow high-Q resonances, a fourth-order accurate algorithm was used, both in space and in time,[109] as well as the Mur boundary conditions to simulate open boundaries and total-field/scattered-field technique for exciting the incident wave. Sufficient accuracy was achieved by creating a dense spatial mesh of 300 points per wavelength ($dx = \lambda/300$). To assure stability of the method in nonlinear regime, the time step was selected as $dt = dx/3c$, and each simulation ran for $N = 2\cdot10^8$ time steps. To compare the results of FDTD simulations with the steady-state theory, the transmission of long Gaussian pulses with central frequencies and amplitudes satisfying conditions Eq. (4.22) was considered, see Fig. 29(d). With an appropriate choice of signal frequencies, we observe hysteresis loops in the $I_{out}(I_{in})$ dependences, which are in excellent agreement with stationary calculations, as shown in Figs. 29(a)–29(c). Characteristic transitional oscillations accompany jumps between two stable branches, and strong reshaping of the transmitted pulse evidences switching between the two regimes of transmission, Fig. 29(d). We note that different choice of signal frequencies near the resonance can lead to various other behaviors of output vs. input curves, with transmission either increasing when nonlinear resonance frequency shifts towards the signal frequency, or decreasing in the opposite case.

In addition to bistability, the resonant wave tunneling through a nonlinear disordered structure is nonreciprocical. As is known for regular systems, nonsymmetric nonlinear systems may possess nonreciprocal transmission properties, resembling the operation of a diode. An all-optical diode is a device that allows unidirectional propagation of a signal at a given wavelength, which may become useful for many applications.[110] A disordered structure is naturally asymmetrical in the generic case, and one may expect a nonreciprocal resonant transmission in the nonlinear case. To demonstrate this, we modeled propagation of an electromagnetic pulse impinging the same sample from different sides and monitored the transmission characteristics. One case of such nonreciprocical resonant transmission is shown in Fig. 30(a). We observe considerably different transmission properties in opposite directions with the maximal intensity contrast between two directions 7.5:1. Moreover, the threshold of bistability is also significantly different for two directions: there is a range of incident powers, for which the wave incident from one side of the sample is bistable, while there are no signs of bistability for the incidence from the other side. Figure 30(b) shows pulse reshaping for incidence from opposite sides of the structure.

In this section we have presented the study of new manifestations of the interplay between nonlinearity and disorder. It is shown that even weak nonlinearity dramatically affects resonant transmission associated with the excitation of the Anderson localized states leading to bistability and nonreciprocity. Despite random character of the appearance of Anderson modes, their behavior and evolution are rather deterministic, and, therefore, these modes can be used for efficient control of light similar to regular cavity modes. These results demonstrate that, unlike infinite systems, the Anderson localization in finite samples is not destroyed by weak nonlinearity—instead it exhibits new intriguing features typical for resonant nonlinear systems.

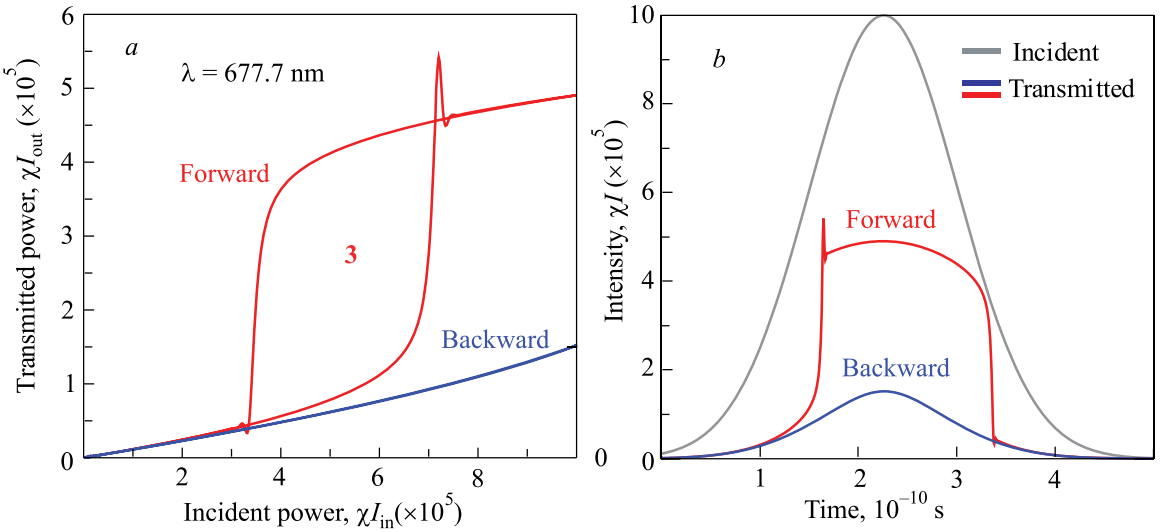

FIG. 30. (Ref. 31) (a) Nonreciprocal transmission through the nonlinear disordered structure, showing different output powers for identical waves incident from different directions. (b) Corresponding shape of the incident pulse, and pulses transmitted in different directions.

Conclusion

We have reviewed the transmission and localization wave properties of complex disordered structures composed of (i) left-handed metamaterials, (ii) magnetoactive optical materials, (iii) graphene superlattices, and (iv) nonlinear dielectric media. Interference origin of wave localization, together with strong energy concentration, makes Anderson localization highly sensitive to weak modifications of the material properties. We have shown that exotic properties of novel materials can drastically modify the main features of wave localization. This brings about anomalous pronounced dependences of wave transmittance and localization length on both wave and material parameters: frequency, angle of incidence, polarization, magnetization, nonlinearity, etc. As a result, remarkable phenomena appear, such as anti-(de-)localization, unidirectional transmission, slow-light propagation, and bistability.

We have described a number of novel features accompanying wave localization in complex media, including: (i) dramatic suppression of localization in mixed stacks with left-handed metamaterials, (ii) Brewster, zero-ε, and zero-μ delocalization, and (iii) anomalous transmission enhancement in periodic metamaterials with only one disordered electromagnetic characteristics, (iv) nonreciprocal localization and unidirectional transmission through magnetoactive disordered stacks, (v) angle-dependent transmission resonances in graphene superlattices, and (vi) bistability and nonreciprocity of transmission resonances in nonlinear disordered structures.

We believe that the results presented significantly extend and enrich theory and potential application of wave localization in complex disordered media. In particular, they provide a theoretical toolbox that can serve for design of novel optical and electronic devices with unusual transport properties.

We are pleased to dedicate this review paper to the 80th anniversary of Academician Victor Valentinovich Eremenko and wish him good health, good mood, and new scientific achievements.

We also thank our co-authors, especially L. C. Botten, M. A. Byrne, R. C. McPhedran, F. Nori, P. Rajan, and S. Savel'ev for the fruitful collaboration and discussions of many original results summarized in this review paper. S.G. is grateful to N. M. Makarov, P. Markos, and L. A. Pastur for useful comments and helpful discussions.

This work was partially supported by the European Commission (Marie Curie Action). V.F. acknowledges partial support from the Israeli Science Foundation (Grant No. 894/10).

[a]Email: sergeyg@bgu.ac.il

[1]P. W. Anderson, Phys. Rev. **109**, 1492 (1958).
[2]I. M. Lifshits, S. A. Gredeskul, and L. A. Pastur, *Vvedenye v Teoriu Neuporyadochennykh System* (Nauka, Moskva, 1987); *Introduction to the Theory of Disordered Systems* (Wiley, New York, 1987).
[3]Y. Imry, *Introduction to Mesoscopic Physics* (Oxford University Press, Oxford, 2002).
[4]S. John, Phys. Rev. Lett. **53**, 2169 (1984).
[5]P. Sheng, *Scattering and Localization of Classical Waves in Random Media* (World Scientific, Singapore, 1991).
[6]P. Sheng, *Introduction to Wave Scattering, Localization, and Mesoscopic Phenomena* (Academic, San Diego, 2007).
[7]P. Marcos and C. M. Soukoulis, *Wave Propagation from Electrons to Photonic Crystals and Left-Handed Materials* (Princeton University Press, Princeton, 2008).
[8]*Years of Anderson Localization*, edited by E. Abrahams (World Scientific, London, 2010).
[9]K. Y. Bliokh, Y. P. Bliokh, V. Freilikher, A. Z. Genack, B. Hu, and P. Sebbah, Phys. Rev. Lett. **97**, 243904 (2006).
[10]P. Sebbah, B. Hu, J. M. Klosner, and A. Z. Genack, Phys. Rev. Lett. **96**, 183902 (2006).
[11]K. Y. Bliokh, Y. P. Bliokh, V. Freilikher, A. Z. Genack, and P. Sebbah, Phys. Rev. Lett. **101**, 133901 (2008).
[12]J. Bertolotti S. Gottardo, D. S. Wiersma, M. Ghulinyan, and L. Pavesi, Phys. Rev. Lett. **94**, 113903 (2005); J. Topolancik, B. Ilic, and F. Vollmer, Phys. Rev. Lett. **99**, 253901 (2007).
[13]T. Schwartz, G. Bartal, S. Fishman, and M. Segev, Nature **446**, 52 (2007).
[14]Y. Lahini, A. Avidan, F. Pozzi, M. Sorel, R. Morandotti, D. N. Christodoulides, and Y. Silberberg, Phys. Rev. Lett. **100**, 013906 (2008).
[15]J. Billy, V. Josse, Z. Zuo, A. Bernard, B. Hambrecht, P. Lugan, D. Clèment, L. Sanchez-Palencia, P. Bouyer, and A. Aspect, Nature **453**, 891

(2008); G. Roati, C. D'Errico, L. Fallani, M. Fattori, C. Fort, M. Zaccanti, G. Modugno, M. Modugno, and M. Inguscio, Nature **453**, 895 (2008).
[16]V. G. Veselago, Sov. Phys. Usp. **10**, 509 (1968).
[17]J. B. Pendry, Phys. Rev. Lett. **85**, 3966 (2000).
[18]V. M. Shalaev, Nat. Photonics **1**, 41 (2007).
[19]M. I. Katsnelson and K. S. Novoselov, Solid State Commun. **143**, 3 (2007).
[20]A. K. Geim and K. S. Novoselov, Nature Mater. **6**, 183 (2007).
[21]C.-H. Parc, L. Yang, Y.-W. Son, M. Cohen, and S. Louie, Nature Phys. **4**, 213 (2008).
[22]A. K. Zvezdin, and V. A. Kotov, *Modern Magnetooptics and Magnetooptical Materials* (IOP, Bristol and Philadelphia, 1997).
[23]A. Yamilov and H. Cao, Phys. Rev. E **70**, 037603 (2004); B. Payne, J. Andreasen, H. Cao, and A. Yamilov, Phys. Rev. B **82**, 104204 (2010).
[24]V. Freilikher, M. Pustilnik, and I. Yurkevich, Phys. Rev. B **50**, 6017 (1994).
[25]J. C. J. Paasschens, T. Sh. Misirpashaev, and C. W. J. Beenakker, Phys. Rev. B **54**, 11887 (1996).
[26]A. A. Asatryan, N. A. Nicorovici, L. C. Botten, C. M. de Sterke, P. A. Robinson, and R. C. McPhedran, Phys. Rev. B **57**, 13535 (1998).
[27]J. E. Sipe, P. Sheng, B. S. White, and M. H. Cohen, Phys. Rev. Lett. **60**, 108 (1988); Y. Yamada, S. Takeuchi, S. Nitta, and S. Nonomura, J. Non-Cryst. Solids **198–200**, 796 (1996); X. Du, D. Zhang, X. Zhang, B. Feng, and D. Zhang, Phys. Rev. B **56**, 28 (1997).
[28]K. Y. Bliokh and V. D. Freilikher, Phys. Rev. B **70**, 245121 (2004).
[29]K. Y. Bliokh, Phys. Lett. A **344**, 127 (2005); R. A. Sepkhanov, A. Ossipov, and C. W. J. Beenakker, Europhys. Lett. **85**, 14005 (2009).
[30]E. McCann, K. Kechedzhi, V. I. Fal'ko, H. Suzuura, T. Ando, and B. L. Altshuler, Phys. Rev. Lett. **97**, 146805 (2006); F. V. Tikhonenko, A. A. Kozikov, A. K. Savchenko, and R. V. Gorbachev, Phys. Rev. Lett. **103**, 226801 (2009); S.-L. Zhu, D.-W. Zhang, and Z. D. Wang, Phys. Rev. Lett. **102**, 210403 (2009).
[31]I. V. Shadrivov, K. Y. Bliokh, Y. P. Bliokh, V. D. Freilikher, and Y. S. Kivshar, Phys. Rev. Lett. **104**, 123902 (2010).
[32]S. A. Gredeskul and Y. S. Kivshar, Phys. Rep. **216**, 1 (1991); J. D. Maynard, Rev. Mod. Phys. **73**, 401 (2001).
[33]P. Devillard and B. Souillard, J. Stat. Phys. **43**, 423 (1986); B. Doucot and R. Rammal, Europhys. Lett. **3**, 969 (1987); Y. S. Kivshar, S. A. Gredeskul, A. Sánchez, and L. Vázquez, Phys. Rev. Lett. **64**, 1693 (1990); M. I. Molina and G. P. Tsironis, Phys. Rev. Lett. **73**, 464 (1994); V. A. Hopkins, J. Keat, G. D. Meegan, T. Zhang, and J. D. Maynard, Phys. Rev. Lett. **76**, 1102 (1996); G. Kopidakis and S. Aubry, Phys. Rev. Lett. **84**, 3236 (2000); A. S. Pikovsky and D. L. Shepelyansky, Phys. Rev. Lett. **100**, 094101 (2008).
[34]K. Y. Bliokh, S. A. Gredeskul, P. Rajan, I. V. Shadrivov, and Y. S. Kivshar, Phys. Rev. B **85**, 014205 (2012).
[35]M. Inoue and T. Fujii, J. Appl. Phys. **81**, 5659 (1997).
[36]F. A. Erbacher, R. Lenke, and G. Maret, Europhys. Lett. **21**, 551 (1993); A. S. Martinez and R. Maynard, Phys. Rev. B **50**, 3714 (1994); D. Lacoste and B. A. van Tiggelen, Phys. Rev. E **61**, 4556 (2000); R. Lenke, R. Lehner, and G. Maret, Europhys. Lett. **52**, 620 (2000).
[37]N. F. Mott and W. D. Twose, Adv. Phys. **10**, 107 (1961).
[38]H. Furstenberg, Trans. Am. Math. Soc. **108**, 377 (1963).
[39]V. D. Freilikher and S. A. Gredeskul, Prog. Opt. **30**, 137 (1992).
[40]F. M. Izrailev, A. A. Krokhin, and N. M. Makarov, Phys. Rep. **512**, 125, (2012).
[41]L. A. Pastur and A. L. Figotin, *Spectra of Random and Almost Periodic Operators* (Springer, Berlin, 1992).
[42]S. A. Gredeskul, A. V. Marchenko, and L. A. Pastur, *Surveys in Applied Mathematics, v. 2* (Plenum, New York, 1995), p. 63.
[43]A. A. Asatryan, L. C. Botten, M. A. Byrne, V. D. Freilikher, S. A. Gredeskul, I. V. Shadrivov, R. C. McPhedran, and Yu. S. Kivshar, Phys. Rev. Lett. **99**, 193902 (2007).
[44]A. A. Asatryan, S. A. Gredeskul, L. C. Botten, M. A. Byrne, V. D. Freilikher, I. V. Shadrivov, R. C. McPhedran, and Yu. S. Kivshar, Phys. Rev. B **81**, 075124 (2010).
[45]A. A. Asatryan, L. C. Botten, M. A. Byrne, V. D. Freilikher, S. A. Gredeskul, I. V. Shadrivov, R. C. McPhedran, and Yu. S. Kivshar, Phys. Rev. B **82**, 205124 (2010).
[46]A. A. Asatryan, L. C. Botten, M. A. Byrne, V. D. Freilikher, S. A. Gredeskul, I. V. Shadrivov, R. C. McPhedran, and Yu. S. Kivshar, Phys. Rev. B **85**, 045122 (2012).
[47]Y. P. Bliokh, V. Freilikher, S. Savel'ev, and F. Nori, Phys. Rev. B **79**, 075123 (1009).
[48]V. V. Cheianov, V. Fal'ko, and B. L. Altshuler, Science **315**, 1252 (2007).
[49]V. Baluni and J. Willemsen, Phys. Rev. A **31**, 3358 (1985).
[50]S. M. Rytov, Yu. A. Kravtsov, and V. I. Tatarskii, *Principles of Statistical Radiophysics* (Springer, Berlin, 1987).
[51]E. J. Torres-Herrera, F. M. Israilev, and N. M. Makarov, Fiz. Nizk. Temp. **37**, 1201 (2011) [Low Temp. Phys. **37**, 957 (2011)].
[52]E. J. Torres-Herrera, F. M. Israilev, and N. M. Makarov, Europhys. Lett. **98**, 27003 (2012).
[53]F. M. Izrailev, N. M. Makarov, and E. J. Torres-Herrera, Physica B **405**, 3022 (2010).
[54]F. M. Izrailev and N. M. Makarov, Phys. Rev. Lett. **102**, 203901 (2009).
[55]V. D. Freilikher, B. A. Liansky, I. V. Yurkevich, A. A. Maradudin, and A. R. McGurn, Phys. Rev. E **51**, 6301 (1995).
[56]M. V. Berry and S. Klein, Eur. J. Phys. **18**, 222 (1997).
[57]F. M. Izrailev, T. Kottos, and G. Tsironis, Phys. Rev. B **52**, 3274 (1995).
[58]S. A. Gredeskul and L. A. Pastur, Fiz. Nizk. Temp. **1**, 277 (1975) [Sov. J. Low Temp. Phys. **1**, 135 (1975)].
[59]T. N. Antzygina, L. A. Pastur, and V. A. Sliusarev, Fiz. Nizk. Temp. **7**, 5 (1981) [Sov. J. Low Temp. Phys. **7**, 5 (1981)].
[60]K. Y. Bliokh and Y. P. Bliokh, Physics—Uspekhi **47**, 393 (2004) [Usp. Fiz. Nauk **174**, 439 (2004)].
[61]C. Caloz and T. Ito, Proc. IEEE **93**, 1744 (2005).
[62]D. Schurig, J. Mock, B. Justice, S. Cummer, J. Pendry, A. Starr, and D. Smith, Science **314**, 977 (2006).
[63]J. Kästel and M. Fleischhauer, Phys. Rev. A **71**, 011804(R) (2005).
[64]Y. Yang, J. Xu, H. Chen, and S. Zhu, Phys. Rev. Lett. **100**, 043601 (2008).
[65]M. V. Gorkunov, S. A. Gredeskul, I. V. Shadrivov, and Yu. S. Kivshar, Phys. Rev. E **73**, 056605 (2006).
[66]C. Martijn de Sterke and R. C. McPhedran, Phys. Rev. B **47**, 7780 (1993).
[67]M. Ya. Azbel, Phys. Rev. B **28**, 4106 (1983).
[68]Y. Dong and X. Zhang, Phys. Lett. A **359**, 542 (2006).
[69]E. M. Nascimento, F. A. B. F. de Moura, and M. L. Lyra, Opt. Express **16**, 6860 (2008).
[70]P. Han, C. T. Chan, and Z. Q. Zhang, Phys. Rev. B **77**, 115332 (2008).
[71]D. Mogilevtsev, F. A. Pinheiro, R. R. dos Santos, S. B. Cavalcanti, and L. E. Oliveira, Phys. Rev. B **82**, 081105 (2010).
[72]E. Reyes-Go'mez, A. Bruno-Alfonso, S. B. Cavalcanti, and L. E. Oliveira, Phys. Rev. E **84**, 036604 (2011).
[73]D. Mogilevtsev, F. A. Pinheiro, R. R. dos Santos, S. B. Cavalcanti, and L. E. Oliveira, Phys. Rev. B **84**, 094204 (2011).
[74]G. A. Luna-Acosta, F. M. Izrailev, N. M. Makarov, U. Kuhl, and H.-J. Stöckmann, Phys. Rev. B **80**, 115112 (2009).
[75]B. L. Altshuler, A. G. Aronov, and B. Z. Spivak, JETP Lett. **32**, 94 (1981).
[76]I. M. Lifshitz and V. Ya. Kirpichenkov, Sov. Phys. JETP **50**, 499 (1979) [Zh. Eksp. Teor. Fiz. **77**, 989 (1979)].
[77]M. Ya. Azbel and P. Soven, Phys. Rev. B **27**, 831 (1983).
[78]K. Y. Bliokh, Y. P. Bliokh, V. Freilikher, S. Savel'ev, and F. Nori, Rev. Mod. Phys. **80**, 1201 (2008).
[79]R. A. Shelby, D. R. Smith, and S. Schultz, Science **292**, 77 (2001).
[80]D. R. Smith, Phys. Rev. E **81**, 036605 (2010).
[81]X. Huang, Y. Lai, Z. H. Hang, H. Zeng, and C. T. Chan, Nature Mater. **10**, 582 (2011).
[82]R. J. Potton, Rep. Prog. Phys. **67**, 717 (2004).
[83]I. L. Lubchenskii, N. N. Dadoenkova, M. I. Lyubchanskii, E. A. Shapovalov, and T. Rasing, J. Phys. D: Appl. Phys. **36**, R277 (2003).
[84]M. Inoue, R. Fujikawa, A. Baryshev, A. Khanikaev, P. B. Lim, H. Uchida, O. Aktsipetrov, A. Fedyanin, T. Murzina, and A. Granovsky, J. Phys. D: Appl. Phys. **39**, R151 (2006).
[85]M. Inoue, K. Arai, and T. Fujii, J. Appl. Phys. **83**, 6768 (1998); M. Inoue, K. Arai, T. Fujii, and M. Abe, J. Appl. Phys. **85**, 5768 (1999); M. J. Steel, M. Levy, and R. M. Osgood, J. Lightwave Technol. **18**, 1297 (2000).
[86]A. Figotin and I. Vitebsky, Phys. Rev. E **63**, 066609 (2001).
[87]A. B. Khanikaev, A. V. Baryshev, M. Inoue, and Y. S. Kivshar, Appl. Phys. Lett. **95**, 011101 (2009); A. B. Khanikaev, S. H. Mousavi, G. Shvets, and Y. S. Kivshar, Phys. Rev. Lett. **105**, 126804 (2010).
[88]A. B. Khanikaev and M. J. Steel, Opt. Express **17**, 5265 (2009).
[89]Z. Yu, Z. Wang, and S. Fan, Appl. Phys. Lett. **90**, 121133 (2007); F. D. M. Haldane and S. Raghu, Phys. Rev. Lett. **100**, 013904 (2008); Z. Wang, Y. D. Chong, J. D. Joannopoulos, and M. Soljacic, Phys. Rev. Lett. **100**, 013905 (2008); Z. Wang, Y. Chong, J. D. Joannopoulos, and M. Soljacic, Nature **461**, 772 (2009).
[90]U. Frisch, C. Froeschle, J.-P. Scheidecker, and P.-L. Sulem, Phys. Rev. A **8**, 1416 (1973).

[91]K. Y. Bliokh, Y. P. Bliokh, and V. D. Freilikher, J. Opt. Soc. Am. B **21**, 113 (2004).
[92]I. Bialynicki-Birula, Prog. Opt. **XXXVI**, 1 (1996).
[93]J. Zalesny, Int. J. Theor. Phys. **48**, 1801 (2009).
[94]M. Mehrafarin and H. Balajany, Phys Lett A **374**, 1608 (2011).
[95]L. Silberstein, Ann. Phys. **22**, 579 (1907).
[96]D. Dragoman and M. Dragoman, *Quantum-Classical Analogies* (Springer, Berlin, 2004).
[97]P. Darancet, V. Olevano, and D. Mayou, e-print arXiv:condmat/080.3553.
[98]S. Tamura and F. Nori, Phys. Rev. B **41**, 7941 (1990).
[99]N. Nishiguchi, S. Tamura, and F. Nori, Phys. Rev. B **48**, 2515 (1993).
[100]N. Nishiguchi, S. Tamura, and F. Nori, Phys. Rev. B **48**, 14426 (1993).
[101]M. Born and E. Wolf, *Principles of Optics* (Cambridge University Press, Cambridge, UK, 1999).
[102]M. I. Katsnelson, K. S. Novoselov, and A. K. Geim, Nature Phys. **2**, 620 (2006).
[103]O. Klein, Z. Phys. **53**, 157 (1929); C. W. J. Beenakker, Rev. Mod. Phys. **80**, 1337 (2008).
[104]M. Titov, Europhys. Lett. **79**, 17004 (2007).
[105]D. Clément, A. F. Varón, M. Hugbart, J. A. Retter, P. Bouyer, L. Sanchez-Palencia, D. M. Gangardt, G. V. Shlyapnikov, and A. Aspect, Phys. Rev. Lett. **95**, 170409 (2005); T. Schulte, S. Drenkelforth, J. Kruse, W. Ertmer, J. Arlt, K. Sacha, J. Zakrzewski, and M. Lewenstein, Phys. Rev. Lett. **95**, 170411 (2005).
[106]J. Topolancik, F. Vollmer, and B. Ilic, Appl. Phys. Lett. **91**, 201102 (2007).
[107]E. Abraham and S. D. Smith, Rep. Prog. Phys. **45**, 815 (1982); H. M. Gibbs, S. L. McCall, and T. N. C. Venkatesan, Phys. Rev. Lett. **36**, 1135 (1976); F. S. Felber and J. H. Marburger, Appl. Phys. Lett. **28**, 731 (1976); M. Soljačić, M. Ibanescu, S. G. Johnson, Y. Fink, and J. D. Joannopoulos, Phys. Rev E. **66**, 055601(R) (2002); M. Notomi, A. Shinya, S. Mitsugi, G. Kira, E. Kuramochi, and T. Tanabe, Opt. Express **13**, 2678 (2005).
[108]A minor discrepancy between the theoretical model and exact numerical simulations can be seen for high incident power for the first resonance. This is because at high intensity the shape of the resonance line changes, which is not taken into account by the model.
[109]K.-P. Hwang, IEEE Microw. Wirel. Compon. Lett. **15**, 271 (2005).
[110]M. D. Tocci, M. J. Bloemer, M. Scalora, J. P. Dowling, and C. M. Bowden, Appl. Phys. Lett. **66**, 2324 (1995); J. J. Liang, S. T. Lau, M. H. Leary, and J. M. Ballantyne, Appl. Phys. Lett. **70**, 1192 (1997); K. Gallo and G. Assanto, J. Opt. Soc. Am. B **16**, 267 (1999).

This article was published in English in the original Russian journal. Reproduced here with stylistic changes by AIP.